

Interannual Variability of Sea Level and Mesoscale Energy in the Indian and Pacific Oceans

Author: Andrew Delman (329B)

Co-Authors: Tong Lee (329B), Bo Qiu (U. Hawai'i)

Introduction

- Mesoscale eddies are systems in the ocean characterized by anomalies in pressure, circulation, and water properties.
 - They have many similarities with mid-latitude systems in the atmosphere (the “highs” and “lows” that we see on weather maps).

Direction of rotation is shown for N. Hemisphere; reverses in S. Hemisphere



Anticyclones
 (“warm-core” eddies)



Cyclones
 (“cold-core” eddies)

- Like mid-latitude storms in the atmosphere, they are important for the exchange of heat between the tropics, mid-latitudes, and polar regions in the ocean
 - They also exchange heat directly with the atmosphere, and upwell fresh nutrients to the ocean surface, influencing chlorophyll blooms
- However, their spatial and temporal scales are very different from their atmospheric cousins

	Mid-latitude storms	Mesoscale eddies
Medium	Atmosphere	Ocean
Spatial scales	~200-2000 km	~10-200 km
Temporal scales	~3 days-3 weeks	~3 weeks-3 years!

- Understanding** and **predicting** the interannual variability and long-term trend of eddy activity improves projections of regional changes in climate and biological productivity

Research questions

- How do modes of climate variability (such as El Niño/La Niña) interact with mesoscale eddy activity on multi-year timescales?
- How are changes in mesoscale eddy activity related to changes in sea level?

Methodology

- Use measurements of sea level anomaly (SLA) and sea surface height (SSH) in the SSALTO/DUACS gridded product, obtained from numerous altimetry missions (TOPEX/Poseidon, Jason-series, ERS-series, Envisat, Saral/AltiKa, Cryosat-2, Sentinel-3A, HY-2A)

Scale decomposition

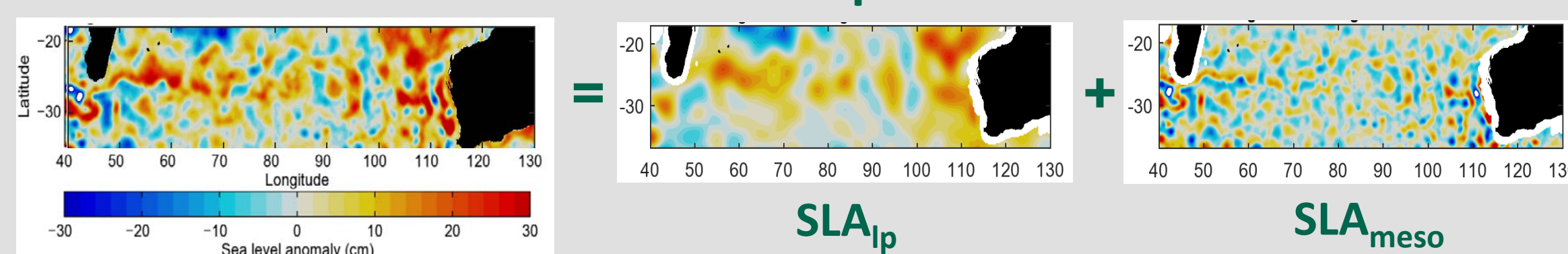


Figure 1. (left) Snapshot of SSALTO/DUACS sea level anomaly, 2011 Jul 02, and its decomposition into (center) low-passed sea level anomaly SLA_{ip} and (right) the residual SLA field SLA_{meso} used to compute mesoscale EKE.

- Compute **eddy kinetic energy (EKE)** – measures eddy strength

$$EKE = 0.5[(u')^2 + (v')^2]$$

u' and v' are anomalous velocities computed from SLA

$$SLA_{ip} \rightarrow EKE_{ip}$$

$$SLA_{meso} \rightarrow EKE_{meso}$$

Atmospheric forcing of mesoscale eddies

- In the southeastern Indian Ocean, the variability of EKE at mesoscales (EKE_{meso}) is forced by winds over the tropical Pacific, driven by ENSO
 - El Niño **decreases** mesoscale eddy activity in most locations in the Indian Ocean

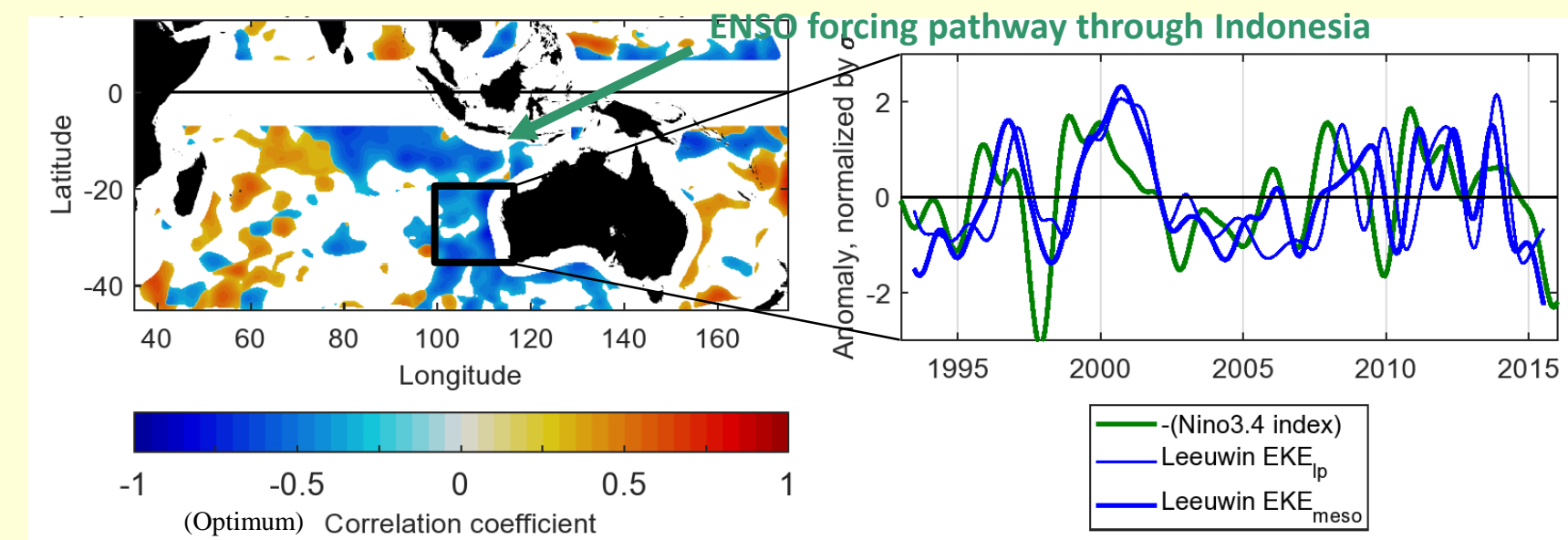


Figure 2. (Left) Optimum (i.e., maximum magnitude) correlation coefficients of EKE_{meso} with the Niño3.4 index for ENSO; a 14-month low-pass filter is applied to the time series to isolate interannual and decadal variability. EKE_{meso} lags Niño3.4 by ~6 months in the tropics, and ~3-18 months west of Australia. (Right) Time series of the Niño3.4 index with sign reversed, vs. EKE_{ip} and EKE_{meso} averaged in black box.

- In the eastern tropical Pacific, wind forcing related to ENSO is also a driver of mesoscale eddy variability
 - However, El Niño tends to **increase** mesoscale eddy activity in the tropical Pacific

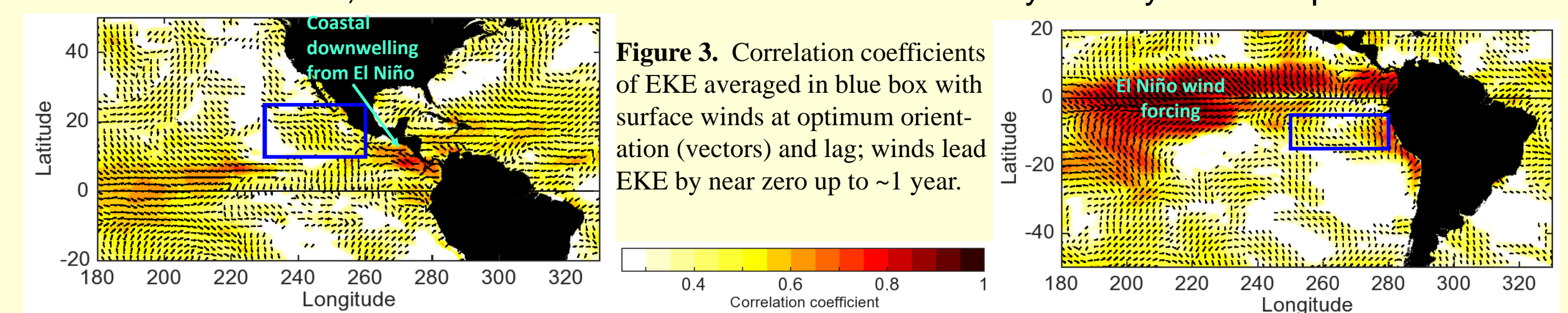


Figure 3.

Correlation coefficients of EKE averaged in blue box with surface winds at optimum orientation (vectors) and lag; winds lead EKE by near zero up to ~1 year.

Sea level and mesoscale eddy activity

- This research has found that the time variation of sea level is correlated with that of EKE in many parts of the global oceans

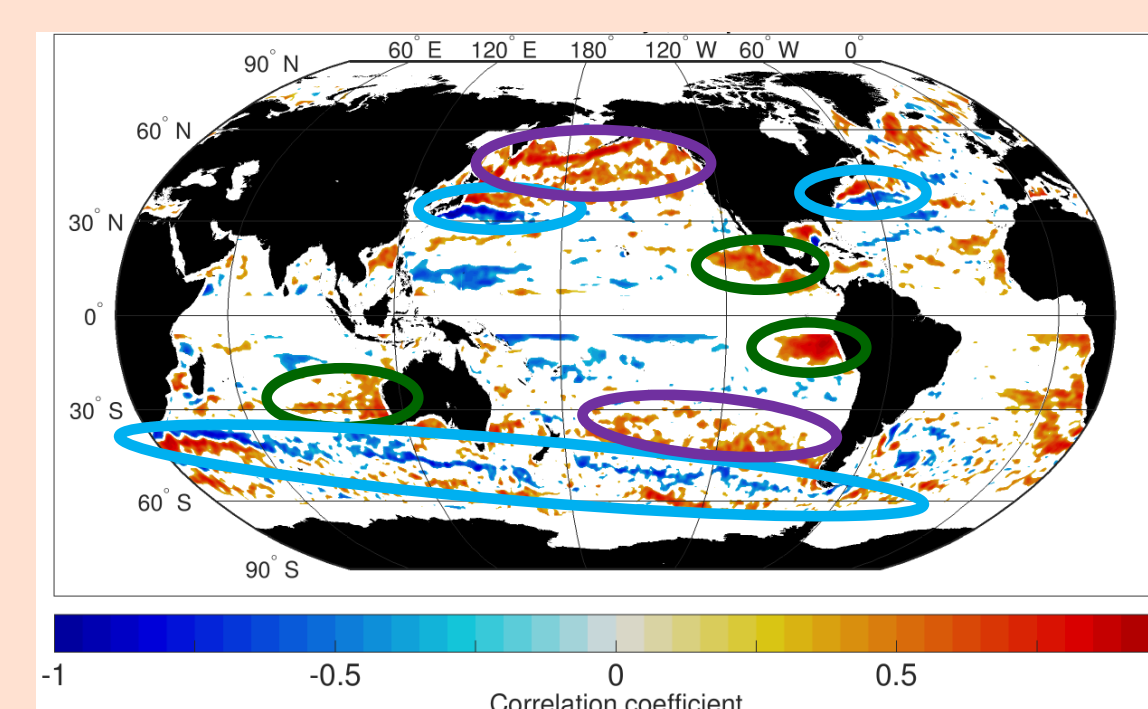


Figure 4. Pointwise correlation coefficient of sea level anomaly (SLA) with EKE, at zero lag, 14-month low-pass filtered for interannual and decadal timescales.

Correlation explained by wind forcing and/or ENSO
Correlation explained by proximity to strong energetic current
No known mechanism (yet) for correlation

- Mid-latitude Pacific regions with a positive SLA-EKE correlation also have an increasing EKE trend over the last 24 years

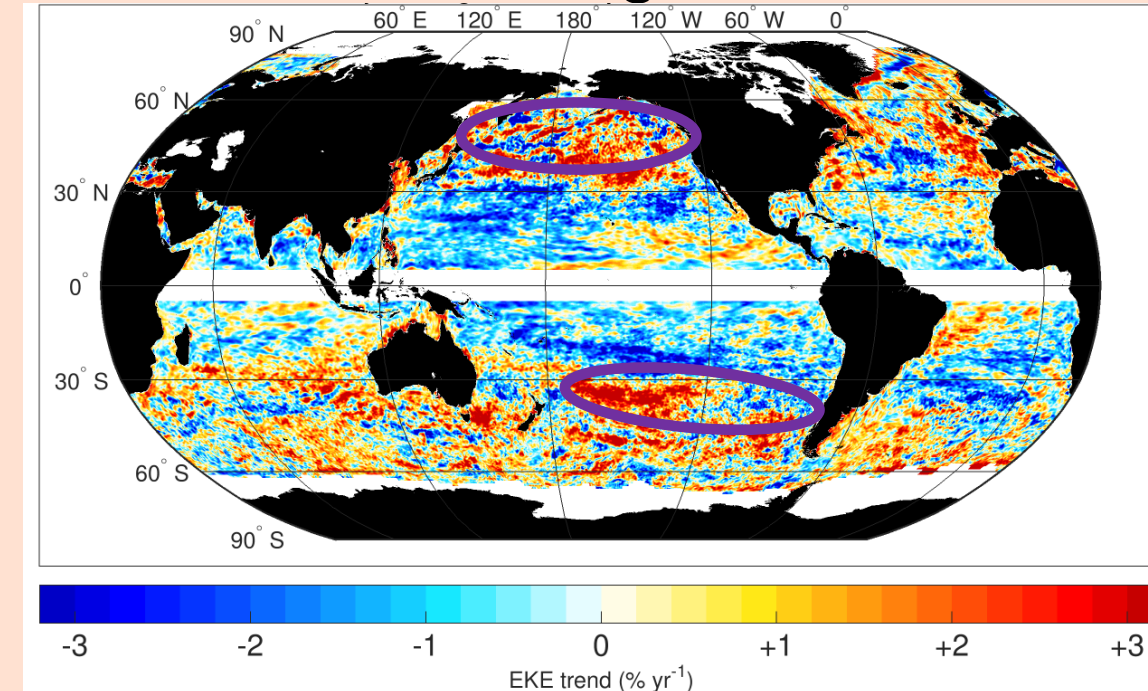


Figure 5. Linear trend of EKE over the 24 years (1993-2016) of the SSALTO/DUACS record, normalized by the mean EKE at each location.

In those areas where the SLA-EKE correlation resembles the EKE trend, high SLA events may give us a preview of eddy activity in a world with higher sea levels

Conclusions & Impact

- Mesoscale eddy variability on interannual/decadal timescales may result from:
 - Climate mode forcing (e.g., ENSO)
 - Wind forcing in coastal regions
 - Energetic current variability
 - Sea level variations?
- Implications of these findings include:
 - Better predictions of **variations in pathways of heat and nutrients** within the ocean, and exchanges with the atmospheric boundary layer
 - Suggestions of a link (in some regions) between **interannual eddy variability** and **longer-timescale (anthropogenic?) changes**

This research was supported by an appointment to the NASA Postdoctoral Program at the Jet Propulsion Laboratory, administered by Universities Space Research Association under contract with NASA.

Poster No. EB-01

Mesoscale circulation and fronts dynamics in the California Current System

Yackar Mauzole (329B), Hector Torres Gutierrez (329C) and Lee-Lueng Fu (3200)

1. Context

CCS The California Current System (CCS) is one of the four major coastal upwelling zones in the ocean, along with the Peru/Chile system, the Canary system and the Benguela system. It typically extends from 50°N to 20°N, and up to 135°W offshore. The CCS has been extensively studied over the last 50 years, and most of the dynamics of the region are well-known now. Still, questions remain regarding the link between the mesoscale ocean circulation and sea surface temperature (SST) fronts.

Science question The ocean dynamics of the CCS vary meridionally, from the northern CCS (from 50°N-40°N) to the central CCS (from 40°N-30°N), down to the southern CCS (from 30°N-20°N). SST fronts associated to the circulation of the CCS are not all generated during the upwelling season, and it is thought that **several frontogenetic mechanisms are at play in the region**.

Objective The aim of this study is to **investigate the spatial and temporal variability of SST fronts in the CCS, from north to south; and to determine the contribution of the various frontogenetic processes at the intra-annual and interannual scales**, by relying on a combination of satellite data and high-resolution numerical simulations.

2. Methodology

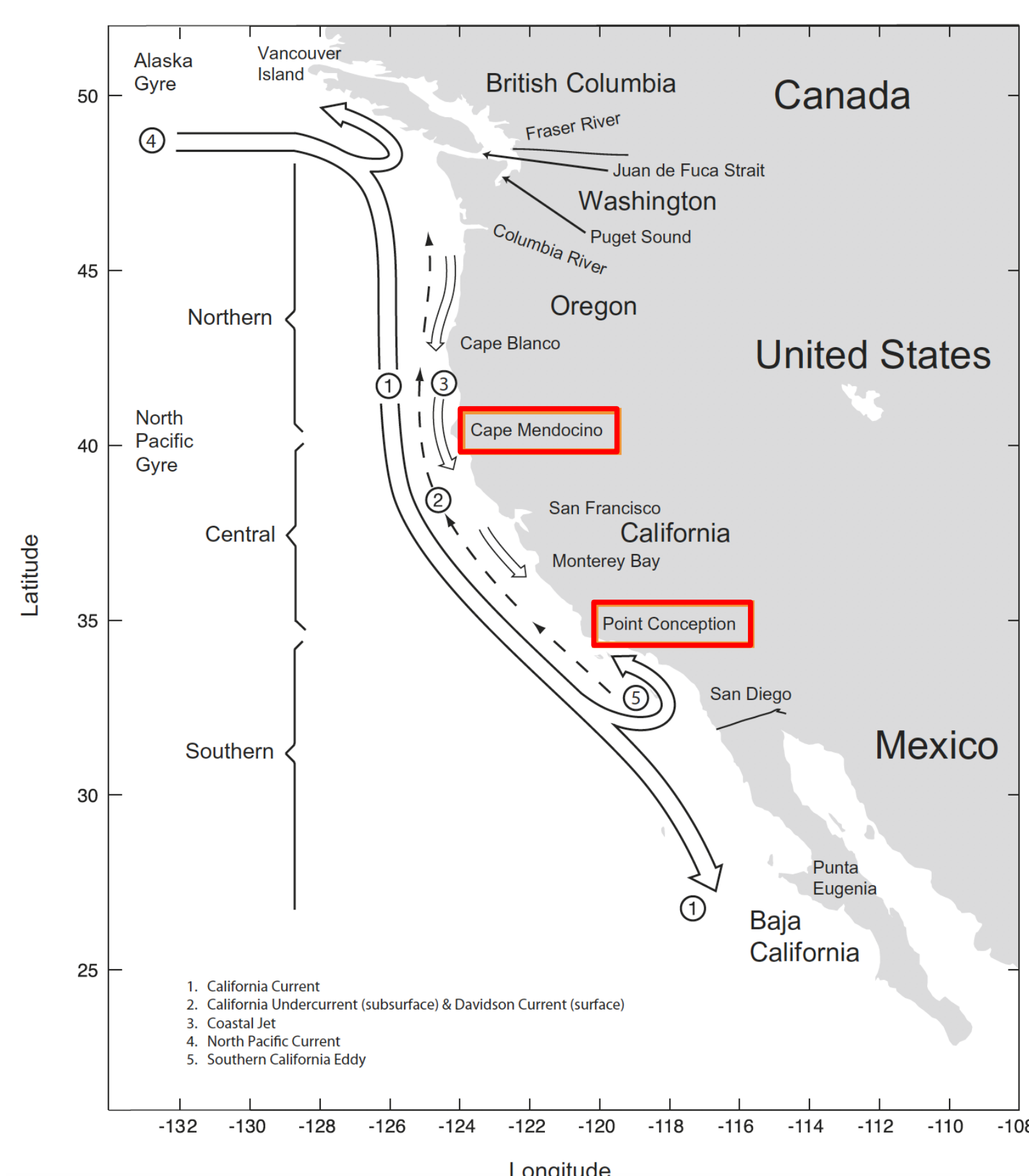
SST data SST fronts were detected by applying the Cayula-Cornillon algorithm to a time series of Level-3 SST fields. Pathfinder AVHRR (Advanced Very High Resolution Radiometer) data was used, which has a spatial resolution of 4km. The dataset extends from 1982 to 2011 included.

SSH data Derived altimetry products, such as sea level anomalies (SLA) and surface geostrophic velocities are used in the study. The dataset is distributed by CMEMS (Copernicus Marine Service Information - formerly AVISO), and is a multi-mission altimeter satellite Level-4 collection of observations, obtained from 1993 to present day, at a spatial resolution of ¼ degree.

Surface winds data

Monthly mean and daily fields were obtained from QuikSCAT data, at a wind vector resolution of 25km. The dataset is distributed by the CERSAT portal of Ifremer.

LLC2160 Based on a Latitude/Longitude/polar-Cap (LLC) configuration of the MIT general circulation model, the numerical simulations have a spatial resolution of 4km. The variables were saved hourly for 13 months, allowing us to investigate in more details the frontogenetic mechanisms at the intra-annual scale.

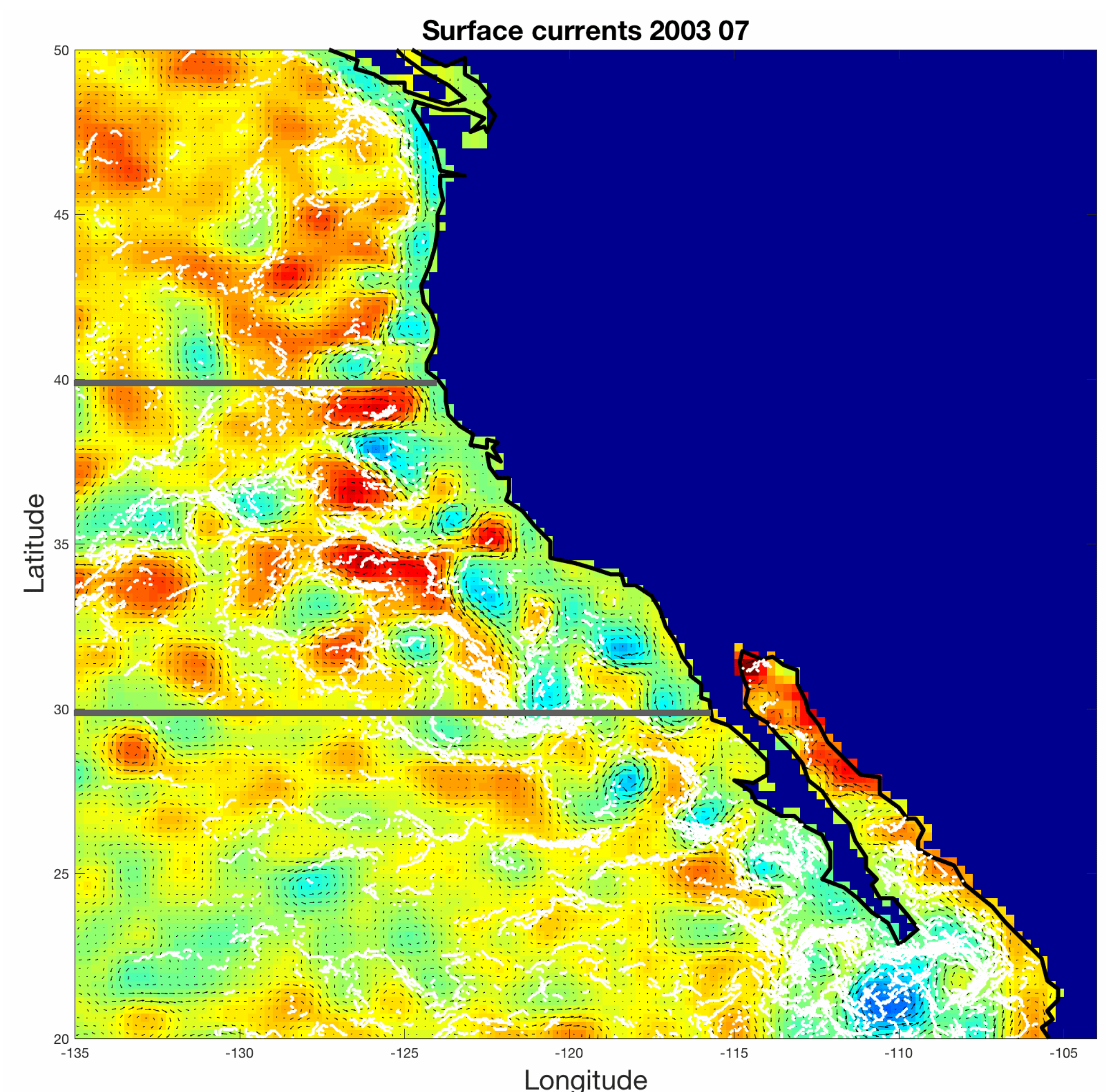


Domain of study. From Checkley and Barth, 2009.

3. Preliminary results

Collocation of features Monthly composite fields of SST fronts (white dots) are combined with monthly mean SLA fields (color). The mean surface geostrophic currents are also plotted (black arrows).

- In the northern CCS, SST fronts are found on the border of the coastal jet (negative SLA), and separate the coastal waters from open ocean.
- In the central CCS, SST fronts appear at the periphery of mesoscale eddies, where geostrophic velocities are stronger.
- In the southern CCS, SST fronts form organized structures, but they do not follow geostrophic contours.



4. Future work

Satellite data So far, I focused on combining SST and SSH data together and on looking at their variability. I will also include the wind data soon, to understand the relationship between the various fields and the observed variability better.

Numerical simulations After validation, I plan to investigate the 3D thermohaline structure of the southern CCS first, over the 13 months of output available. I will analyze the strain, vorticity and 3D velocity fields as well in the central CCS, by relying on the hourly output to illustrate the relationship between SST fronts and mesoscale eddies. In the northern CCS, the thermohaline and velocity structure around the coastal jet will be explored, relative to the observed SST fronts.

5. Benefit to JPL

- By relying on a combination of satellite observations and high-resolution simulations, I want to address the open question of frontal variability with regards to the mesoscale ocean circulation in the California Current System.
- The CCS, as well as the other coastal upwelling regions are critically important at the socio-economic level, by accounting for over 20% of the global fish catch. Bringing a better understanding of the ocean dynamics in these regions will be a great contribution to and from JPL.

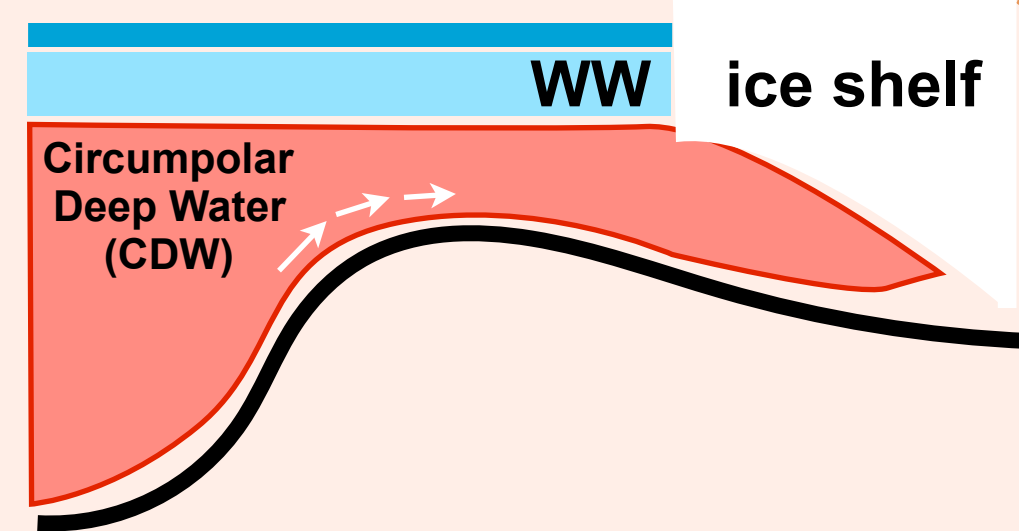
Origin of Circumpolar Deep Water intruding onto the Amundsen and Bellingshausen Sea continental shelves

Author: Yoshihiro Nakayama (329C), Dimitris Menemenlis (329C), Hong Zhang (329C), Michael Schodlok (329C), Eric Rignot (3340)

1. Introduction

Mechanisms controlling ice shelf melting

- 1) Strength of CDW intrusion
- 2) Thickness of Winter Water (WW)
- 3) Source CDW property



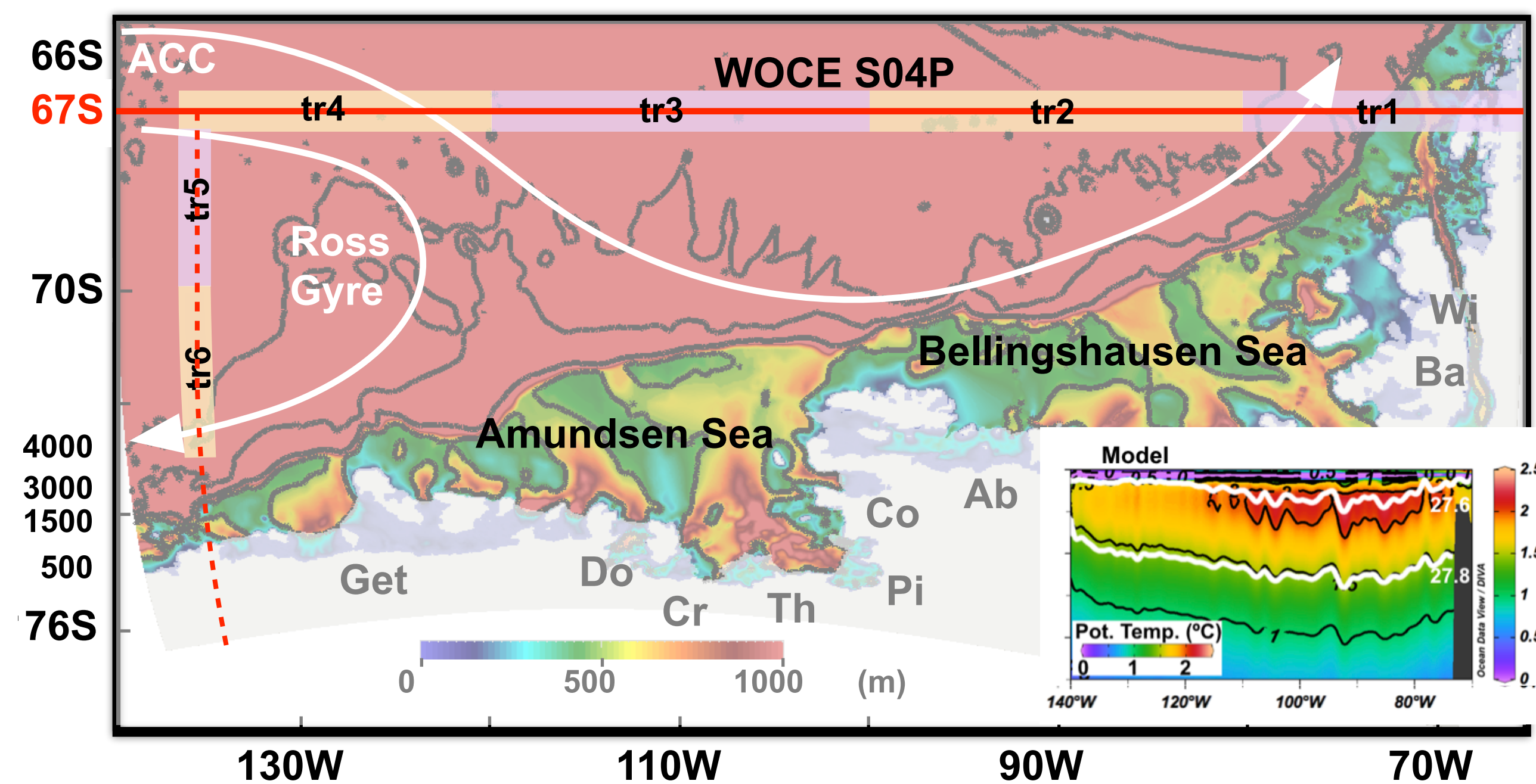
Known to be controlled by wind over shelf and shelf break areas (e.g., Dutriex et al., 2014, Webber et al., 2017).

We show for the first time that this is controlled by large-scale ocean circulation.

Objective & Significance

Melting of West Antarctic ice shelves and glaciers is caused by Circumpolar Deep Water (CDW) intruding onto the Amundsen and Bellingshausen Seas (ABS) continental shelves. We investigate CDW pathways onto the ABS using a regional ocean model that extends from Antarctic Continent to 65°S and from 140°W to 65°W. The numerical experiments comprise simulations forced by the four possible combinations of 2001-2006 and 2009-2014 lateral-oceanic and surface-atmospheric boundary conditions. **Simulated CDW tracers from a zonal section across 67°S (S04P) circulate along the Antarctic Circumpolar Current (ACC) and Ross Gyre (RG) and travel into ABS continental shelves after 3-5 years but source locations are shifted westward by ~900 km along S04P in 2001-2006 compared to 2009-2014.** We find that **off-shelf CDW that is ~0.2°C warmer in 2009-2014 than 2001-2006, leading to a ~0.1°C warming of bottom waters near eastern AS ice shelves.** These differences are primarily caused by model domain ocean circulation, which is determined by lateral, rather than surface, boundary conditions. This implies that large-scale atmospheric and ocean circulation outside of our regional model domain is able to control CDW pathways and thus off- and on-shelf CDW properties.

2. MITgcm regional ABS configuration



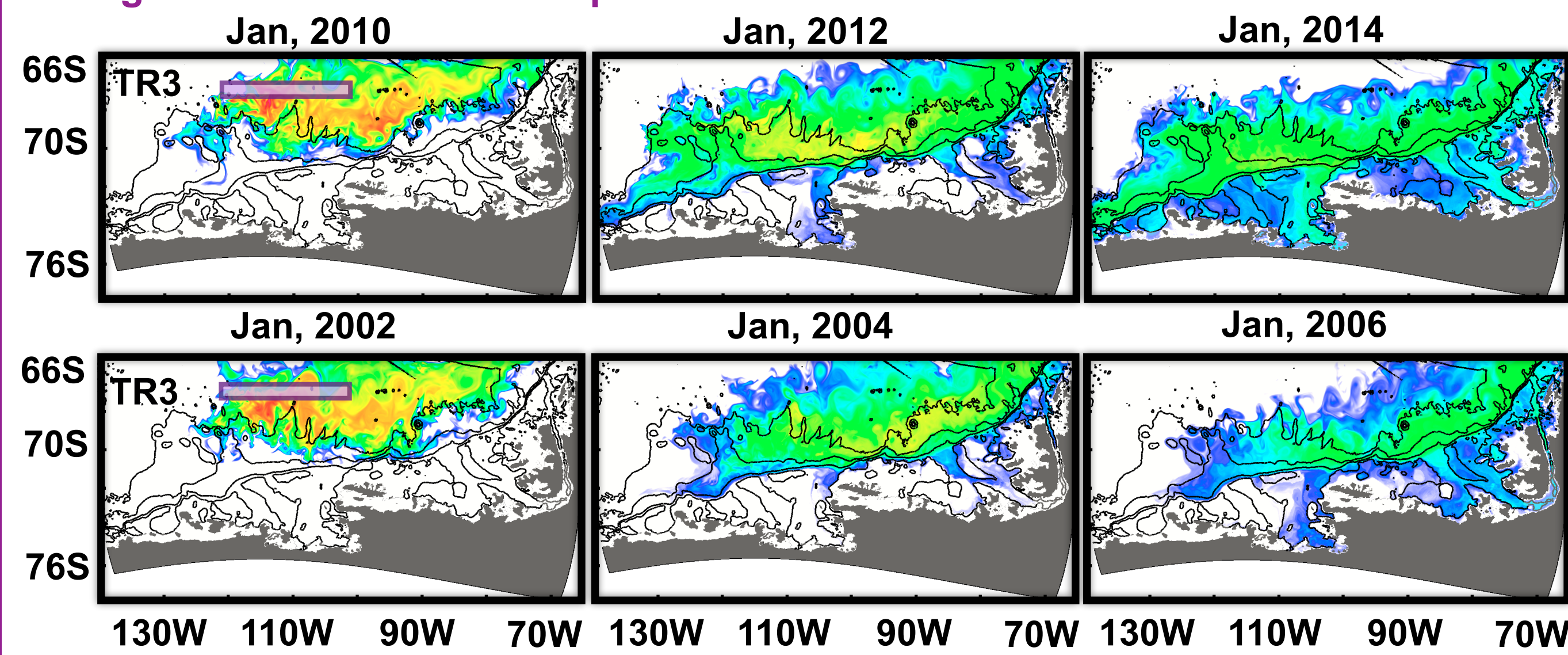
- Tracers representing CDW are initially released from purple and orange boxes with potential density of 27.60-27.80 near northern and eastern boundaries of the model domain.
- Initial condition from WOA 2013, boundary conditions from Estimating the Circulation and Climate of the Ocean (ECCO), bathymetry from IBSCO, and ice shelf draft from BEDMAP.
- 5-year simulations (2001-2006 and 2009-2014) with ECCO optimized atmospheric forcing.
- Horizontal grid spacing of 2-3 km and 50 vertical levels.

Sensitivity simulations

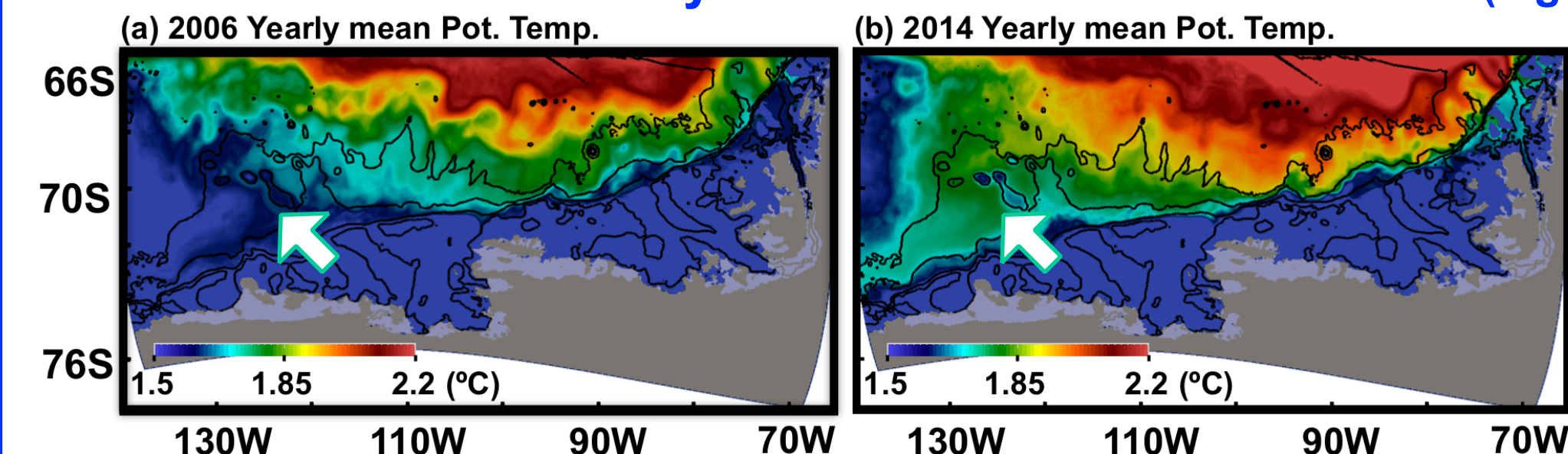
Simulations	Atmospheric Forcing (AF)	Oceanic Lateral boundary (BC)
CTRL(2009-2014)	2009-2014	2009-2014
2001-2006	2001-2006	2001-2006
BC09AF01	2001-2006	2009-2014
BC01AF09	2009-2014	2001-2006

3. Results

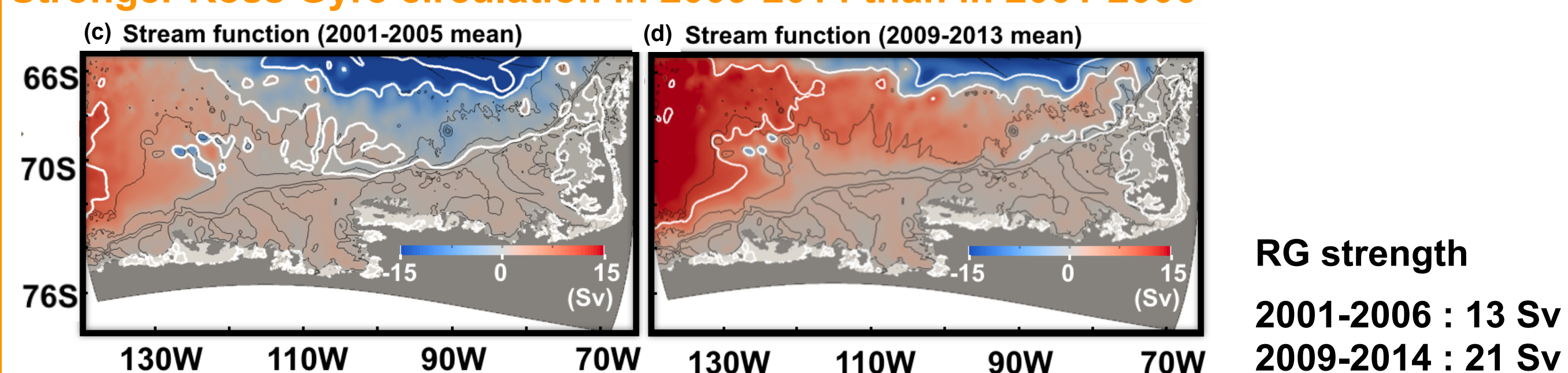
Stronger CDW westward transport in 2009-2014 than in 2001-2006



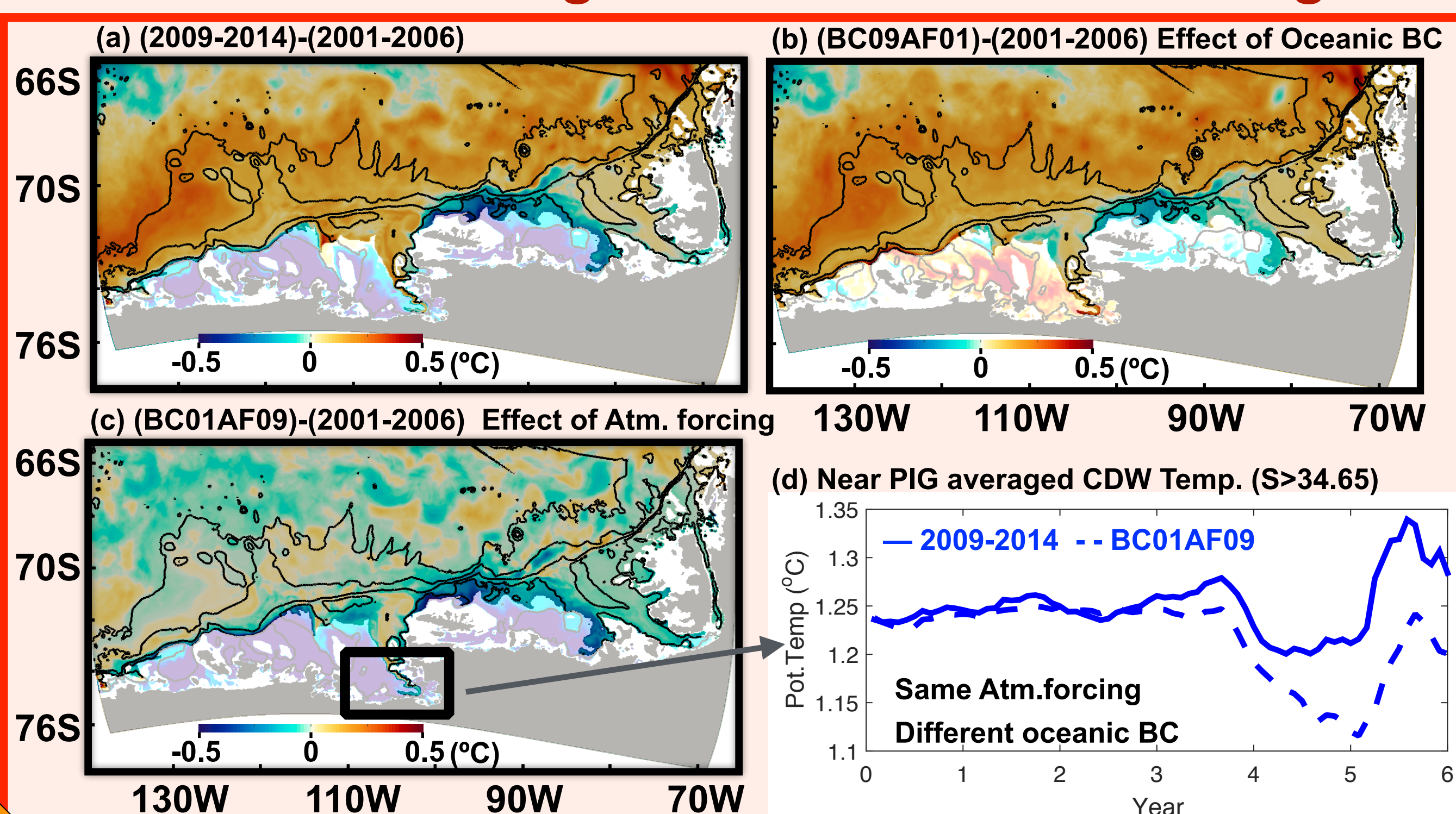
Off-shelf CDW is warmer by ~0.2°C in 2014 than in 2006 (e.g., see arrows)



Stronger Ross Gyre circulation in 2009-2014 than in 2001-2006



4. Off-shelf warming leads to on-shelf warming



Off-shelf warming is caused by lateral, rather than surface, boundary conditions. This means that large-scale ocean circulation controls CDW pathways and thus off- and on-shelf CDW properties.

5. Summary

Results of sensitivity experiments can be summarized as below.

Simulations	AS CDW origin	Off-shelf warming	RG strength
CTRL(2009-2014)	TR3	yes	strong
2001-2006	TR4	no	weak
BC09AF01	TR3	yes	strong
BC01AF09	TR4	no	weak

We show that large-scale ocean circulation is able to control CDW pathways and thus off-shelf CDW properties (~0.2°C), leading to on-shelf warming (~0.1°C).

Given the trend towards positive Southern Annular Mode causing southern shift of the westerlies, modified large-scale ocean circulation may exert a dominant control on the intruding CDW properties and possibly enhance the melting of West Antarctic glaciers.

Constructing a 25-year record of Antarctic ice-shelf height change from satellite altimetry

Fernando Paolo (329C) Johan Nilsson (329C) Alex Gardner (329C)

Summary

Motivation: Projections of sea-level change over the next century are highly uncertain, in part, due to insufficient understanding of ice-sheet sensitivity to changes in ocean properties. This limitation is related to the lack of long and continuous observational records of changes in ice shelves, where the ice sheet interacts with the ocean.

Challenge: Measurements from satellite radar altimeters of changes in ice-shelf height, informing how ice mass fluctuates, are strongly affected by variations in radar's surface scattering. E.g. Temporal changes in the dielectric properties of the near-surface firn alters the waveform shape of the radar echo, affecting the retrieved height and derived trends.

Approach: We are synthesizing 25+ years of satellite altimetry observations to extend the time span and improve the resolution (to 5-km monthly solutions) and accuracy of the Antarctic ice-shelf height-change record. We minimize the scattering-variation effect using a multi-variate fit to different waveform parameters. We improve some key geophysical corrections and optimize the integration of multi-mission data. We validate our results against ICESat and Operation IceBridge (laser altimetry) measurements.

Correlation of height changes with variations in radar scattering

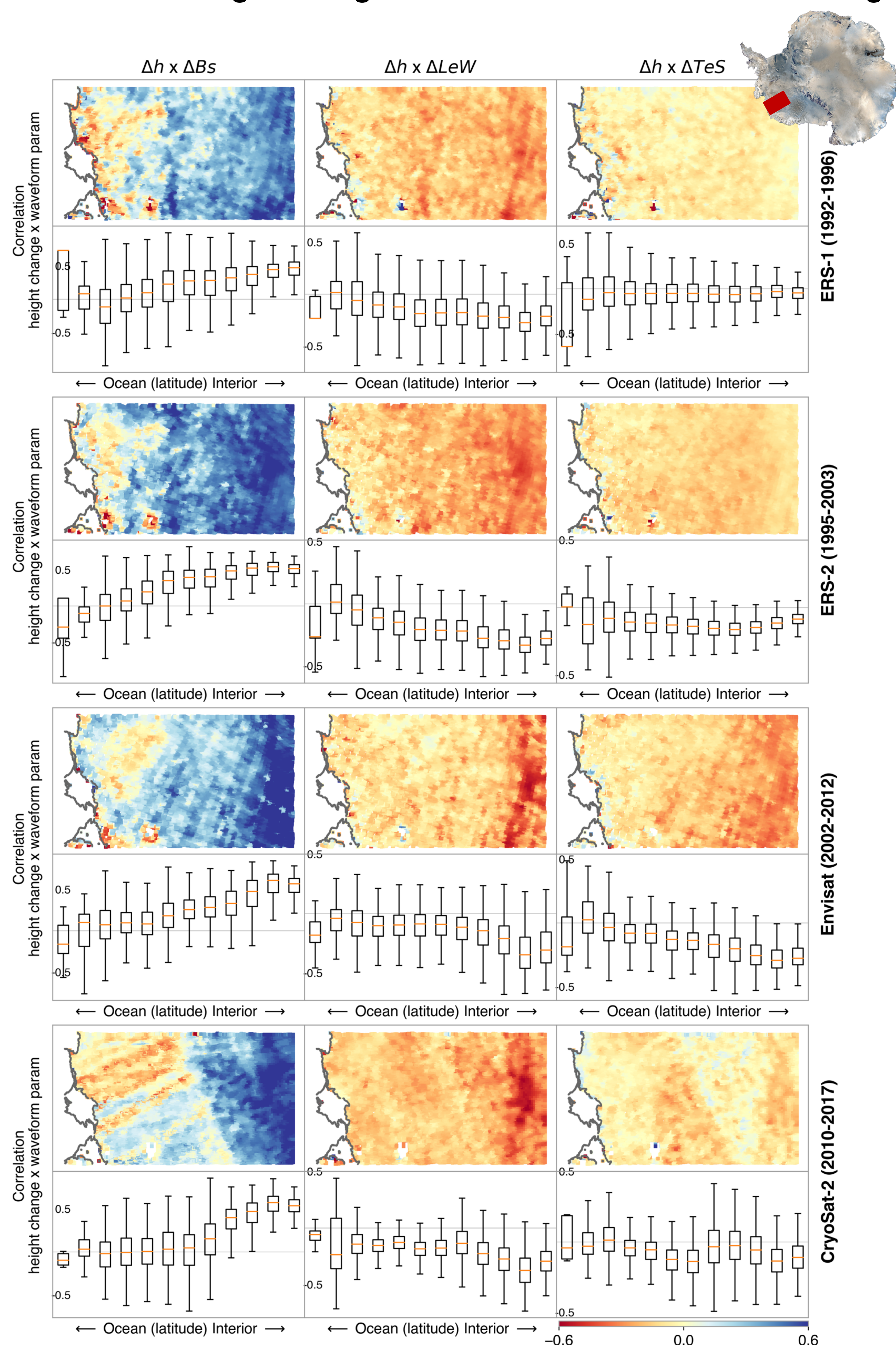
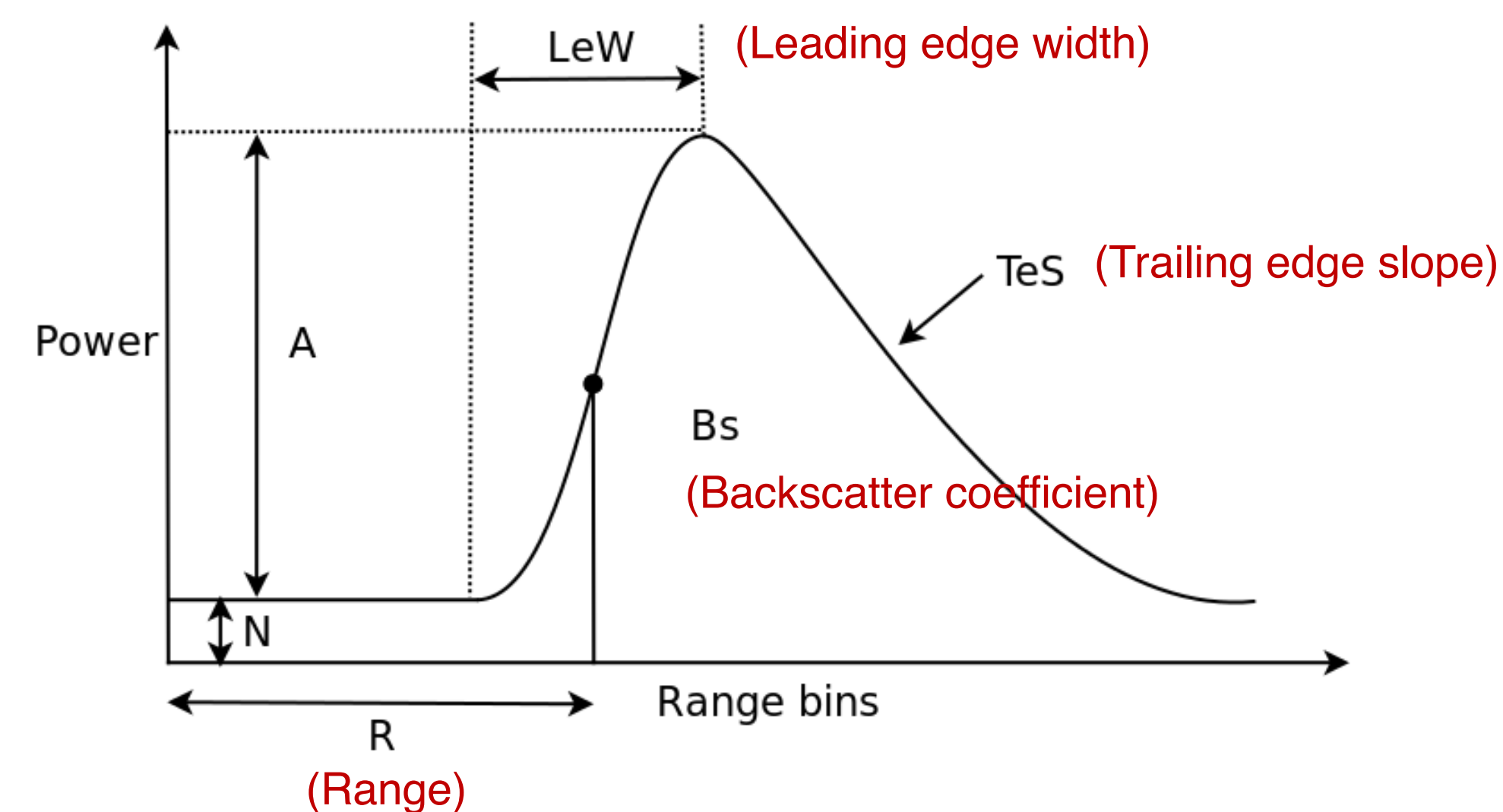


Fig.1: Correlation between retrieved height-changes and variation in waveform parameters: Backscatter coefficient (Bs), Leading edge width (LeW), and Trailing edge slope (TeS); for all radar missions.

National Aeronautics and Space Administration
Jet Propulsion Laboratory
California Institute of Technology
Pasadena, California

Model of the scattering-variation induced height-change



$$\Delta h(t) = b_1 \Delta Bs(t) + b_2 \Delta LeW(t) + b_3 \Delta TeS(t)$$

$$b_k = \frac{\Delta \text{diff}(\Delta h)}{\Delta \text{diff}(\Delta p_k)}, \quad p_k = \{Bs, LeW, TeS\}$$

Fig.2: Parameters determining the waveform shape of radar return echoes. These parameters (Bs, LeW, TeS) are sensitive to changes in the dielectric properties of the ice, affecting the retrieved satellite-to-surface range (R) from which the ice-sheet height is estimated. (Eq.) Our model of the scattering-variation induced height.

Minimizing the effect of variations in radar scattering

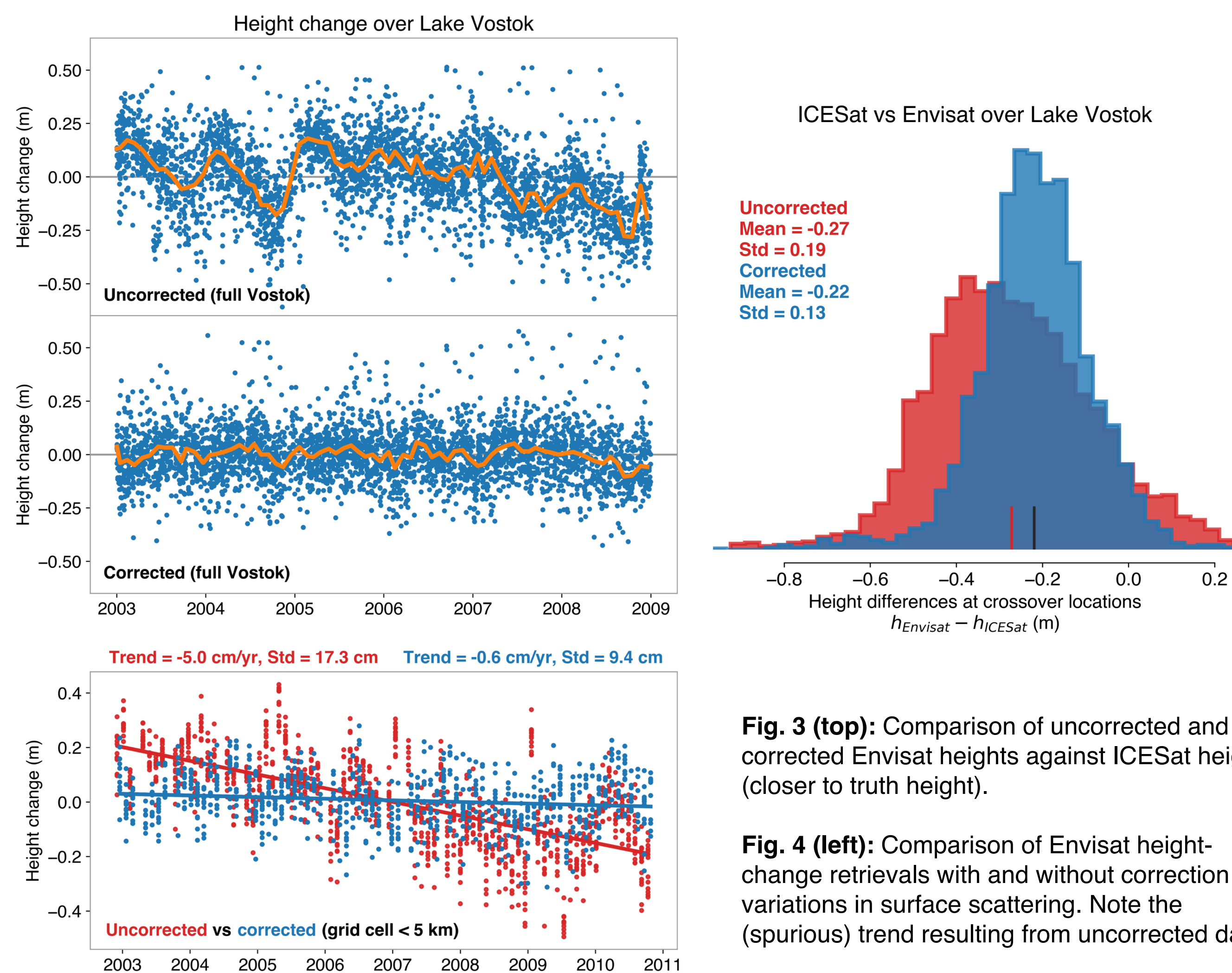


Fig. 3 (top): Comparison of uncorrected and corrected Envisat heights against ICESat heights (closer to truth height).

Fig. 4 (left): Comparison of Envisat height-change retrievals with and without correction for variations in surface scattering. Note the (spurious) trend resulting from uncorrected data.

In a nutshell

- All radar missions are strongly affected by variations in volume and surface scattering
- Scattering variations impact the waveform parameters (Backscatter coefficient, Leading edge width, and Trailing edge slope) of the return radar echo
- Changes in waveform parameters modify the waveform shape, affecting the retrieved height
- This effect is stronger towards the ice-sheet interior, having a large impact on ice-sheet volume change reconstructions
- We are able to minimize significantly the scattering effect on radar retrieved heights at 5 km spatial resolution
- We are able to bring closer together radar and laser measurements of height change

A New Vision of Air-Sea Interactions Driven by Submesoscale Ocean Motions and Winds

Author: Hector S Torres (329C)

Patrice Klein (329C) and Dimitris Menemenlis (329C)

Context

Context: Four years averages of 25-km measurements of near-surface wind speed and direction over the global ocean from the QuikSCAT satellite radar scatterometer reveal the existence of persistent mesoscale features (> 50 km) [Chelton et al., 2004].

Question: We do not have wind stress observations at scales smaller than 50 km. We know that ocean currents including submesoscale currents (< 50 km) do have an impact on the wind stress. Does this impact significantly affect the magnitude of the wind stress curl and divergence (since both involve spatial derivatives of the wind stress)?

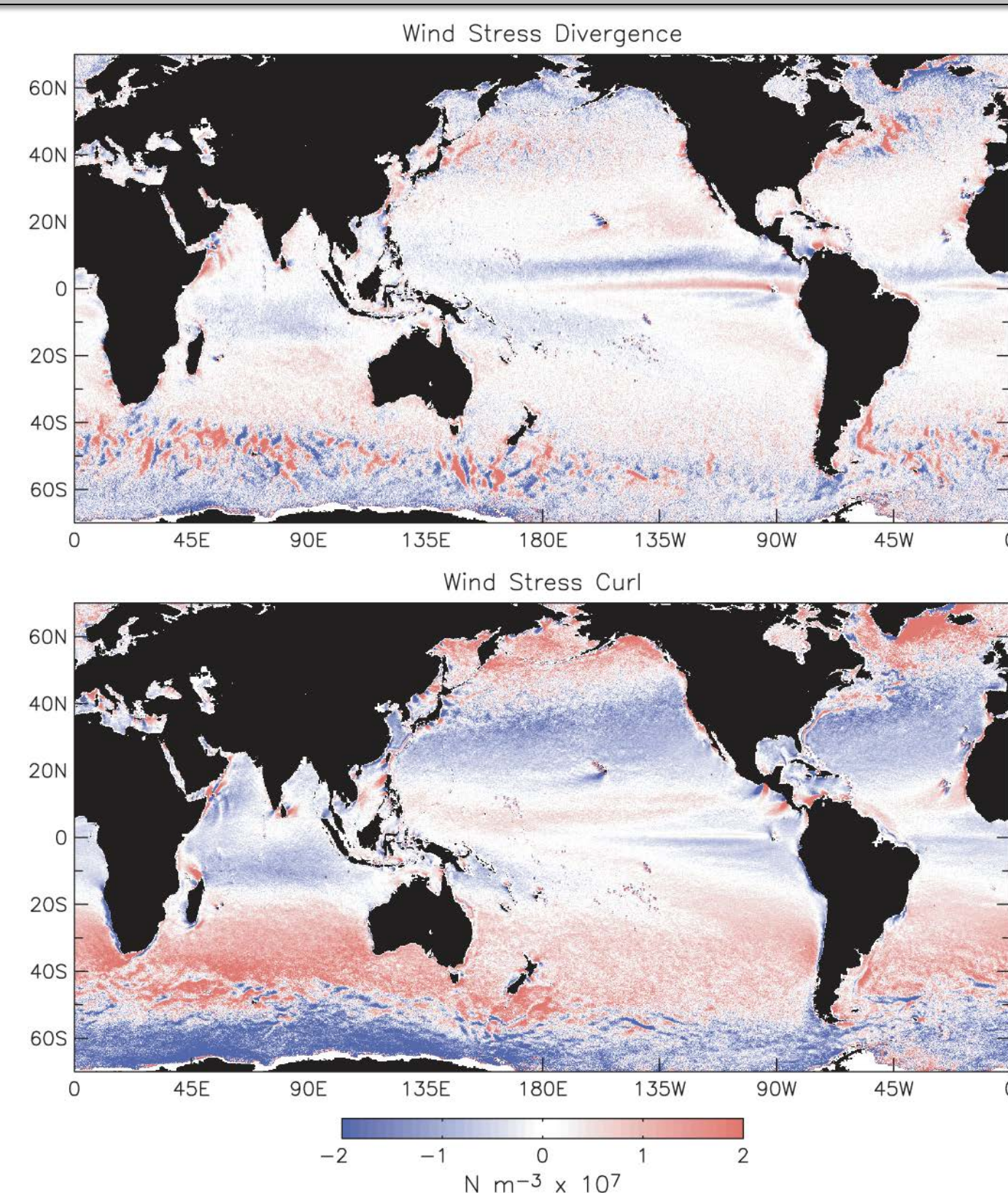


Figure 1. Wind stress divergence and wind stress curl estimated from QuikSCAT [Chelton et al., 2004]

Methodology

High-resolution (dx = 2km) ocean simulation: The MITgcm ocean model has been implemented in the Kuroshio Extension area to perform two experiments in order to assess the impact of the ocean submesoscale motions on wind stress.

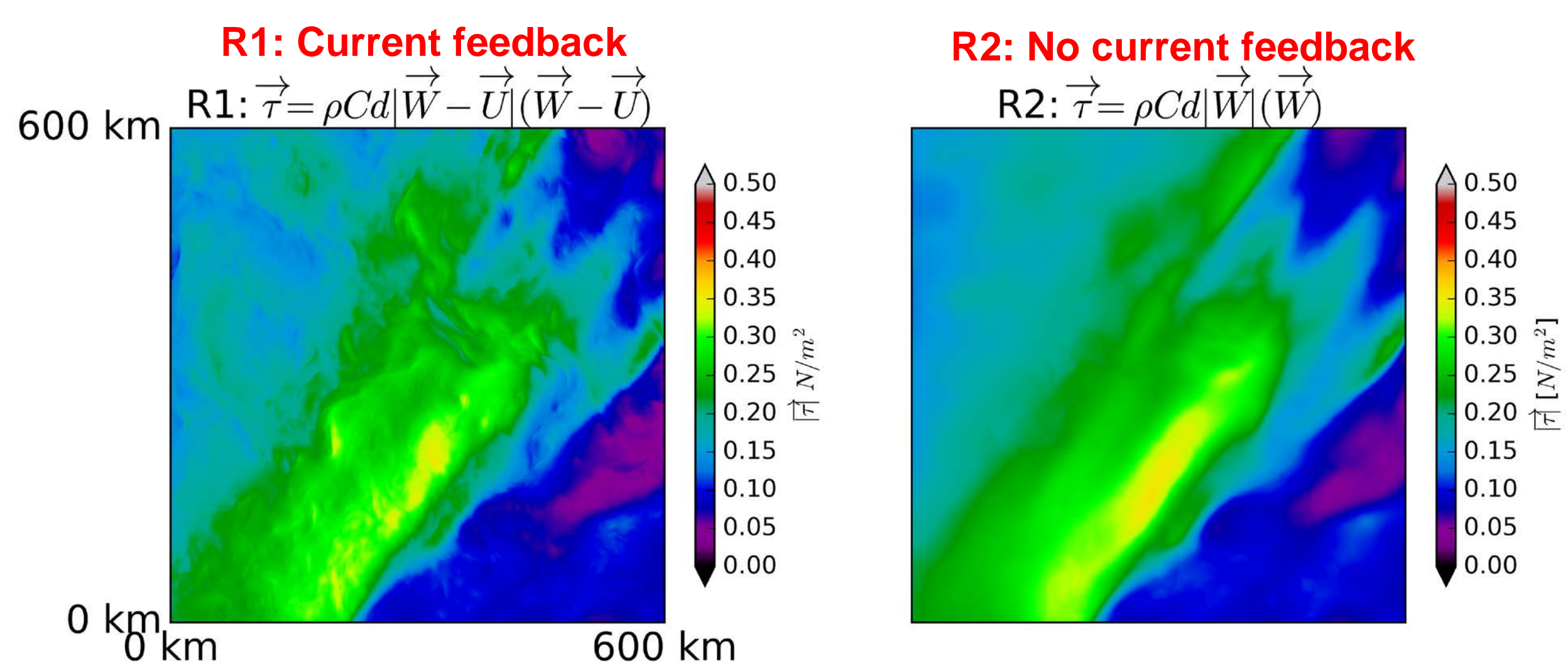


Figure 2. Magnitude of the wind stress: with surface current feedback (left panel) and without surface current feedback (right panel). The left panel highlights submesoscale features in the wind stress.

Results

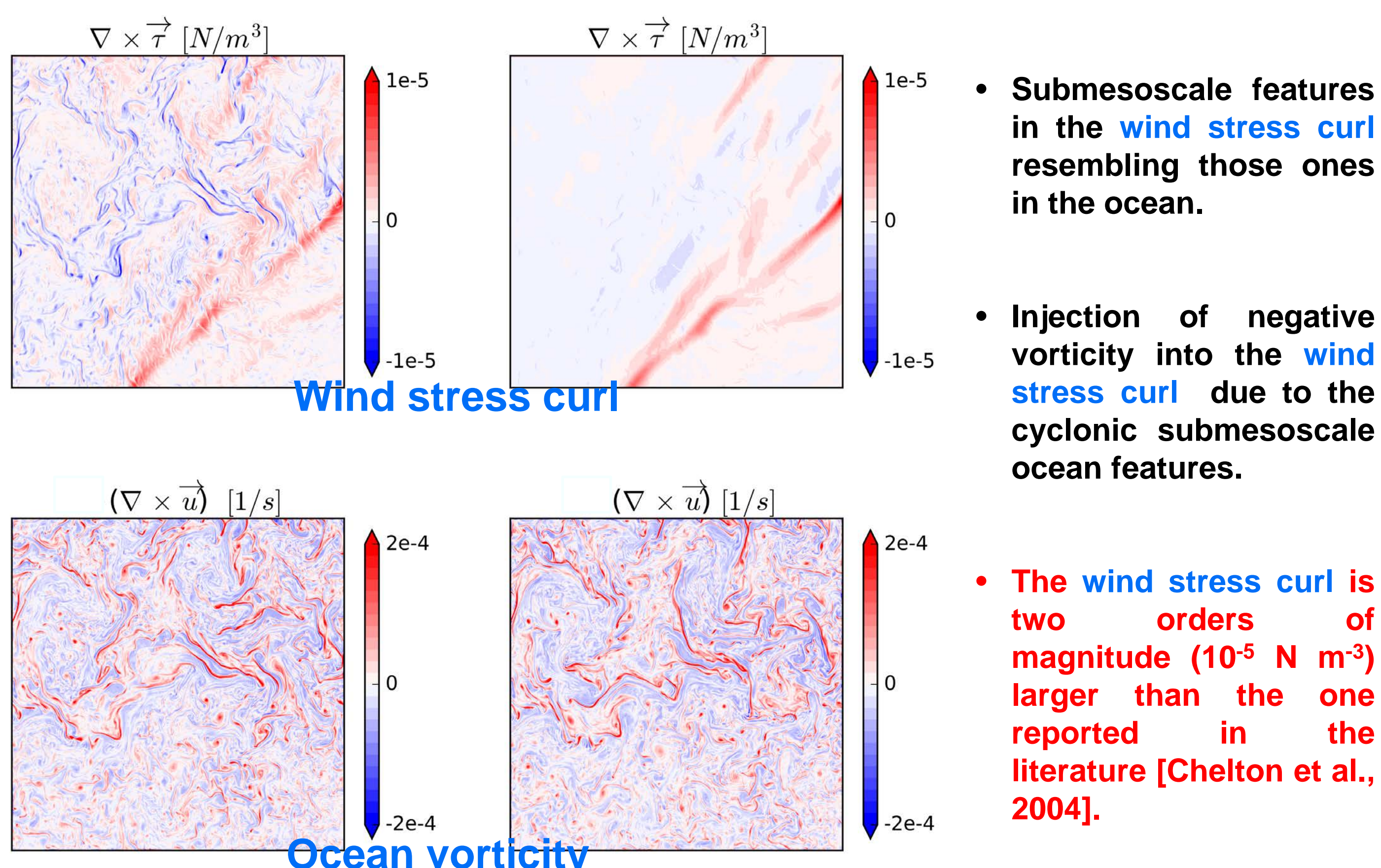


Figure 3. Wind stress curl (top panels) and ocean vorticity (lower panels): with current feedback (left column), without feedback (right panel).

- Submesoscale features in the **wind stress curl** resembling those ones in the ocean.

- Injection of negative vorticity into the **wind stress curl** due to the cyclonic submesoscale ocean features.

- The **wind stress curl** is two orders of magnitude (10^{-5} N m^{-3}) larger than the one reported in the literature [Chelton et al., 2004].

Results

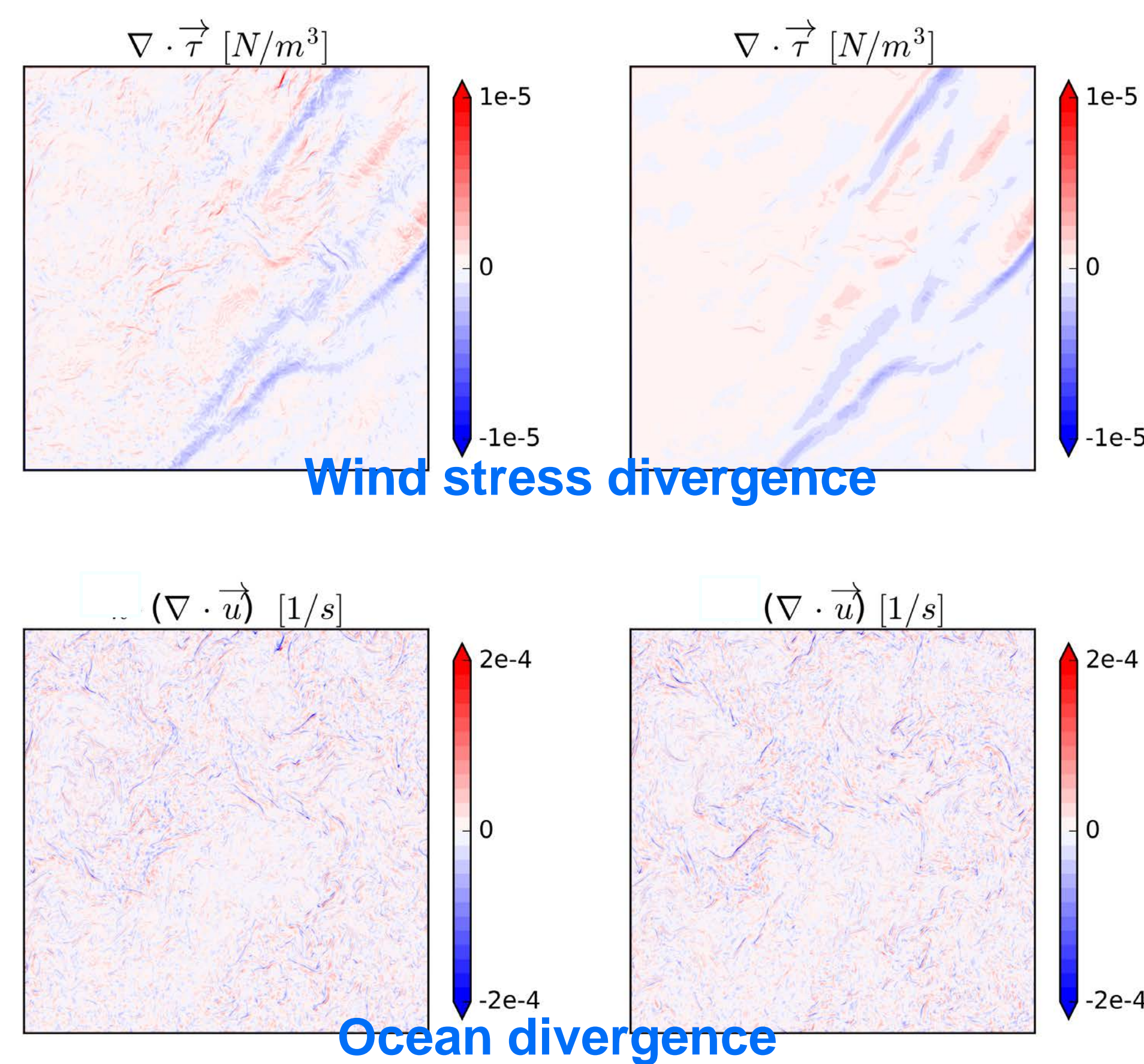


Figure 4. Wind stress divergence (top panels) and ocean vorticity (lower panels): with current feedback (left column), without feedback (right panel).

- Submesoscale features in the **wind stress divergence** resembling those ones in the ocean.

- Injection of positive divergence into the **wind stress divergence** due to a negative divergence in the ocean motions.

- The **wind stress divergence** is two orders of magnitude (10^{-5} N m^{-3}) larger than the one reported in the literature [Chelton et al., 2004].

Spectral analysis: The submesoscale ocean signature in the atmosphere allows to reach wavelengths smaller than 50 km, that are known to drive most of the vertical velocity in the ocean.

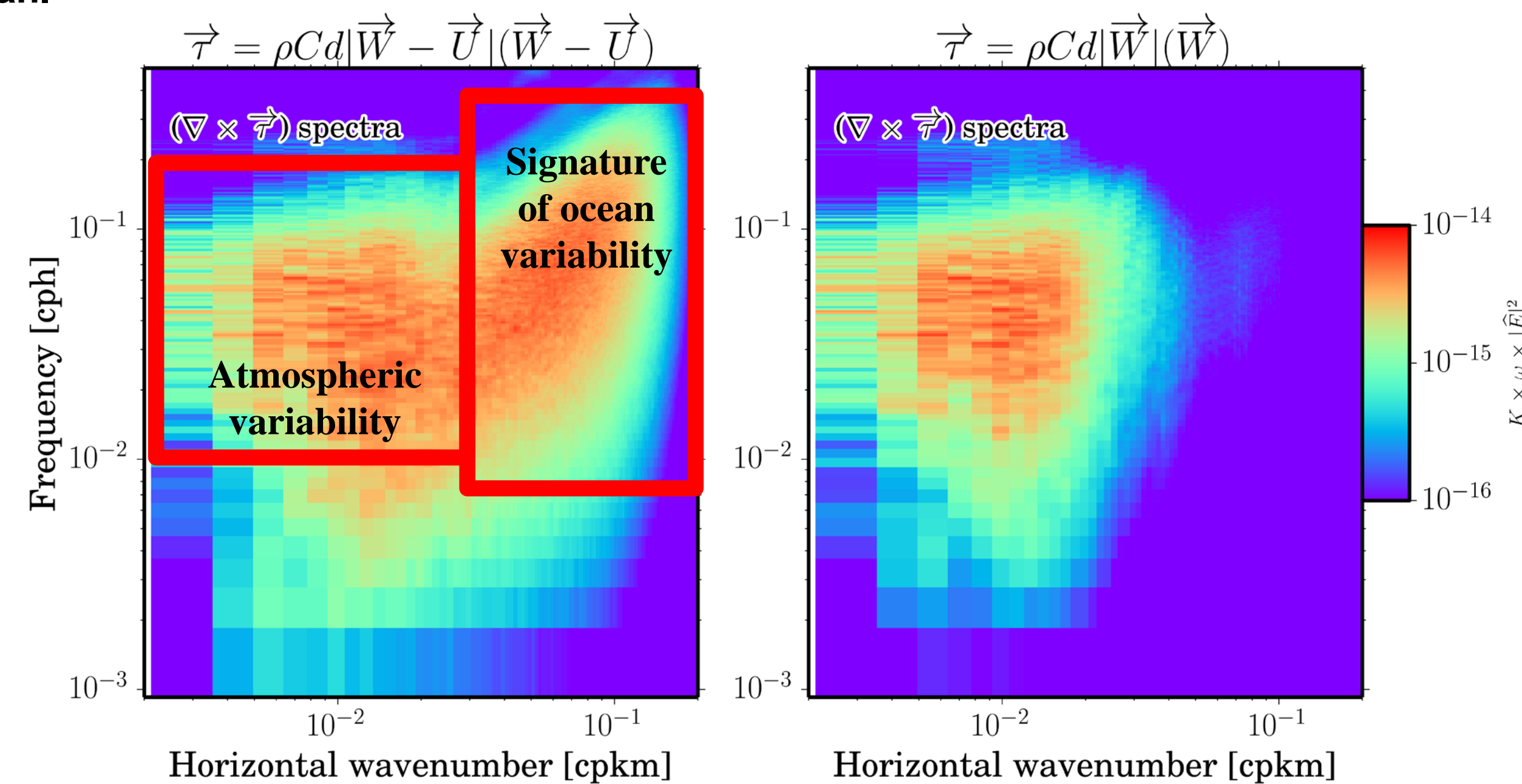


Figure 5. Frequency-wavenumber spectra of the wind stress curl: with surface current feedback (left column) and without surface current feedback (right column).

Summary

The ocean submesoscale motions are associated with large vertical velocity in the ocean, which in turn might have the same effect in the atmosphere.

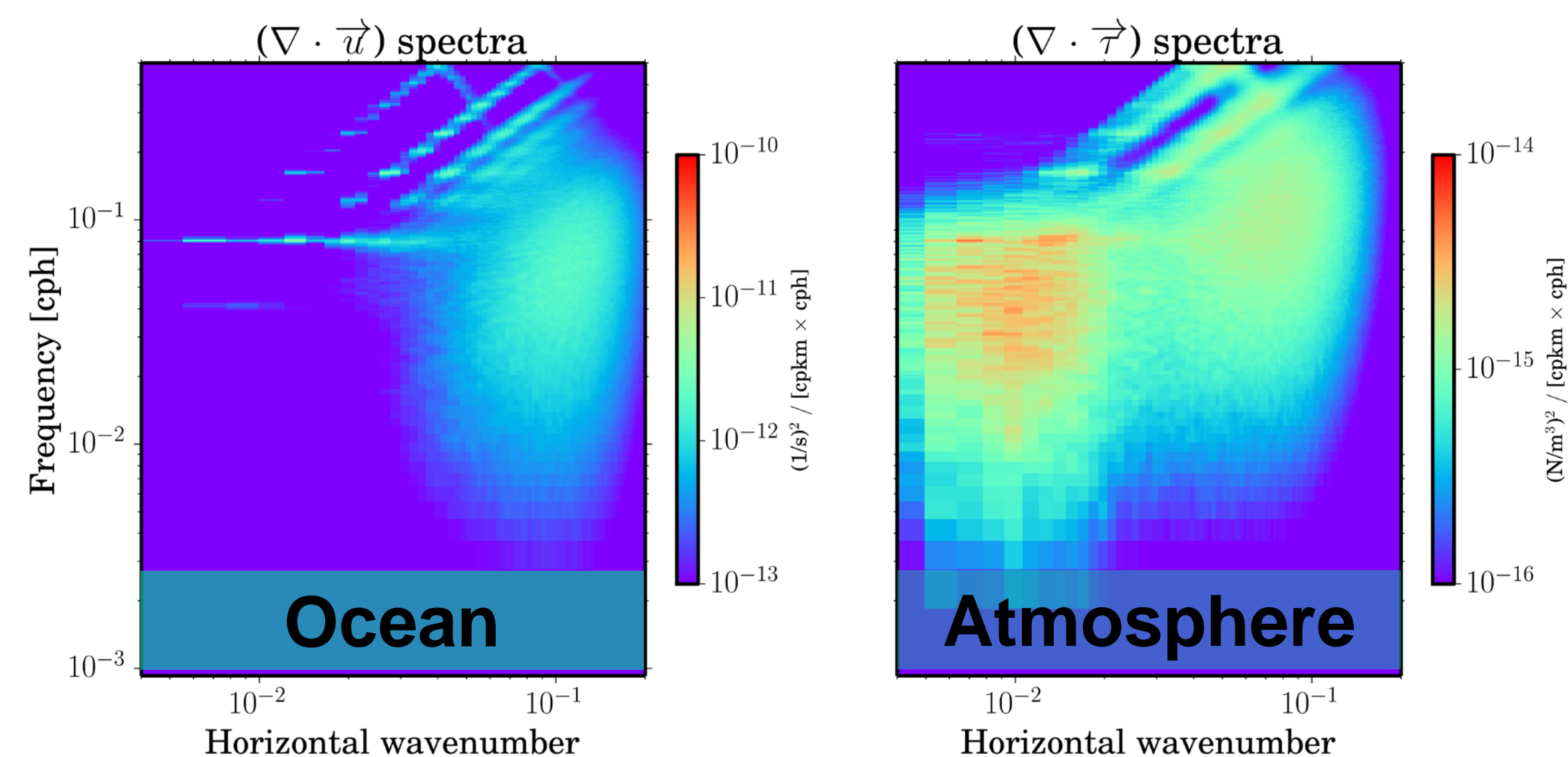


Figure 6. Frequency-wavenumber spectra of the ocean vertical velocity (left panel).

- These findings reveal that submesoscale ocean motions not only fully explain the vertical pump in ocean, might also explain a large part of the vertical pump in atmosphere.

- These findings are quite important for the air-sea interactions and therefore are of interest for science justification of a Winds and Currents satellite mission (WaCM). And also for future applications of SWOT observations.

Sensitivity of Hadley ascent and high clouds to warming and physical parameters in CESM

Author: Kathleen Schiro (329D)

Hui Su (329D), Baird Langenbrunner (UC Irvine), Yuan Wang (Caltech), Jonathan Jiang (329J), and J. David Neelin (UCLA)

Research Questions:

1. How do high clouds and their radiative effects interact with tropical circulation in present and future climate?
2. What physical processes are responsible for inter-model differences in climate model projections of tropical circulation and high cloud changes under global warming?

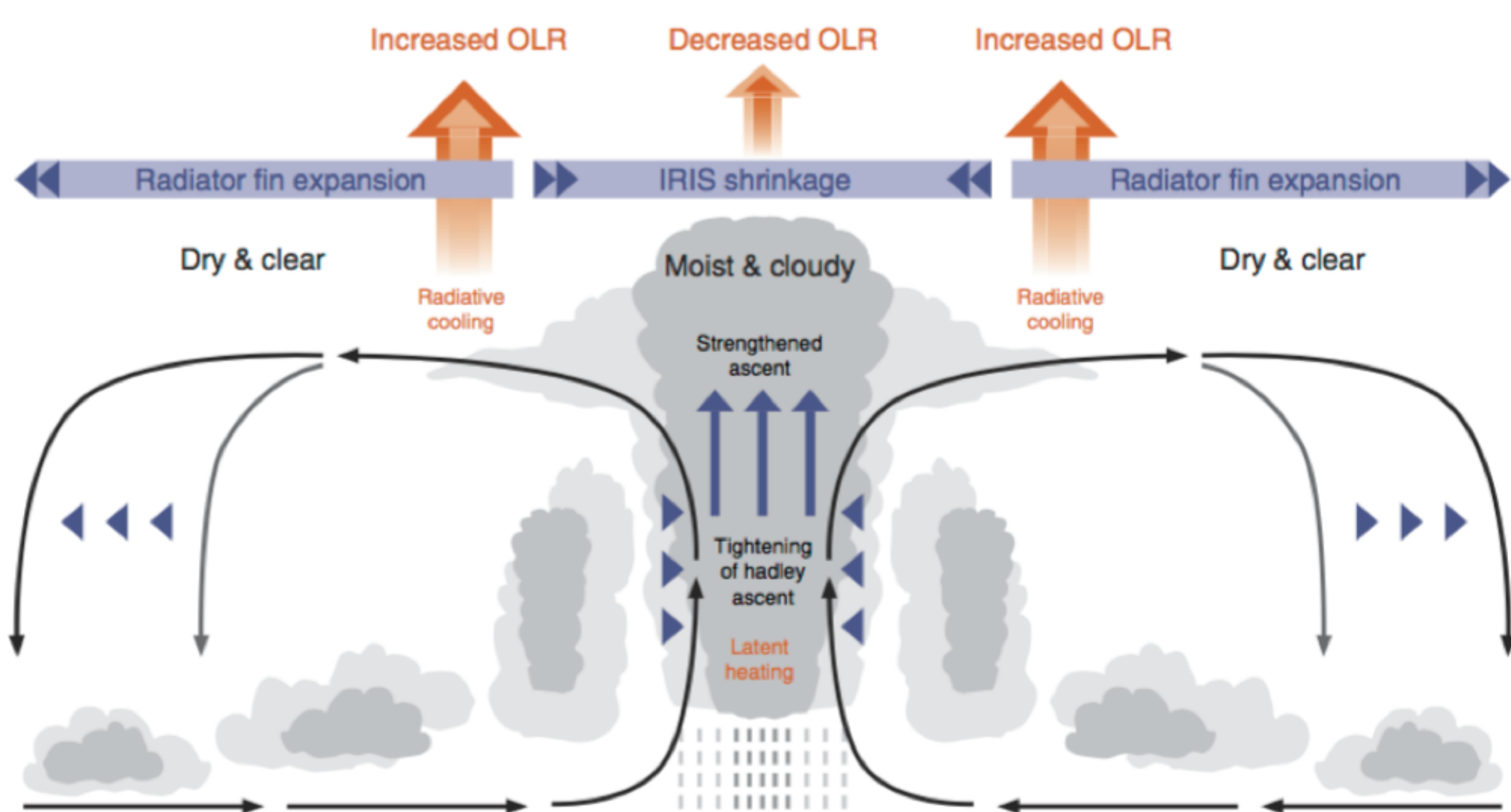
Motivation:

- Precipitation change under warming strongly coupled to change in outgoing longwave radiation (OLR; right)

$$L_v P = LWC - SH - SWA$$

P = precipitation rate
 L_v = latent heat of vaporization
 LWC = longwave cooling rate
 SH = sensible heat flux
 SWA = shortwave absorption

- Tropical mean OLR strongly coupled to tropical high clouds (depicted below)
- Understanding interactions between high clouds, circulation, and radiation key to observationally constraining changes in precipitation



Data and Methods

- Parameter perturbation experiments with atmosphere-only GCM (NCAR CAM5.3)
 - One parameter per run, 2-5 values perturbed
- Cloud, circulation, and precipitation changes (20°S-20°N) regressed onto tropical mean surface temperature
- Permits exploration of physics governing circulation changes with warming

Category

convection

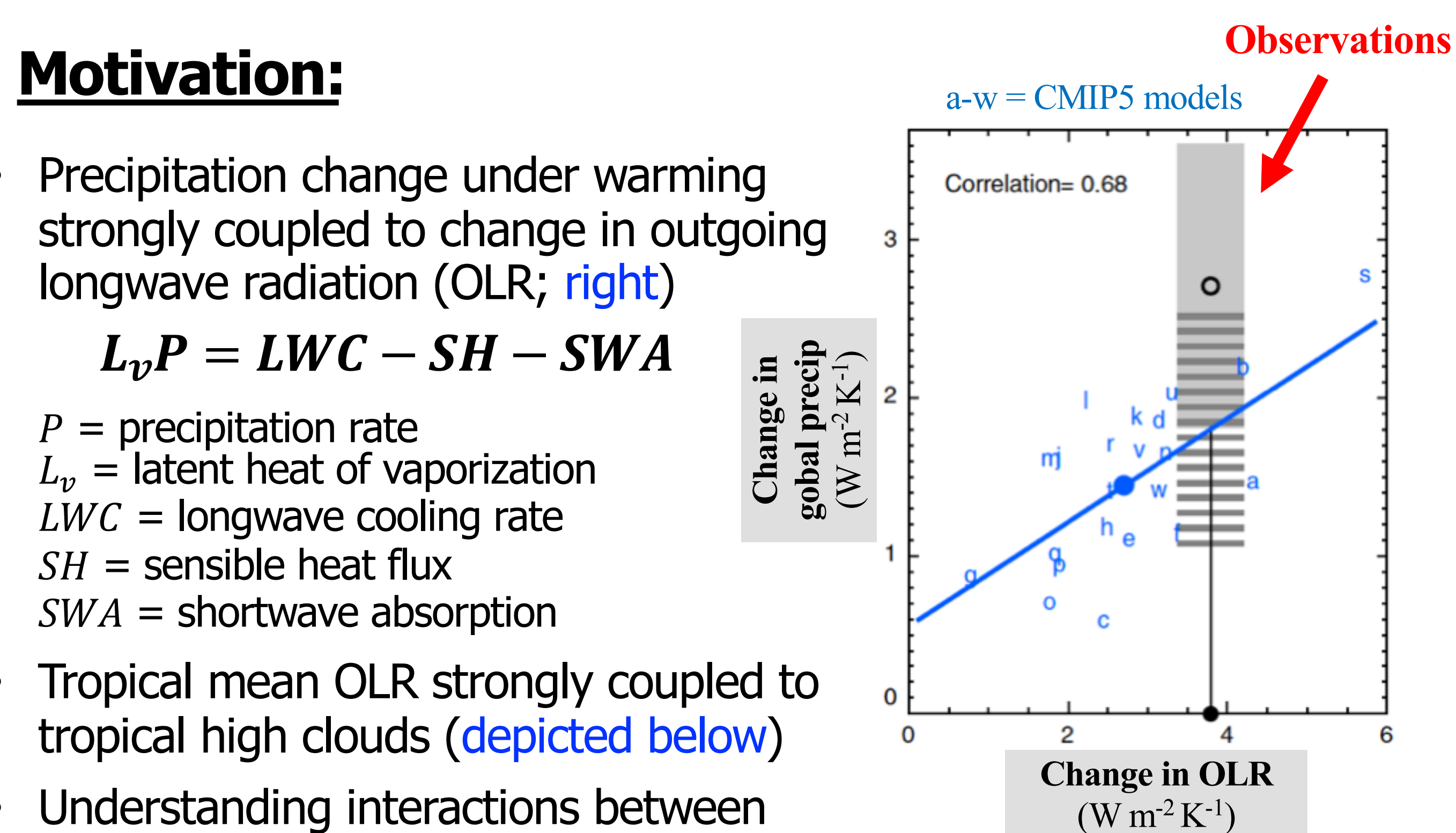
Description

Fractional rate of entrainment
Downdraft fraction
Convective timescale
Evaporation efficiency

microphysics

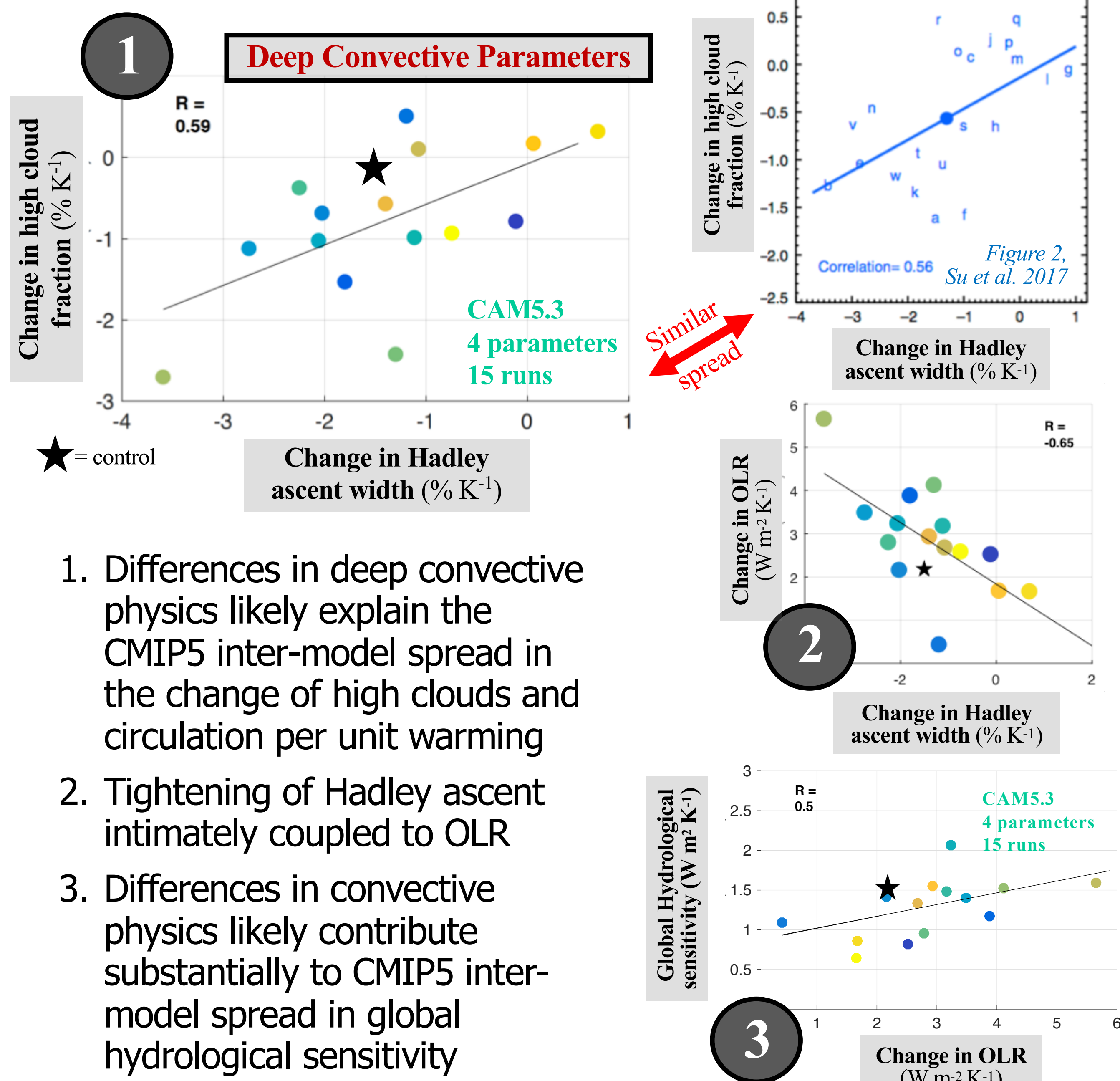
Threshold RH for high clouds
Threshold RH for low clouds
Fall speed for stratiform ice
Fall speed for stratiform snow
Autoconversion size ice - snow
Collection efficiency, ice
Inverse variance of cloud water
Max w for ice nucleation
Min w for liquid nucleation
Radius of detrained ice

Analysis period: 1995-2005

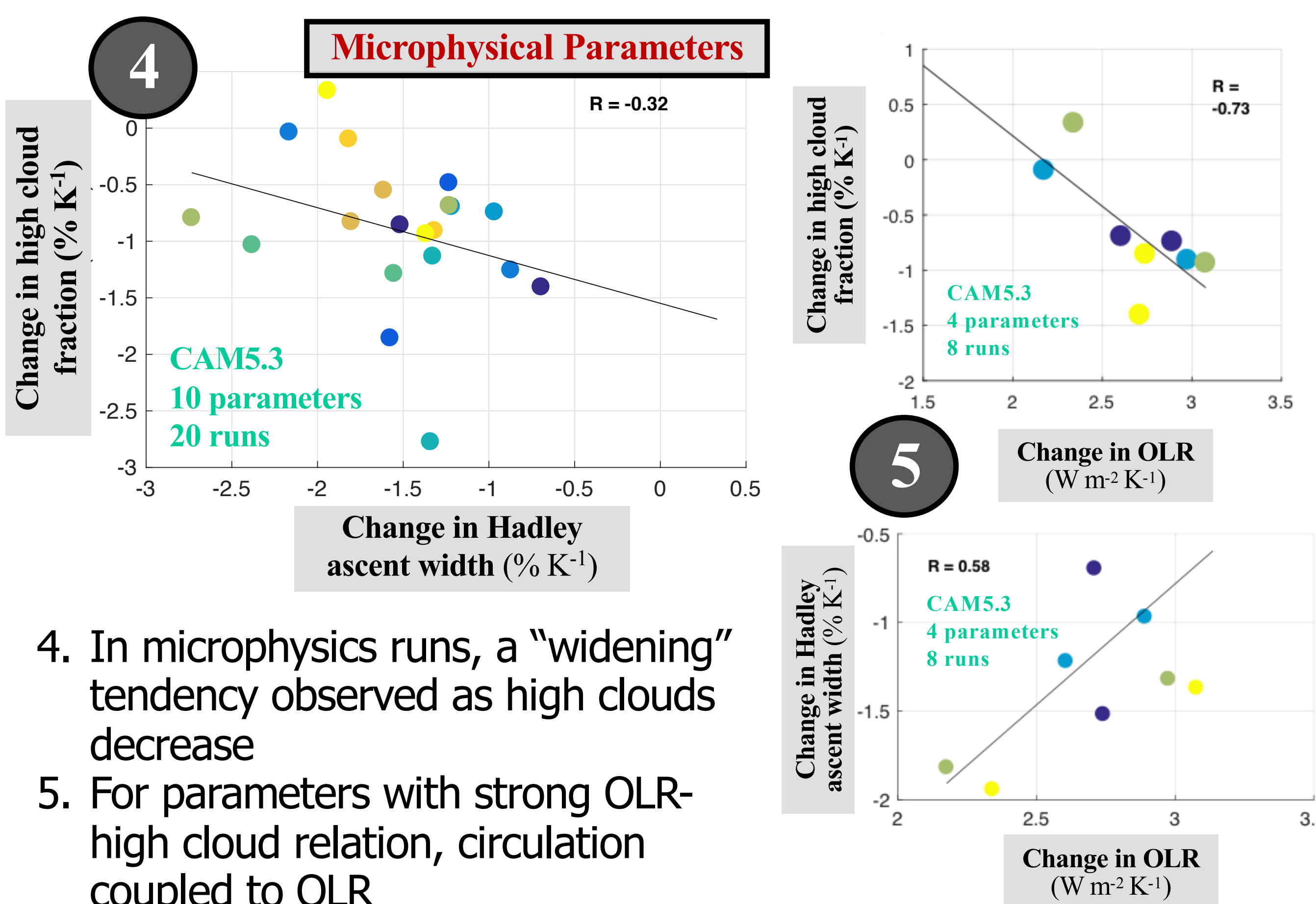


Figures 1 (bottom) and 4a (top) Su et al. 2017, Nat. Comm.

Results



1. Differences in deep convective physics likely explain the CMIP5 inter-model spread in the change of high clouds and circulation per unit warming
2. Tightening of Hadley ascent intimately coupled to OLR
3. Differences in convective physics likely contribute substantially to CMIP5 inter-model spread in global hydrological sensitivity



4. In microphysics runs, a "widening" tendency observed as high clouds decrease
5. For parameters with strong OLR-high cloud relation, circulation coupled to OLR

Conclusions

- Deep convective physics likely contribute substantially to CMIP5 inter-model spread in response of high clouds, Hadley ascent tightening, and global precipitation to warming
- Circulation and clouds intimately coupled through OLR
- Satellite observations can be used effectively to constrain physical parameters in climate models within emergent constraint framework

Acknowledgments:

Funding for this project was provided by NASA NEWS and ACMAP-AST.

Evaluating Convective Entrainment Rates Associated with Deep Convection Simulated by GEOS5 Using Aura CO and CloudSat Observations

Author : Ryan Stanfield (329D)

Hui Su (329D), Jonathan Jiang (329J), Lei Huang (329D), Zhengzhao Johnny Luo (CCNY), Saulo Freitas (NASA Goddard), Andrea Molod (NASA Goddard), Ming Luo (329I)

1. Introduction / Motivation

Problem: As convection usually occurs at horizontal scales smaller than the grid sizes of general circulation models (GCMs), the effects of convection are represented statistically through the use of parameterizations as functions of resolved atmosphere state variables.

The most common way to parameterize convective transport is through mass flux schemes. A key process that modifies the mass flux is the mixing between convective plumes and their environment by entrainment and detrainment processes that describe, respectively, the inflow of environmental air into the convection and the outflow from the convective column into the environment.

A number of studies have documented the strong sensitivity of model performances in precipitation, cloud, and trace gases to entrainment rate (ER) parameterizations.

Objective: Improve the simulation of convection and its impacts through observational constraints on one of the most uncertain and important model physical parameters, the entrainment rate.

4. Conclusions

- Estimated entrainment rates (ER) are predominantly found to be less than 20 % / km. Observations show a monotonic decrease in estimated ERs, while GEOS5 estimated and given ERs peak at 5 - 10 % (Figure 2).
- Observed estimated ERs decrease with increasing cloud top height (Figure 3).
- Observed estimated ERs decrease with increasing Relative Humidity (RH; Figure 4).
- Observed estimated ERs decrease with increasing Convective Available Potential Energy (CAPE; Figure 5).

5. Benefit to JPL

Our research further demonstrates the value of NASA observations by providing us a framework in which we can improve climate model physics through better simulation of entrainment rates associated with deep convection.

2. Methodology

Plume Model: We use an entraining plume model and CO concentrations from AURA TES/MLS and the GEOS5 simulation as a tracer to estimate Entrainment Rate (ER) using Equations (1) and (2) as well as some assumptions.

Eq. 1 : Mass Flux

$$\frac{\partial \eta(z)}{\partial z} = \sigma$$

Eq. 2 : Carbon Monoxide Concentration

$$CO_{parcel}(z + \Delta z) = \frac{CO_{parcel}(z) + \sigma \Delta z CO_{environment}(z)}{(1 + \sigma \Delta z)}$$

where,

- $\eta(z)$ = the normalized mass flux at height (z) relative to cloud base,
- σ is the entrainment ratio (%/km),
- and Δz is the height change between different pressure levels.

Cloud tops are identified using CloudSat for observational cases (Figure 1) and by the maximum of the detraining flux profile for the GEOS5 simulation (not shown here).

The Level of Maximum Detrainment (LMD) is identified as the maximum of the CO concentration profile within 150 mb of the identified cloud top if one exists, otherwise the previously determined cloud top height is used.

The ER estimated by the plume model is identified as the rate needed for good agreement between the estimated and observed CO concentrations at the LMD. ERs provided by the GEOS5 simulation are taken at the LMD height.

3. Results

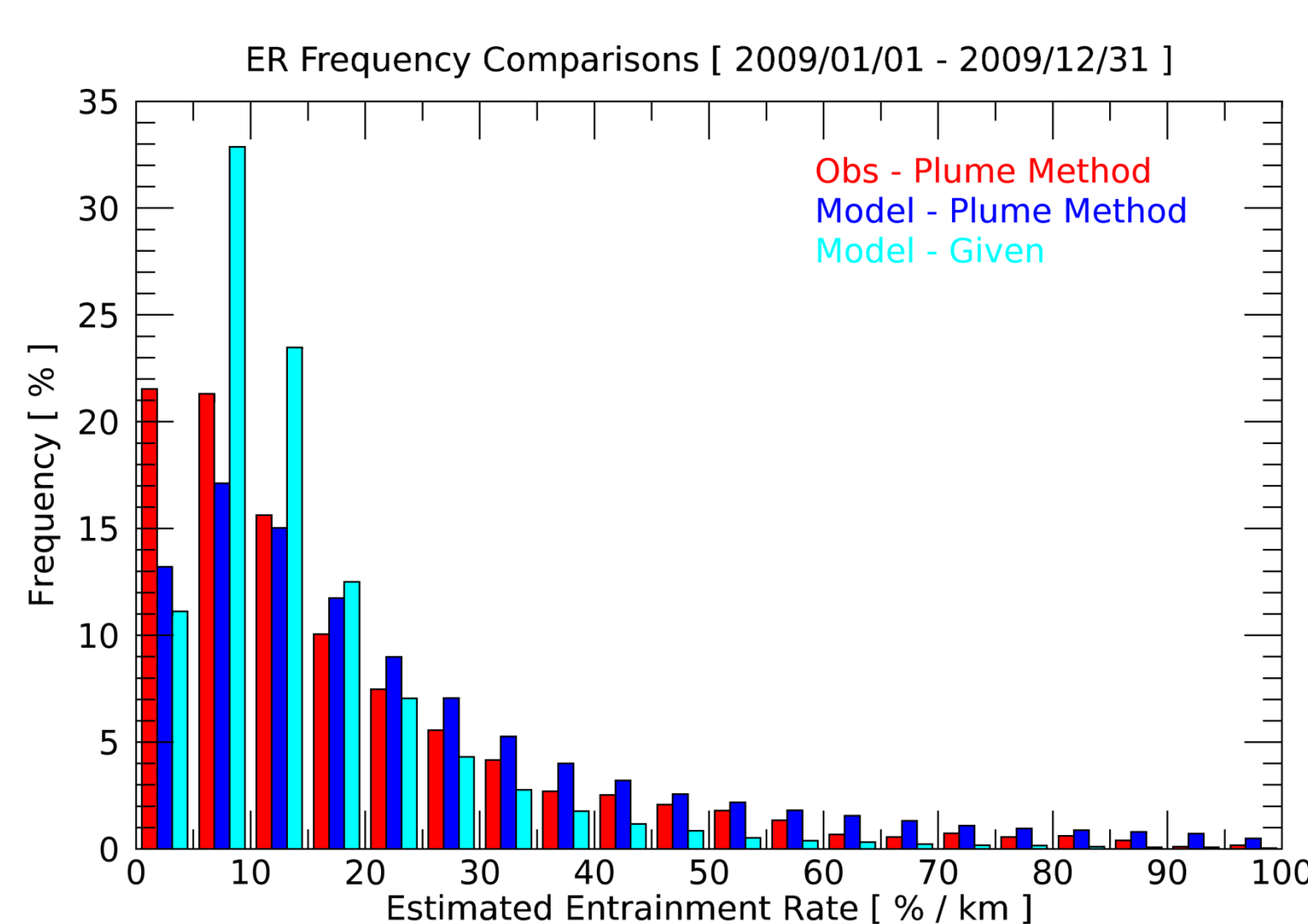


Figure 2. Frequency of plume model estimated ERs using MLS/TES CO observations and GEOS5 plume estimated and simulated ERs binned at every 5%.

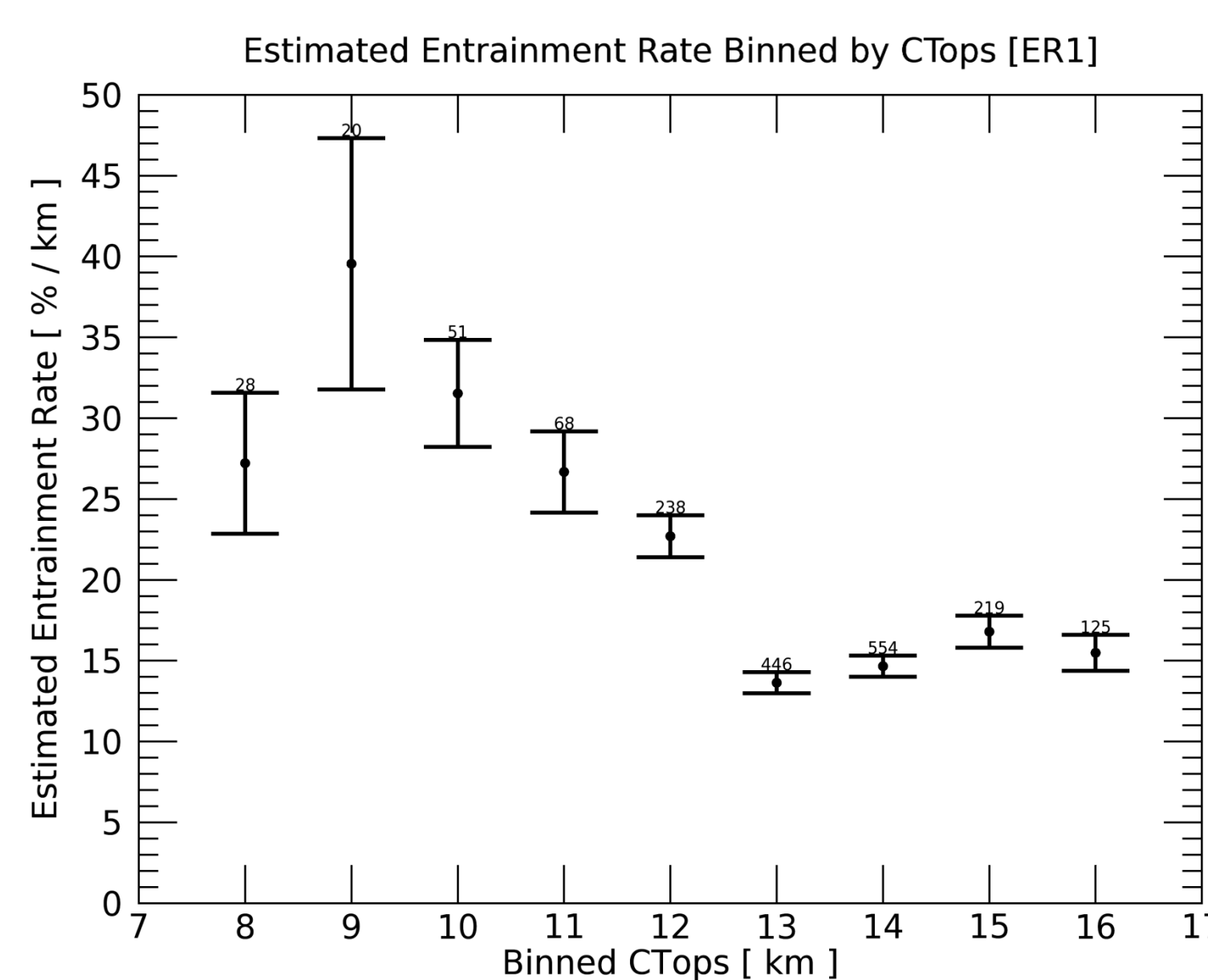


Figure 3. Spread of observed estimated ERs, when binned by cloud top height at every kilometer. The spread is given as the standard deviation divided by the root number of samples within each bin (standard error).

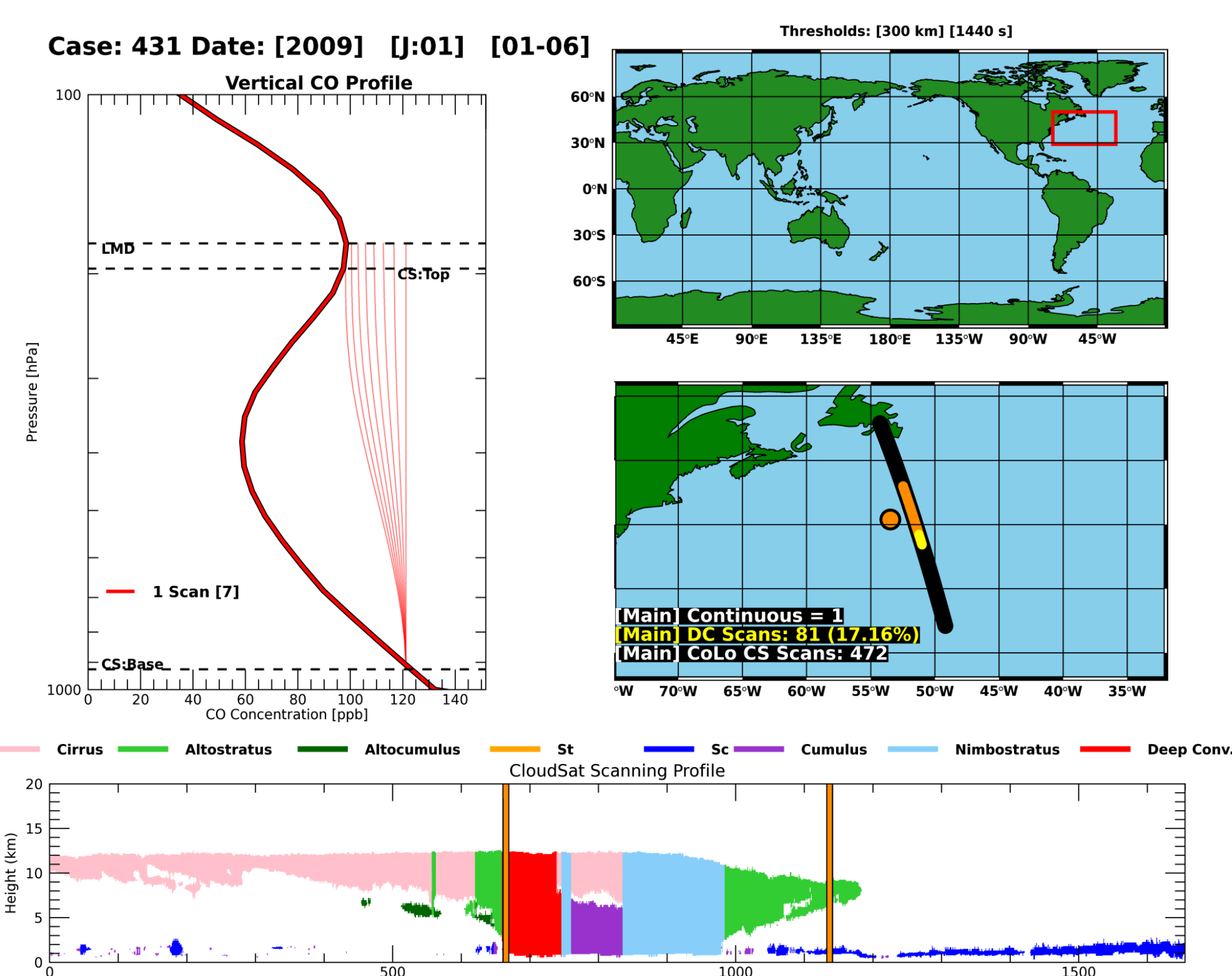


Figure 1. A sample case where an entrainment ratio is estimated by applying our plume model (soft red lines) to the local AURA TES/MLS CO profile (dark red line) where CloudSat identified deep convection (red, bottom panel).

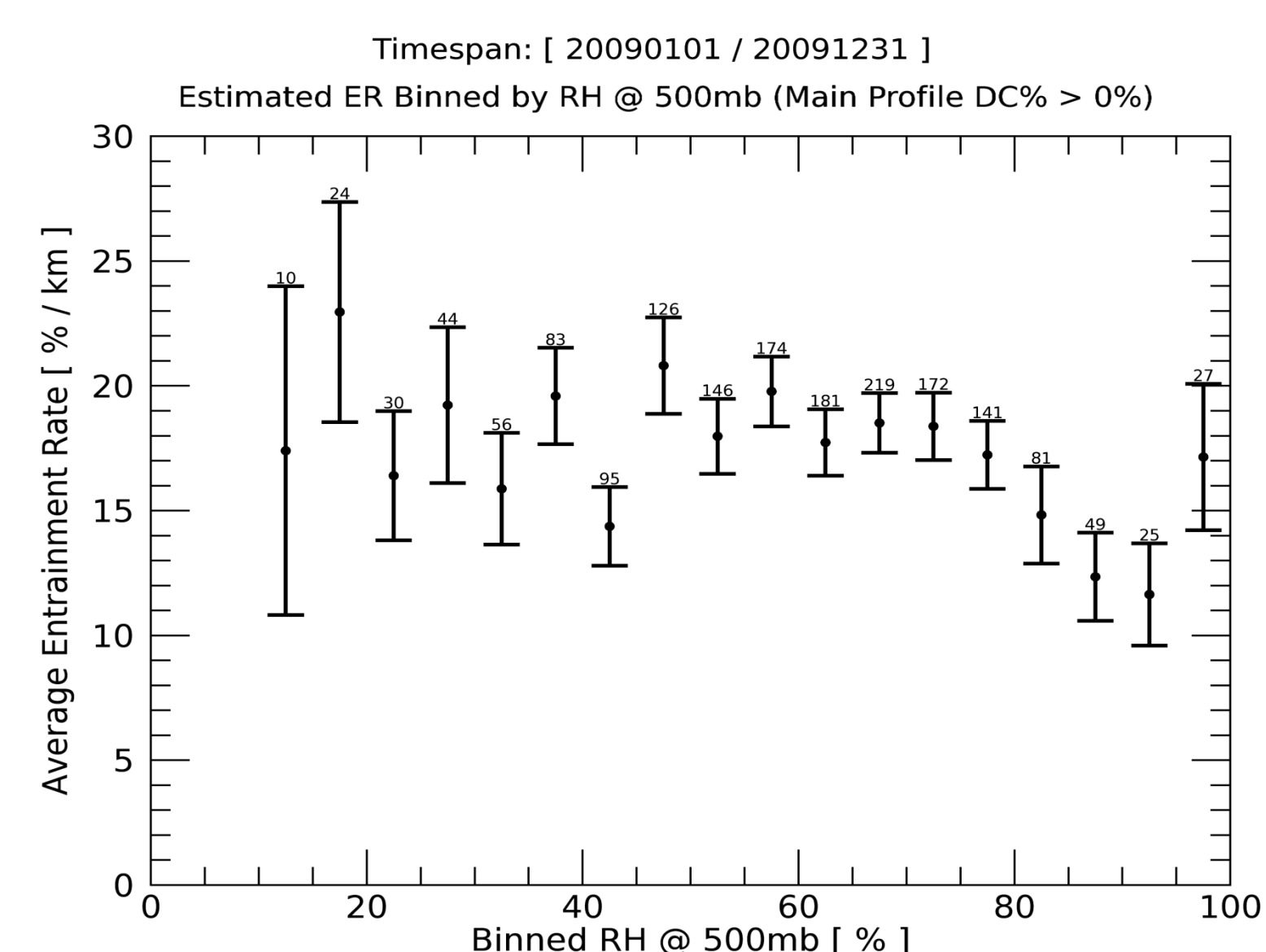


Figure 4. As in Figure 3, except for Relative Humidity at 500 mb (RH) and binned for every 5% RH. The number of samples in each bin is listed above.

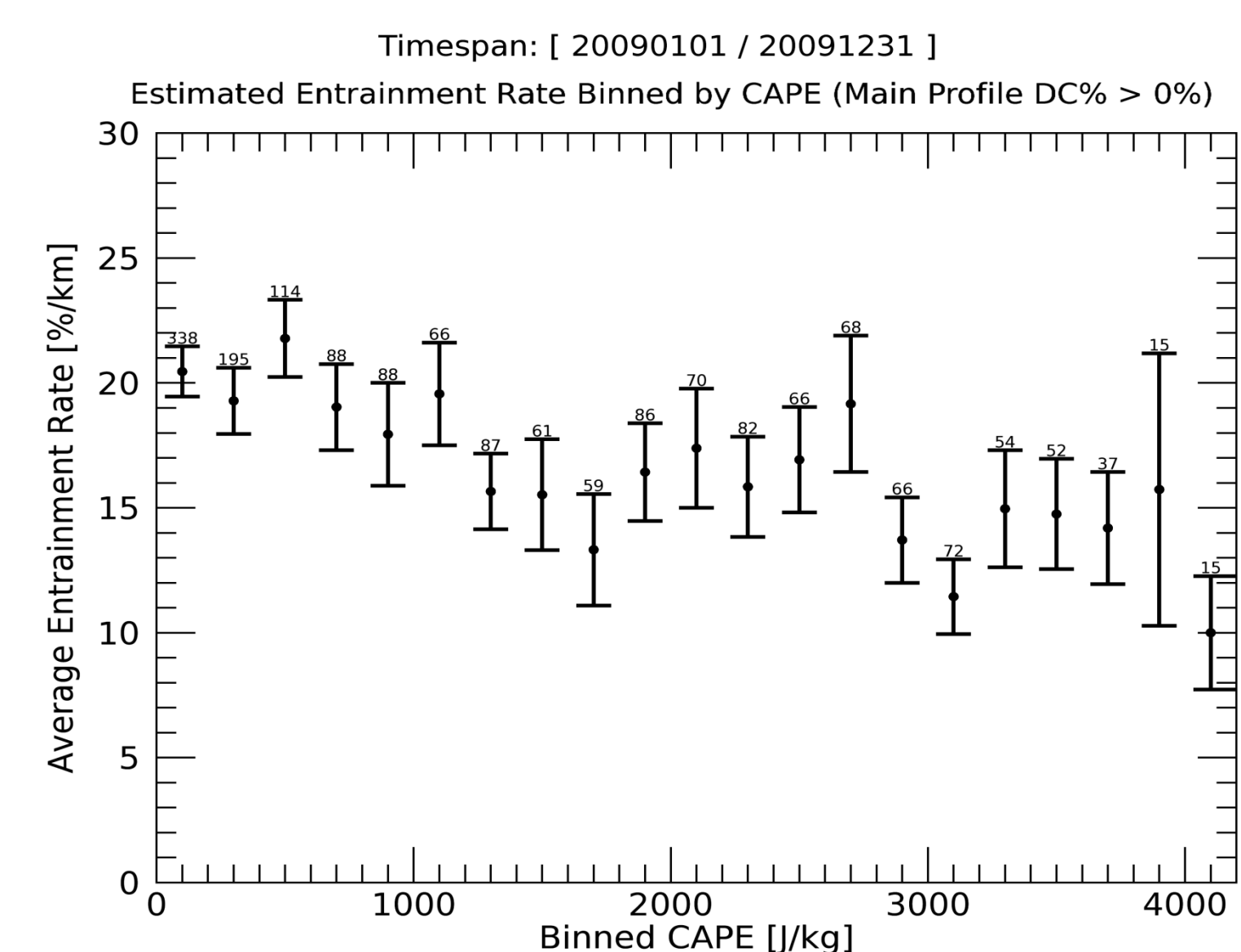


Figure 5. As in Figure 3, except for Convective Available Potential Energy (CAPE) and binned for every 200 J/kg.

Constraining bulk microphysics warm-rain autoconversion rates with radar reflectivity and cloud droplet effective radius data

Anna Jaruga (329E), Marcin Witek (329J), Joao Teixeira (3292), Tapio Schneider (Caltech)

Objectives:

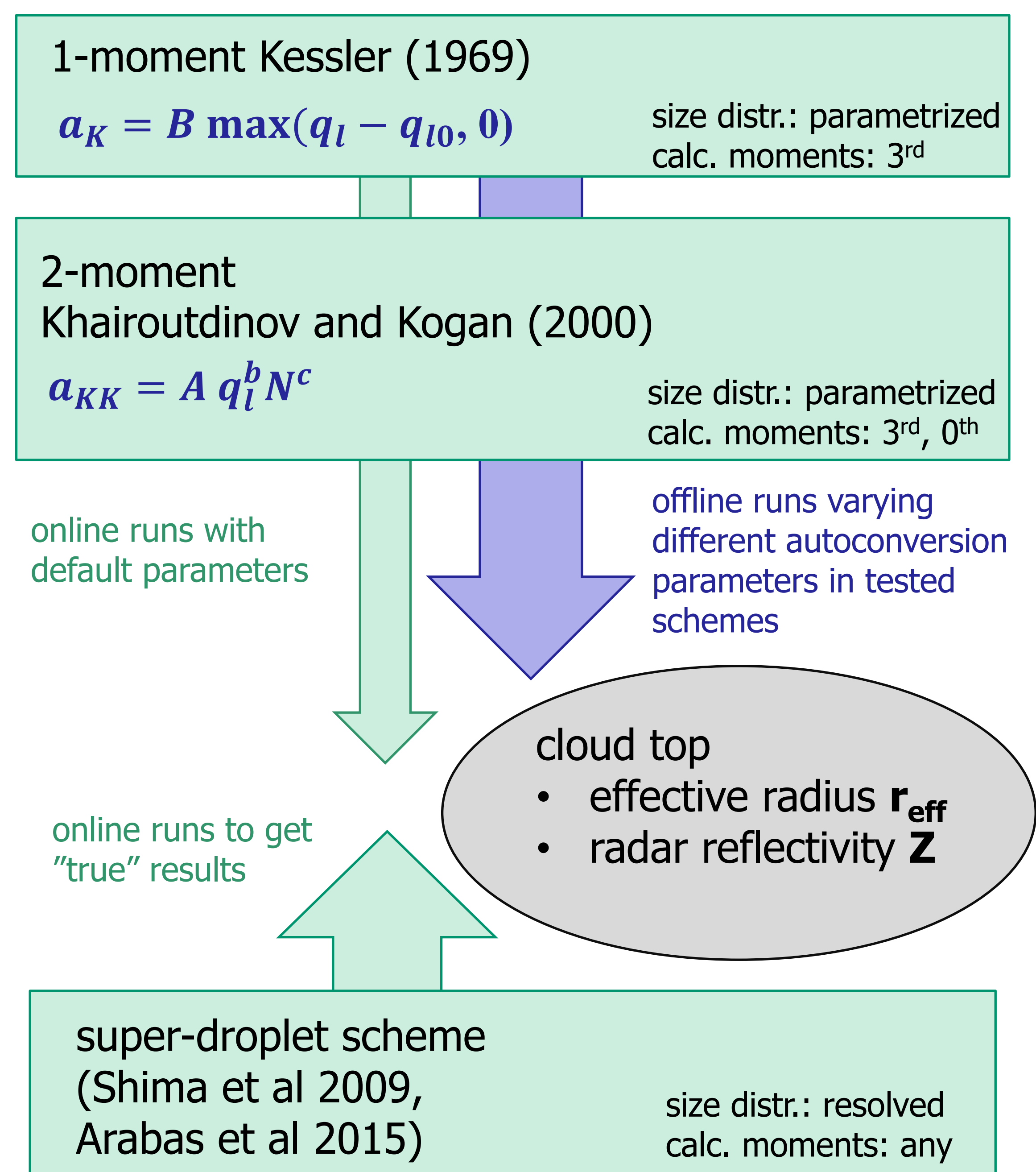
Improving the representation of warm-rain precipitation in numerical models

Introduction:

- Global Climate Models (GCM) have biases related to warm-rain compared to satellite observations.
- One of the reasons is the autoconversion rate (the rate of conversion of cloud water to rain water) calculated by the microphysics schemes in GCMs

Methodology:

- 2D Large Eddy Simulations (LES) of Sc (DYCOMS)



Next steps:

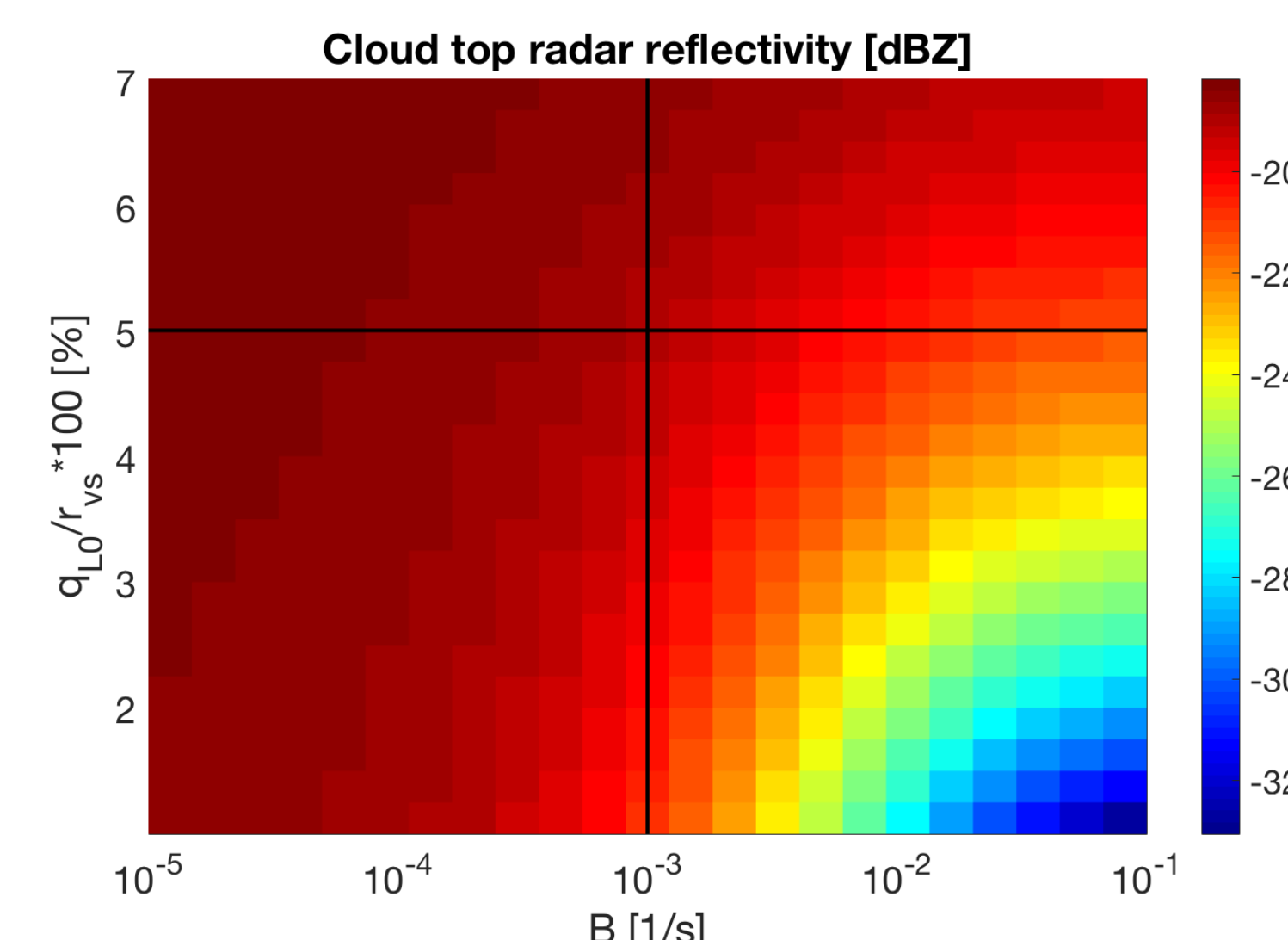
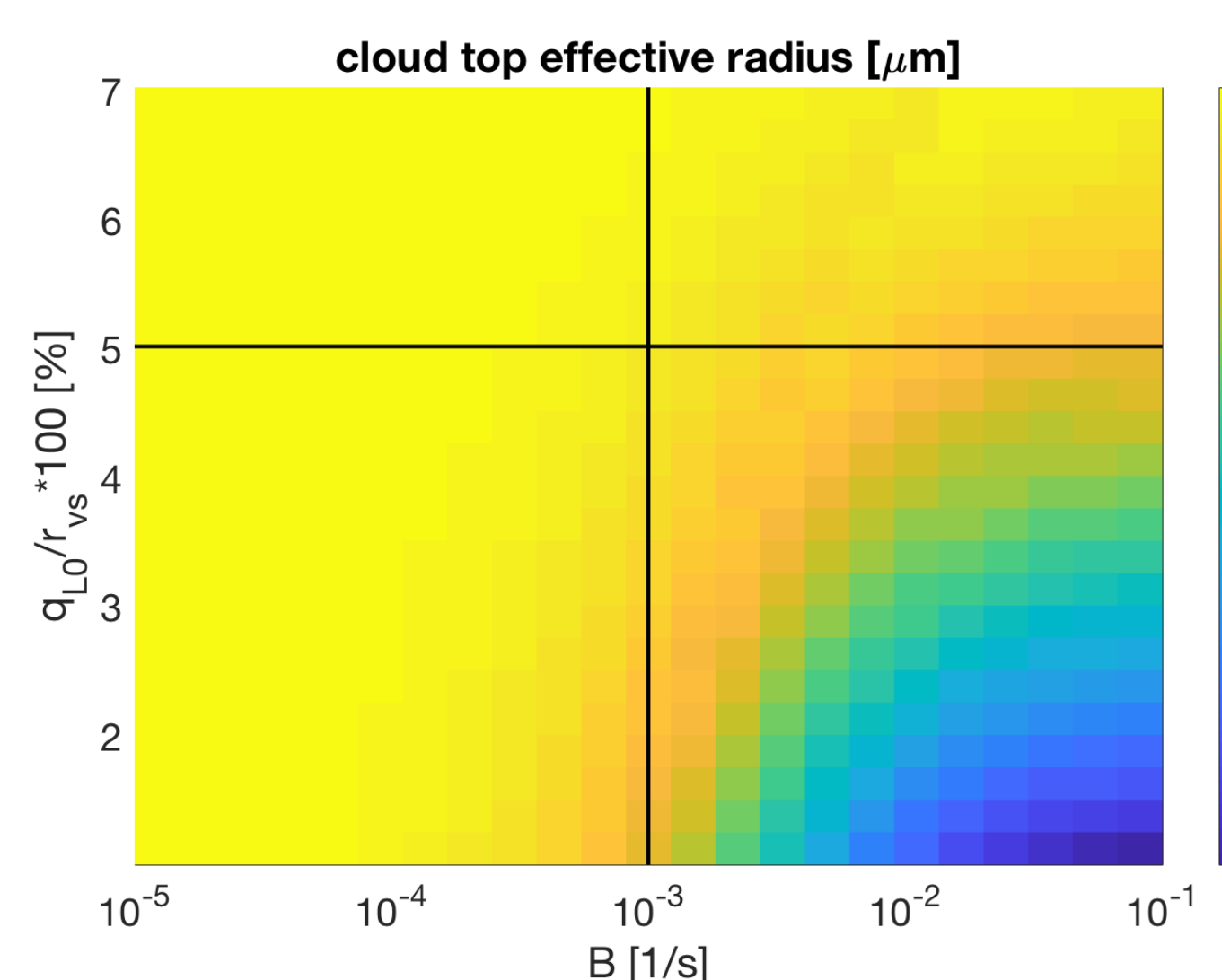
- Different setups: Cu - RICO
- Different assumed size distributions for 2-moment scheme
- Additional observables – max. rain, total rain
- Combine with satellite observations

Results: autoconversion parameters landscape

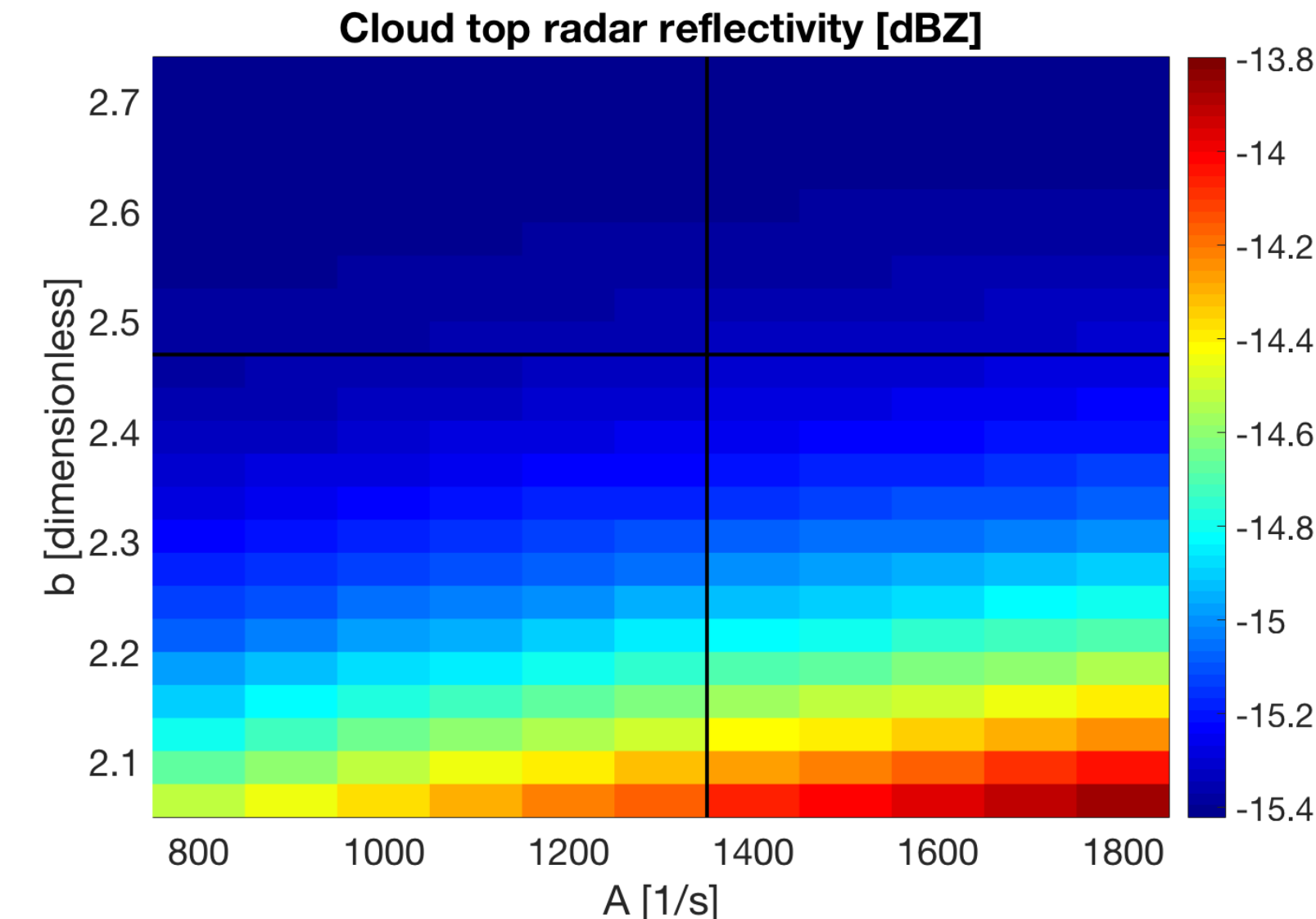
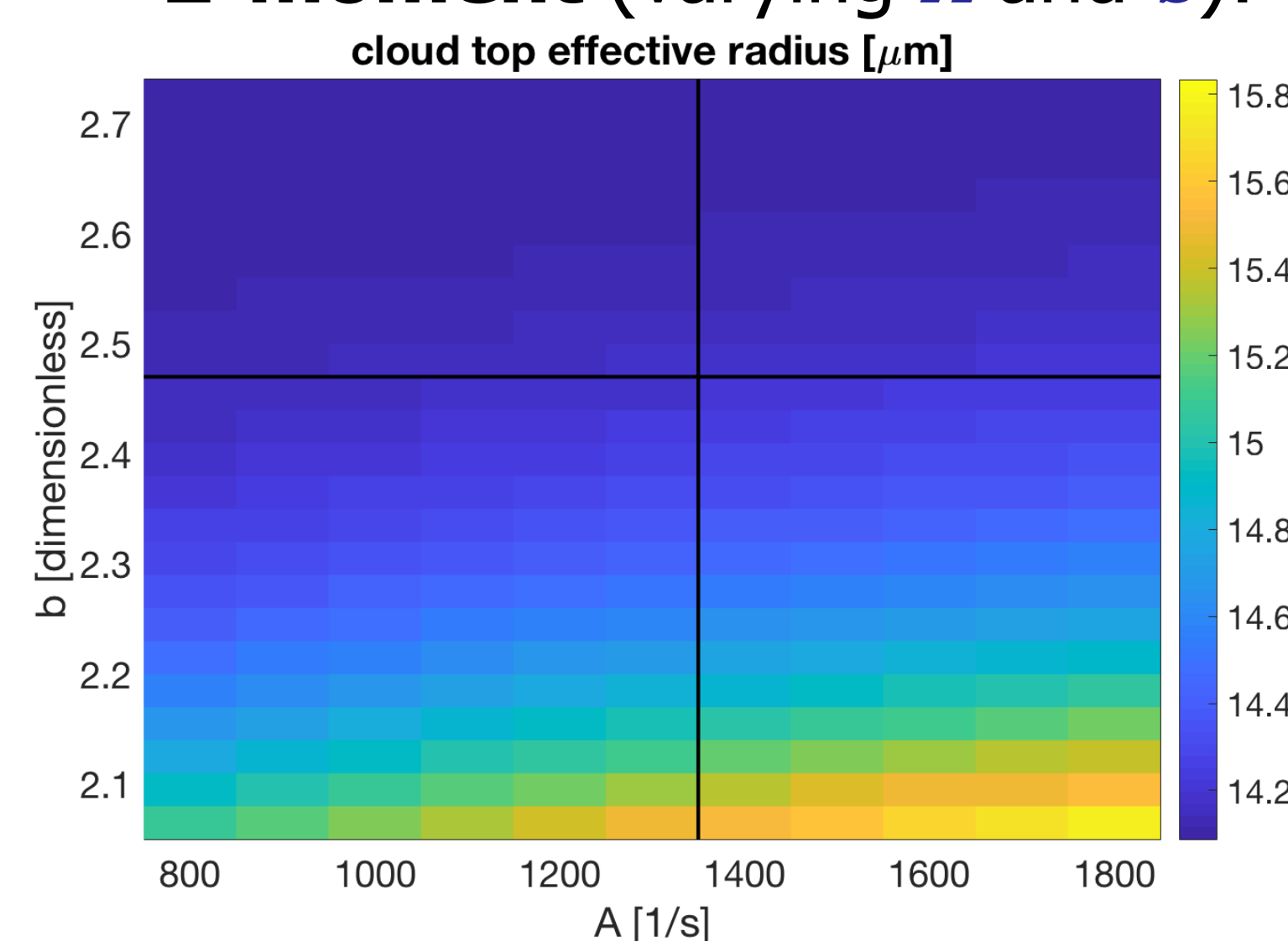
super-droplet "truth":

$$r_{\text{eff}} = 10.7 \mu\text{m} \quad Z = 0.6 \text{ dBZ}$$

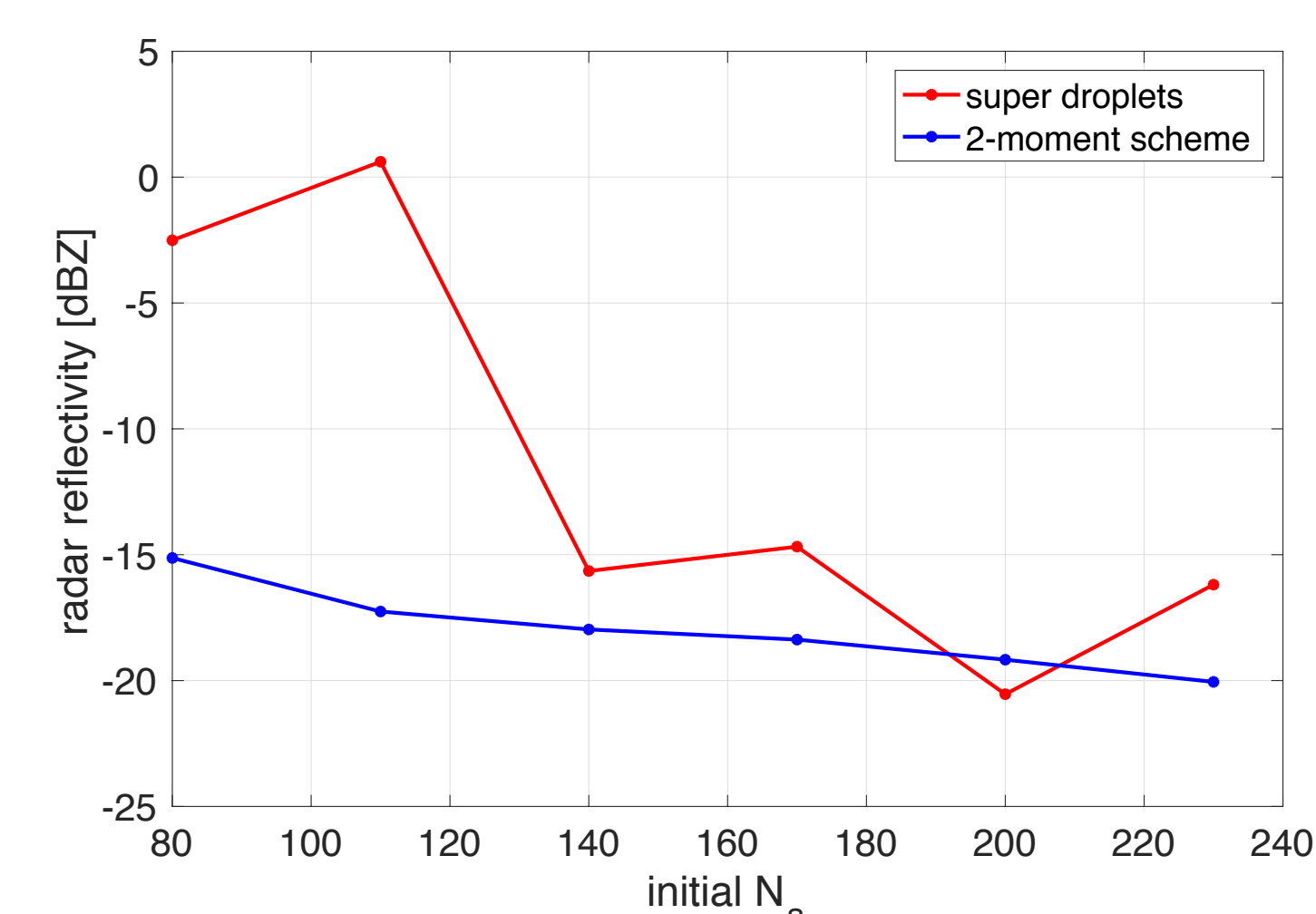
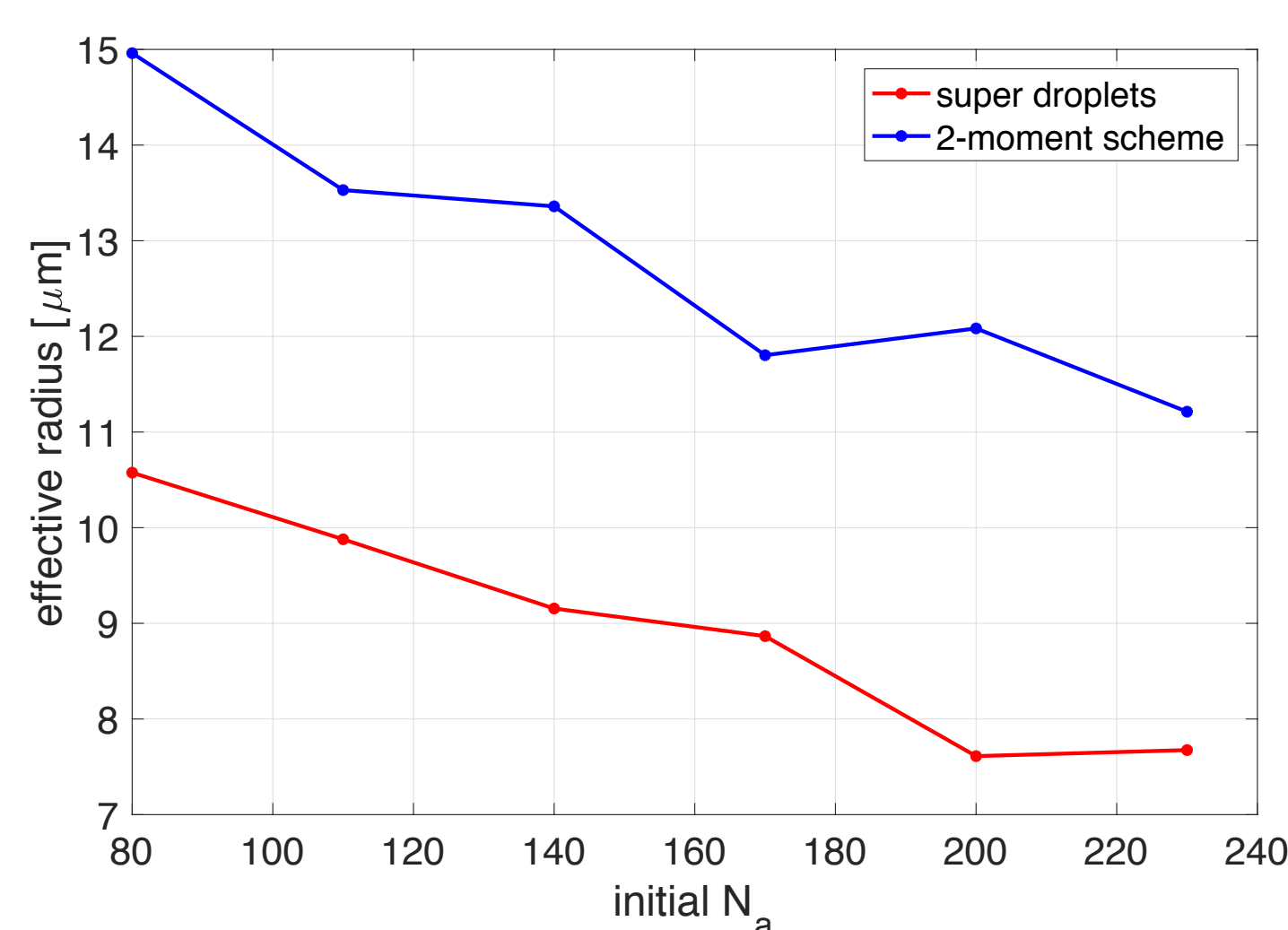
1-moment (varying q_{l0} and B):



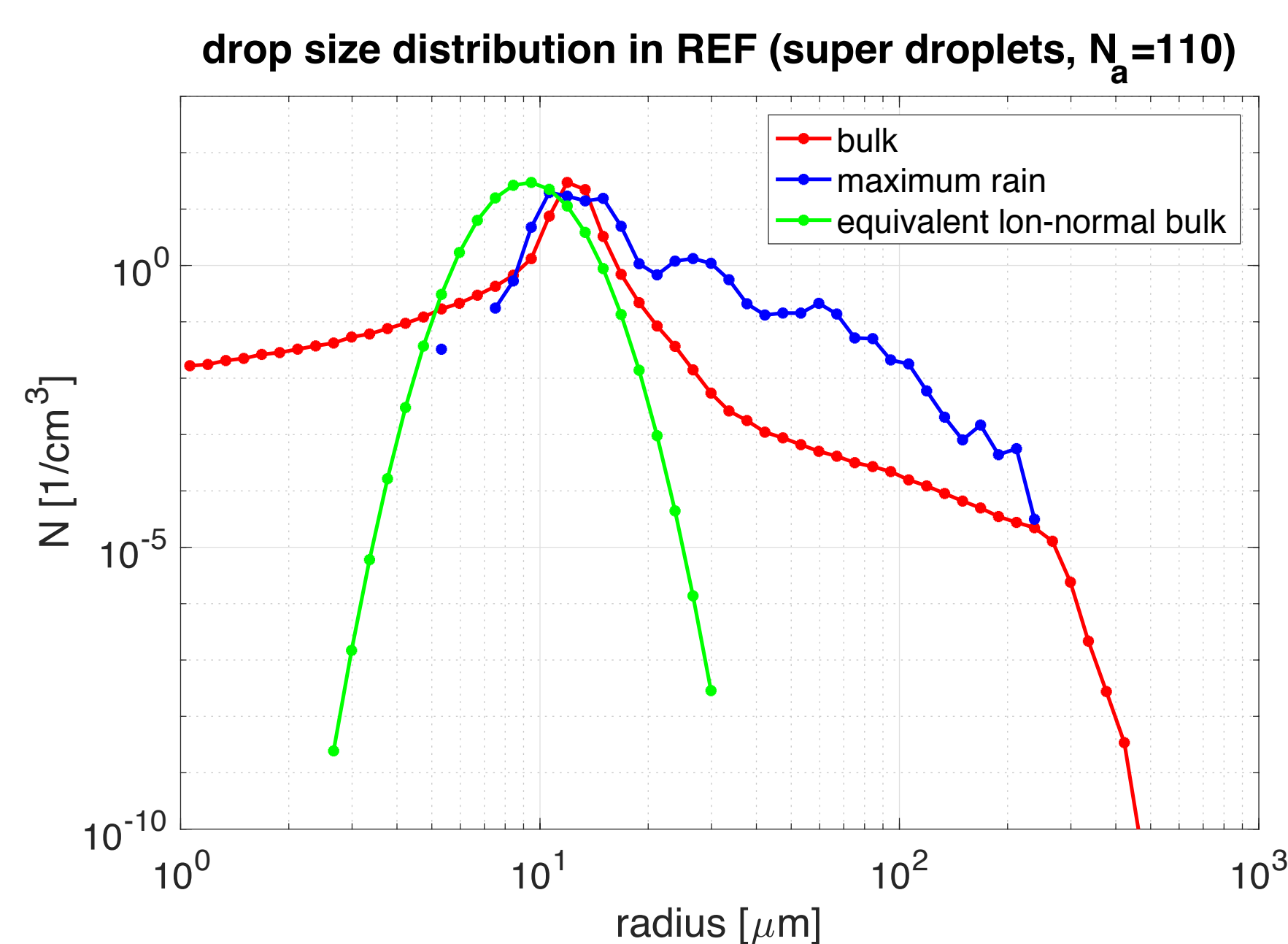
2-moment (varying A and b):



Results: aerosol impact on 2-moment scheme



Results: droplet sizes



Conclusions:

- Big differences between the two schemes and the "truth"
- ... and between the two schemes themselves
- A set of autoconversion parameters that is good for predicting r_{eff} might result in a decrease of accuracy for Z
- The assumed droplet distribution shape is critical

Evaluating precipitation extremes in regional climate models relative to a 'cloud' of observational uncertainty

Peter Gibson (JPL, 329-F)
Duane Waliser (JPL, 8000)

Context

Problem:

Climate models are routinely evaluated against observational products. Typically, observational differences \ll model differences so a single observational product can be reliably used. However, in some regions, observational uncertainty in precipitation is not trivial which makes model evaluation challenging.

Objectives:

- Investigate observational uncertainty in the tails of precipitation over CONUS (in-situ, satellite, reanalysis)
- Implement dimension reduction tools to evaluate/visualize model skill relative to the 'cloud' of observational uncertainty

Data

- 10 'Observational' products analyzed: In-situ (CPC-Unified, PRISM, Daymet); Satellite (TRMM, GPCP, PERSIANN); Reanalysis (MERRA-1, MERRA-2, ERA-INT, NARR)
- 30 Regional climate model simulations from NA-CORDEX. Includes reanalysis-driven and GCM-driven runs

Precipitation indices

WCRP's ETCCDI annual indices:

- CWD = consecutive wet days
- CDD = consecutive dry days
- SDII = average precipitation on wet days
- r10/20mm = number of wet days above 10/20mm threshold
- rx1day/rx3day = maximum 1 or 3-day precipitation totals per year
- prcptot = total yearly precipitation

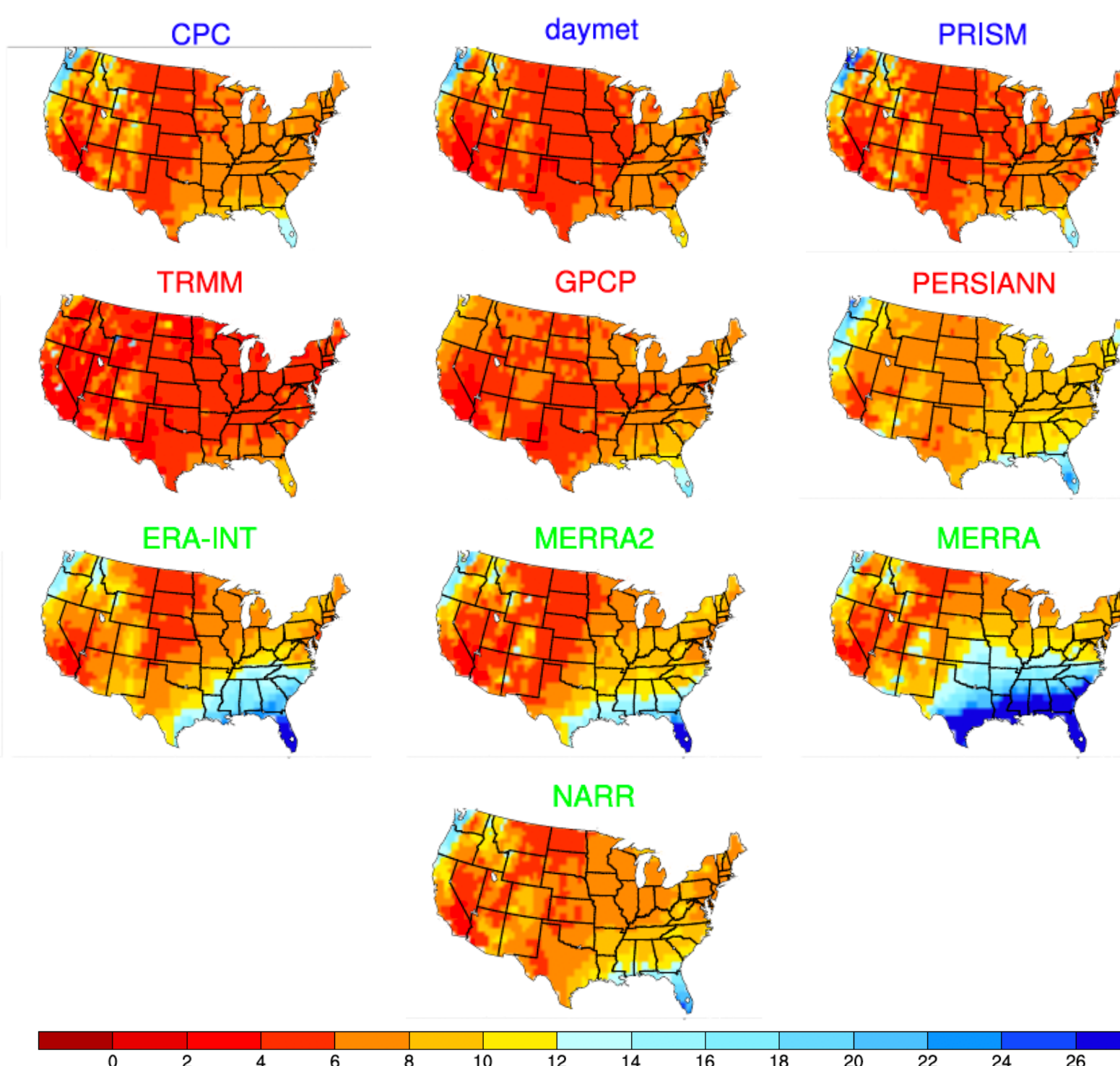
Methods

- Model/observation similarity from T-index from Tian et al. (2017, J. Hydromet):

$$T = \underbrace{[(1 + R)/2]}_{\text{Spatial pattern error}} \times \underbrace{[1 - \text{MSE}/(\text{Bias}^2 + \sigma_f^2 + \sigma_r^2)]}_{\text{Normalized amplitude error}}.$$

- Multi-Dimensional Scaling (MDS) dimension reduction tool that attempts to map high-D data to low-D space so that between object similarity can be readily visualized.
- MDS is fed T-index from 40 datasets for 6 precipitation indices

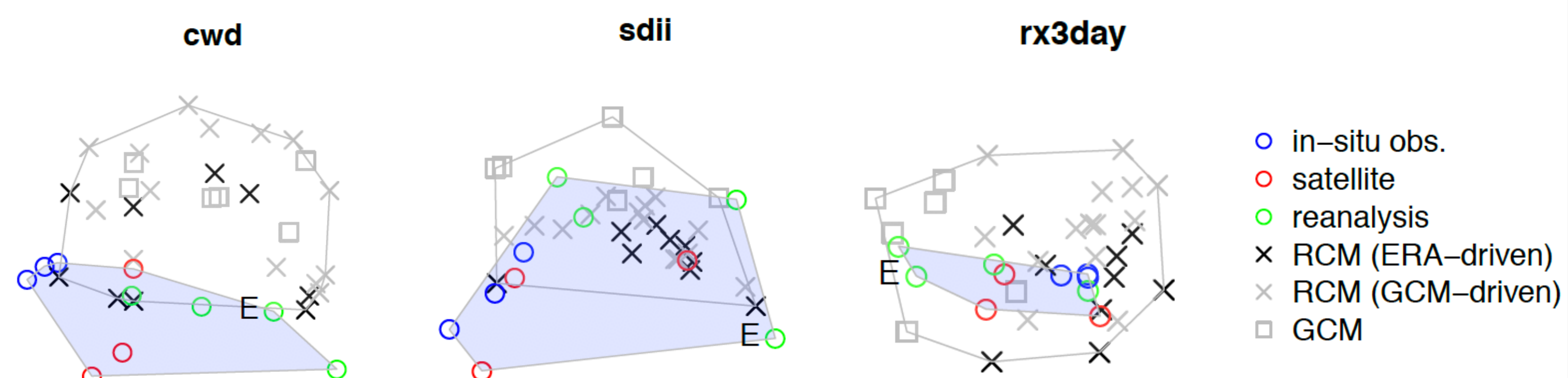
Results



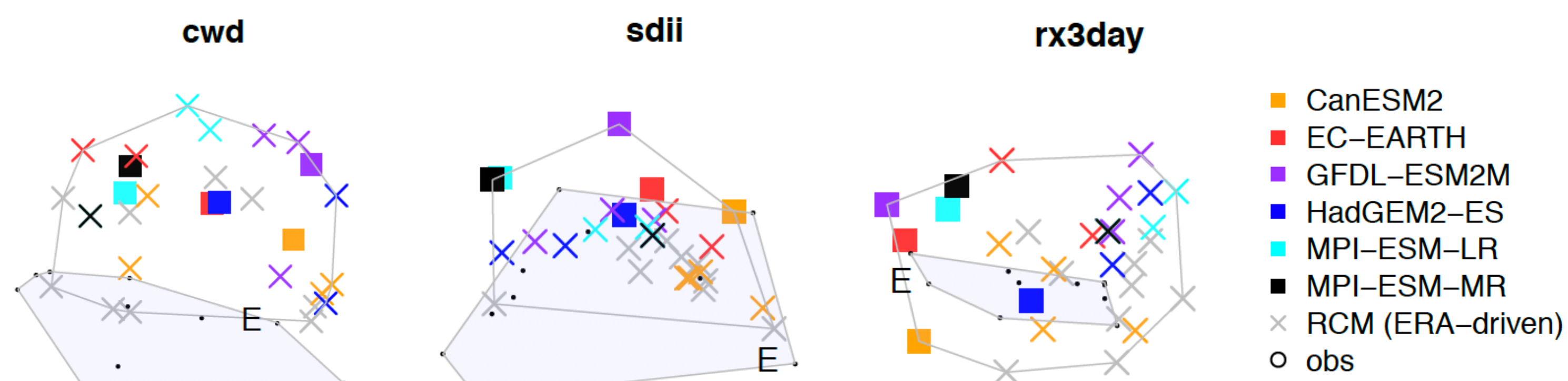
Example:

Consecutive Wet Day (CWD) climatology of observational products shows large spread. Use MDS (below) to compare this spread to model spread (30 simulations) for different precipitation indices

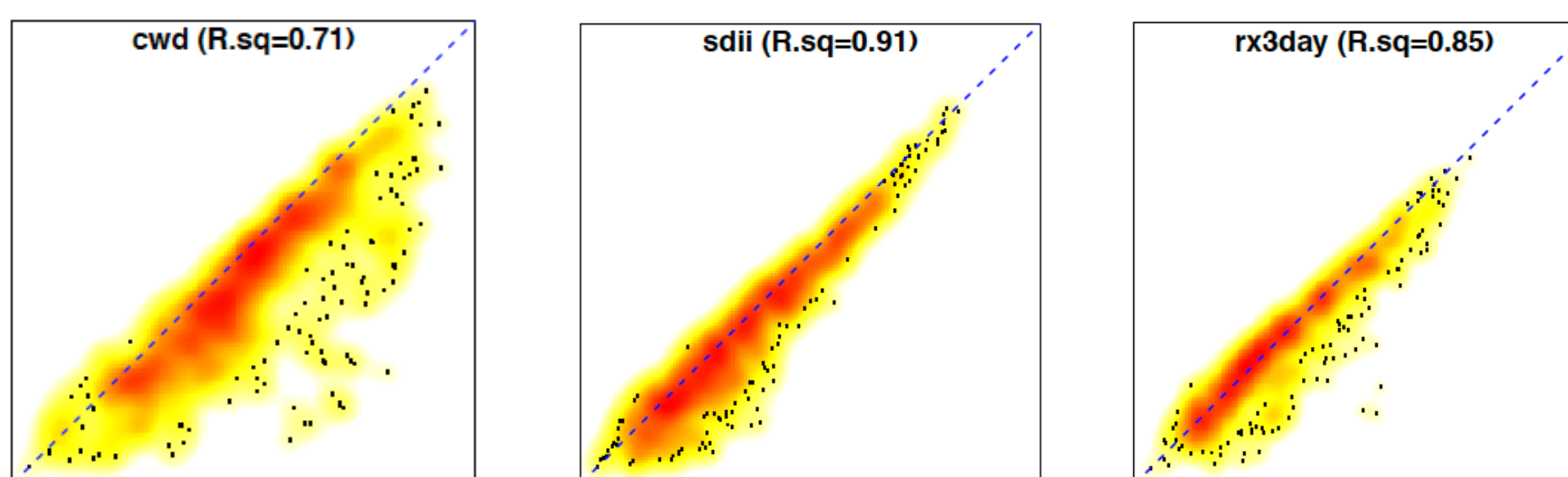
How do observations and models compare in MDS-space?



Do regional climate models (RCMs) add value?



How much information is lost in the dimension reduction?



Conclusions

- MDS is a useful tool to examine model differences relative to the spread in observations (other methods require a single reference observation)
- Degree of observational uncertainty depends on precipitation index
- There is no apparent added-value in downscaling for some precipitation indices
- Model uncertainty comes from both large scale (i.e. GCM choice) and small scale (i.e. RCM choice)

Characterizing CH₄ Emissions in Arctic and Boreal Regions via AVIRIS-NG Airborne Hyperspectral Imagery

Author: Clayton D. Elder (329G-Affiliate)

Co-Authors: C. E. Miller (329G), D. R. Thompson (382B), A. K. Thorpe (382B)

1. Motivation

- Arctic and Boreal regions are warming at 2x the global average, threatening widespread permafrost thaw, enhanced CH₄ and CO₂ emissions, and a positive feedback to further warming.
- Our ability to accurately observe, model, and forecast **northern GHG emissions (esp. CH₄)** are complicated by their **high spatial and temporal variability**, and the general inaccessibility of circumpolar regions.
- Space-or-ground-based strategies operate on scales too coarse or fine, respectively, to adequately characterize CH₄ sources. Airborne imaging spectroscopy bridges scale gaps and has identified point source CH₄ emissions related to industry and fossil fuels¹, geologic sources², landfills³, and agriculture⁴. We now apply this approach to understand high-latitude CH₄ emissions.

What environmental factors regulate CH₄ emissions, on small and large scales, in climate-sensitive Arctic and Boreal regions?

2. Objective

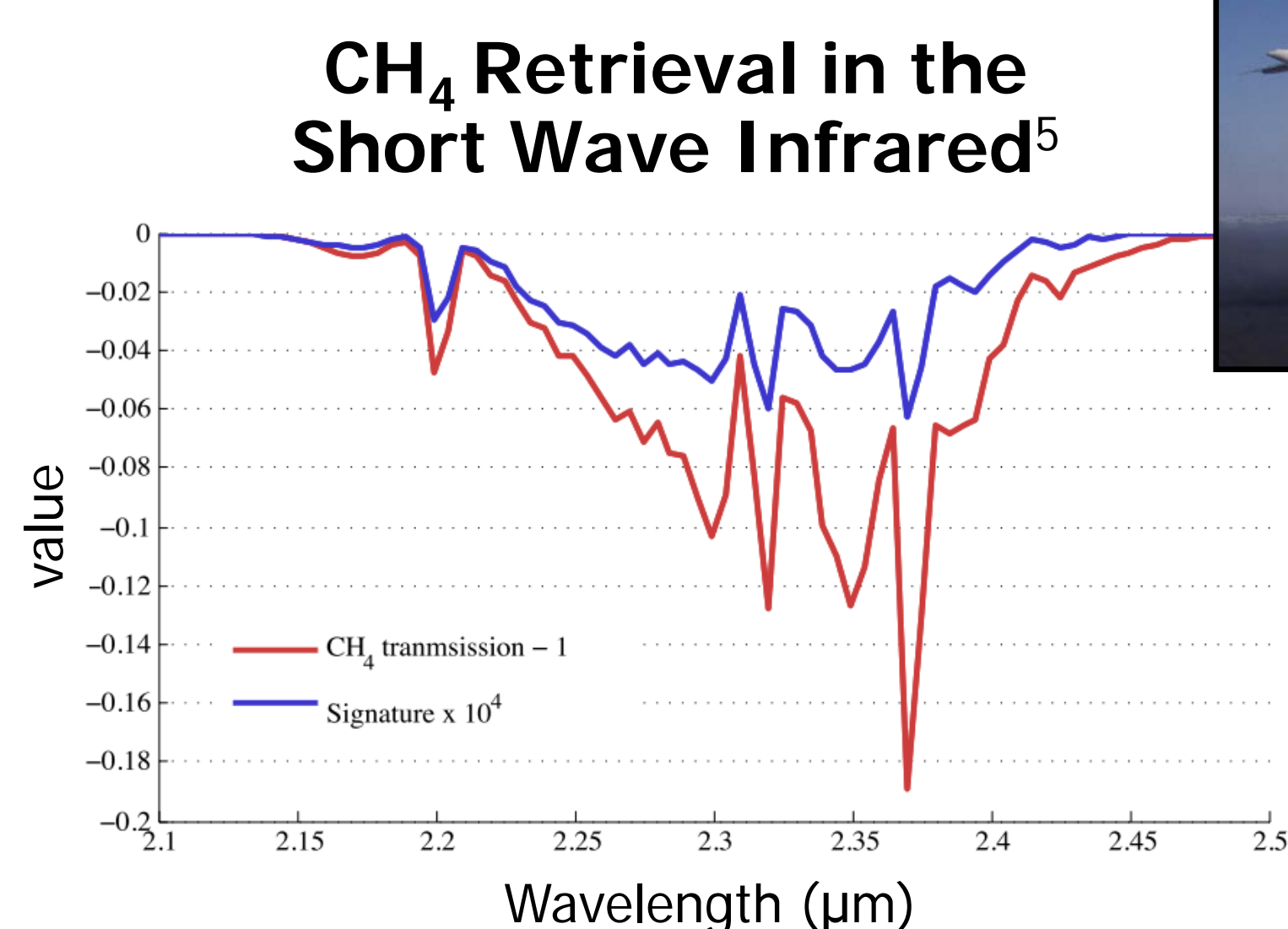
- Geospatially characterize remotely-sensed CH₄ enhancements in relation to key ecosystem variables such as water table position, vegetation, and climate.
- Develop a ground-truth strategy for evaluating observed CH₄ enhancements in terms of CH₄ flux.

3. Methodology

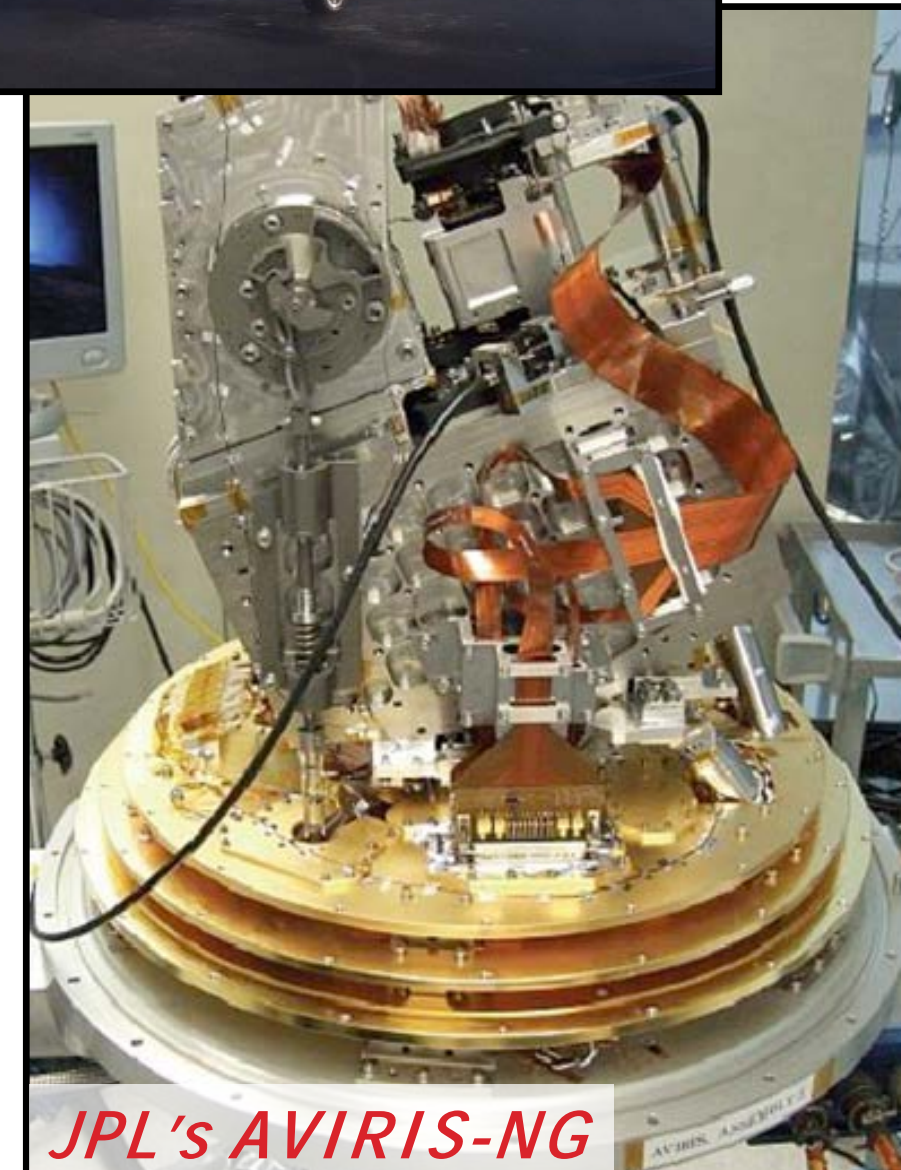


2017 Arctic Boreal Vulnerability Experiment (ABoVe) airborne campaign

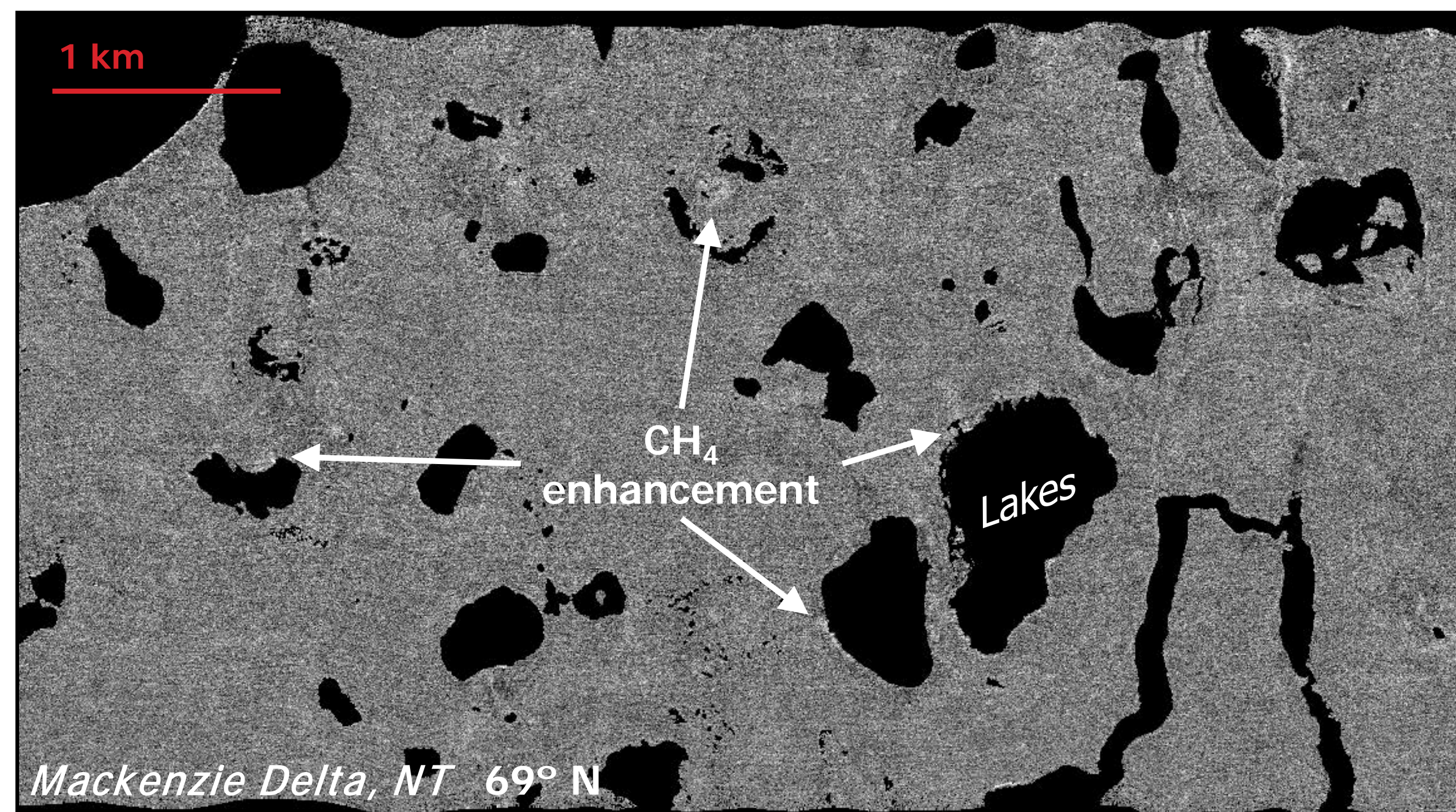
- Airborne Vis/IR Imaging Spectrometer – Next Gen.
- Roughly 40k km² imaged
 - Arctic and Boreal wetlands
 - Oil & gas production sites
 - Mapped Mackenzie Delta
- 5 x 5 m pixel resolution



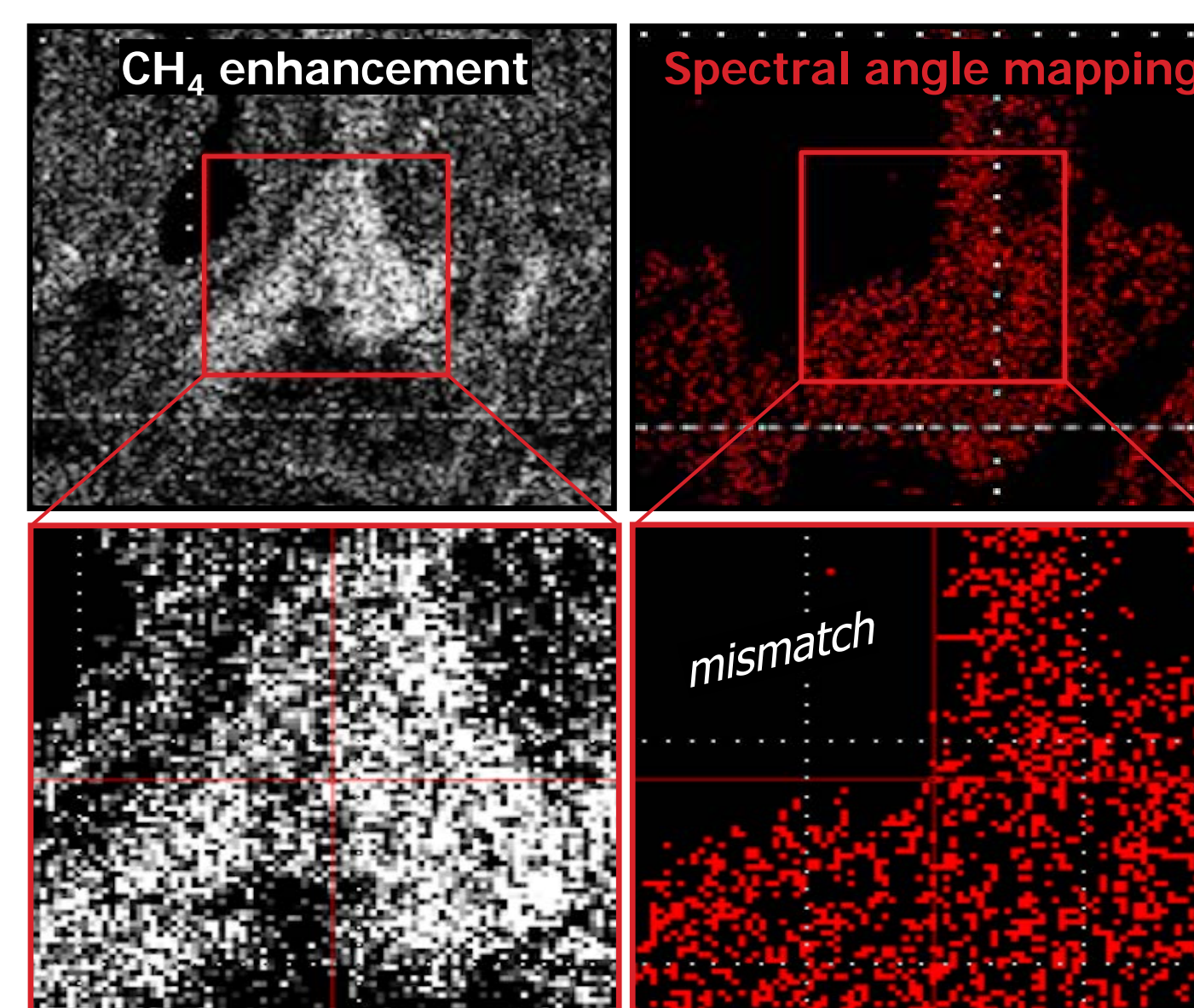
- CH₄ absorption of surface-radiated SWIR
- Column-wise Jacobian matched filter calculates perturbation from background radiance values.



4. Results



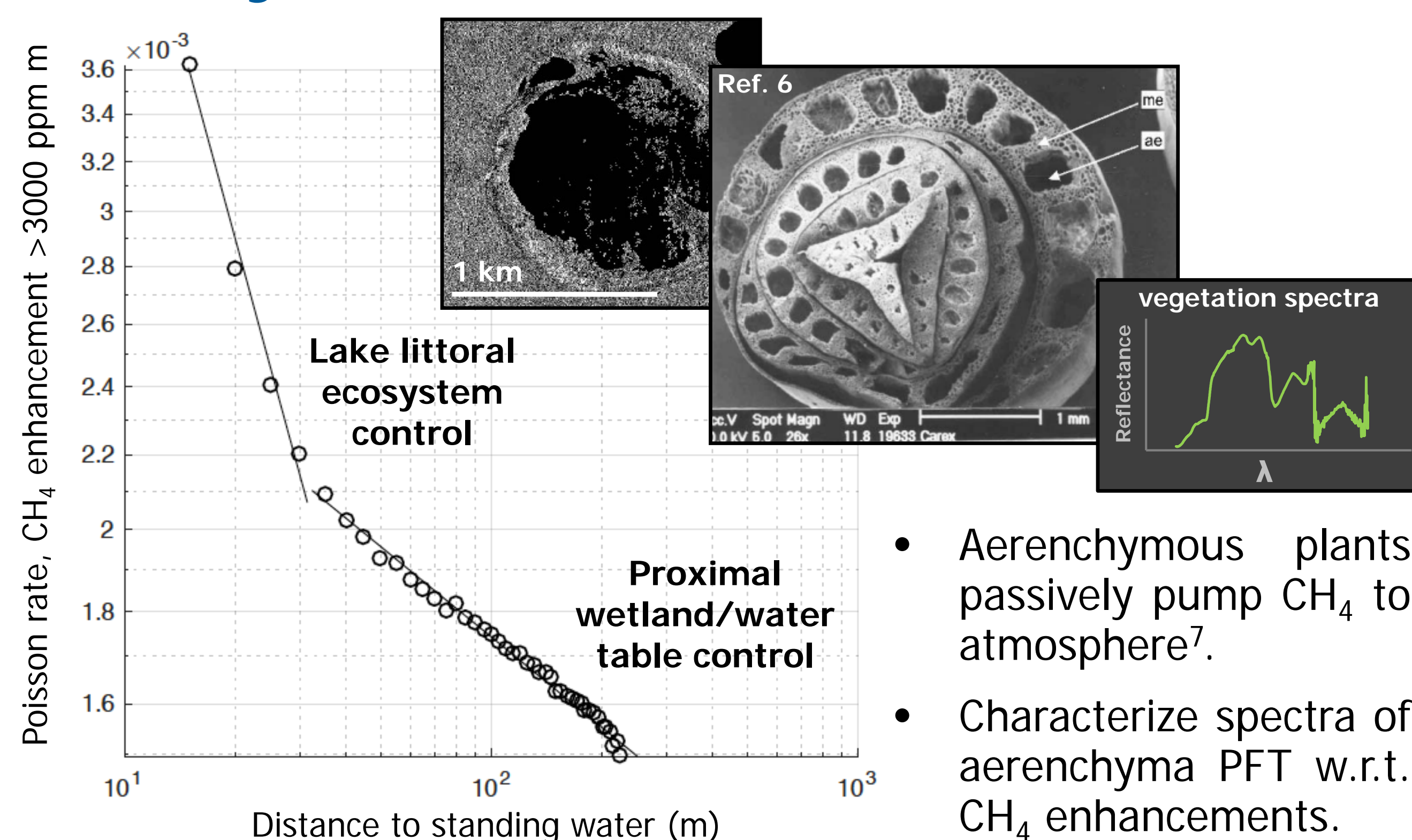
- Tens of thousands of distributed CH₄ enhancements across many Arctic and Boreal wetland ecosystems
- Enhancement distribution resembles characteristic "heavy-tail" pattern (isolated hotspots dominate flux)



Quality Control

- Spectral angle mapping to identify enhanced regions with similar reflectance spectra (land cover)
- CH₄ enhancements appear independent of surface reflectance properties (surface does not induce false positive).

5. Early Conclusions & Future Direction



- Aerenchymous plants passively pump CH₄ to atmosphere⁷.
- Characterize spectra of aerenchyma PFT w.r.t. CH₄ enhancements.
- Two power laws explain CH₄ enhancement rate w.r.t. distance to standing water. Explore correlation with emergent grasses.
- Design ground-based test of power laws (CH₄ flux vs. distance to standing water).

References and Acknowledgements

1. Frankenberg et al. 2016 *P. Natl. Acad. Sci.* 2. Thorpe et al. 2017 *Atmos. Meas. Tech.* 3. Krautwurst et al. 2017 *Atmos. Meas. Tech.* 4. Ayasse et al. 2018 (in revision) *Proc. Spie.* 5. Thompson et al. 2015 *Atmos. Meas. Tech.* 6. Kutzbach et al. 2004 *Biogeochem.* 7. von Fisher et al. 2010 *J. Geophys. Res. Biogeo.*

This research was funded by the NASA grant "Imaging Arctic CH₄ Plumes" awarded to C. E. Miller (329G). We would like to thank Winston Olson Duvall (382B) for processing the AVIRIS-NG datasets used in this research.

Simultaneous regional detection of land-use changes and elevated GHG levels

Armineh Barkhordarian^{1,2} (329J)

Hans von Storch³, Ali Behrangi^{2,4}, Jonathan H. Jiang² (329J), Paul C. Loikith⁵, Carlos R. Mechoso¹

¹University of California, Los Angeles. ²Jet Propulsion Laboratory, California Institute of Technology. ³Helmholtz-Zentrum Geesthacht, Germany. ⁴University of Arizona, Tucson. ⁵Portland State University, Portland

I. Introduction

This study aims at attributing the recently observed “drier dry season” over tropical South America to external drivers of climate change, both human induced [well mixed greenhouse gases (GHG), anthropogenic aerosols (AA) and land-use-change (LU)] and naturally occurring [solar irradiance and stratospheric aerosols due to volcanoes (NAT)]. A decline in dry season precipitation has a large impact on soil water storage and ecosystem health of the region. Thus, attributing the forced components of the observed “drier dry season” over tropical SA to external drivers of climate change is of great practical importance to societies.

Scientific question

Are we observing systematic trends of rainfall or are we solely witnessing the effects of natural internal variability of the climate system?

II. Methodology and Data

We have two fundamental objectives:

- 1) To detect externally forced changes in the observed record (Detection)
- 2) To attribute detected changes to natural or anthropogenic forcing (Attribution) [Barkhordarian et al., 2017; 2018]

Observation

GPCP and GPCP gridded observed datasets.

Model data

- 23 Global Climate Models (CMIP5)
- 1 regional Climate Model (CORDEX)
- Single forcing simulations of GHG, LU, NAT and AA
- Pre-industrial Control simulations (CMIP5)
- CCSM4 millennium simulation (850-1850)

III. Results

Regions where externally forced changes are detectable

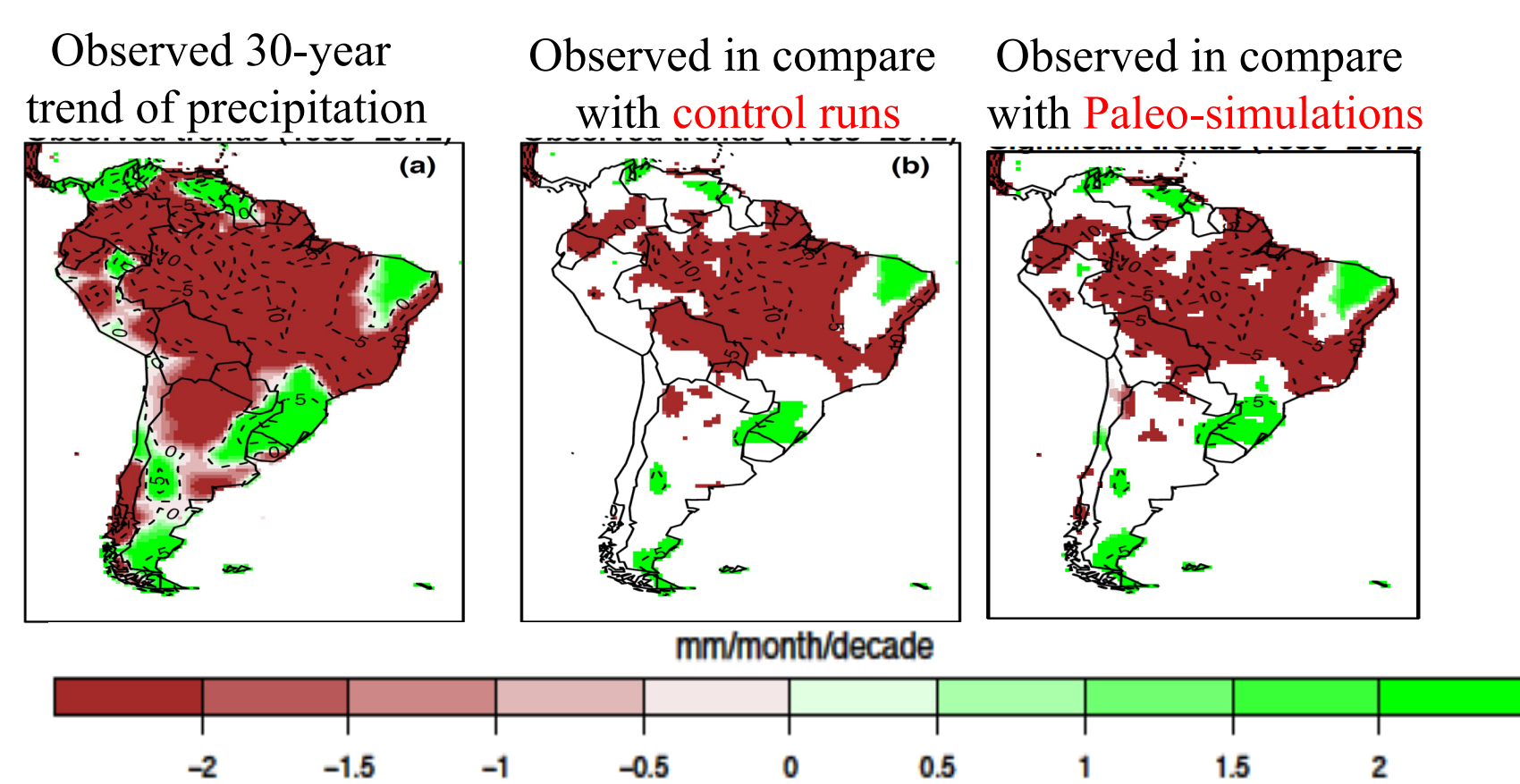


Figure 1: Regions where externally forced changes are detectable in the observed 30-year trends of precipitation in ASO (August-October) (with < 5% risk of error).

Bivariate signal attribution

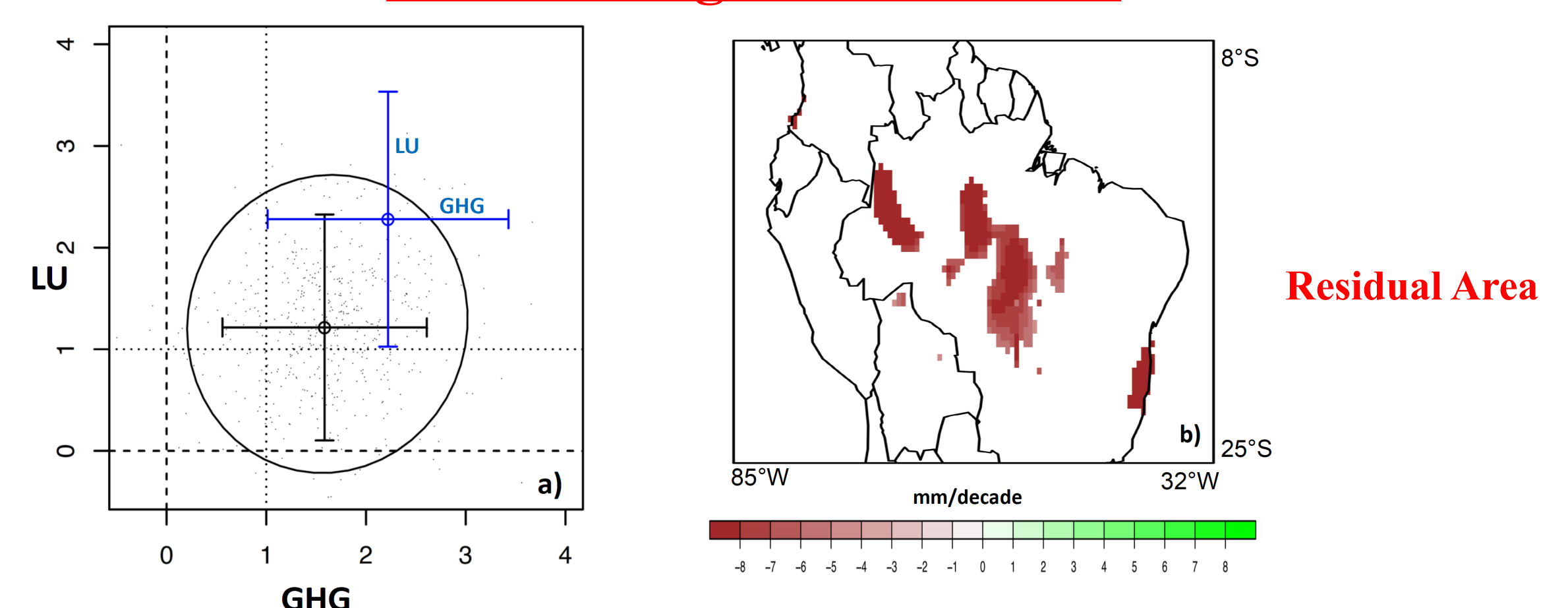


Figure 4: Left: The ellipse displays the joint 2-dimensional 90% uncertainty interval of scaling factors for the GHG and LU when observed data are regressed onto two signals simultaneously during 1983-2012. The black and blue whiskers indicate the bivariate and univariate 1-dimensional 95th %-tile uncertainty intervals for the two signals, respectively. Right: Regions where externally forced changes are still detectable after removing the effect of GHG and LU forcing (at 5% level).

Univariate Signal Detection

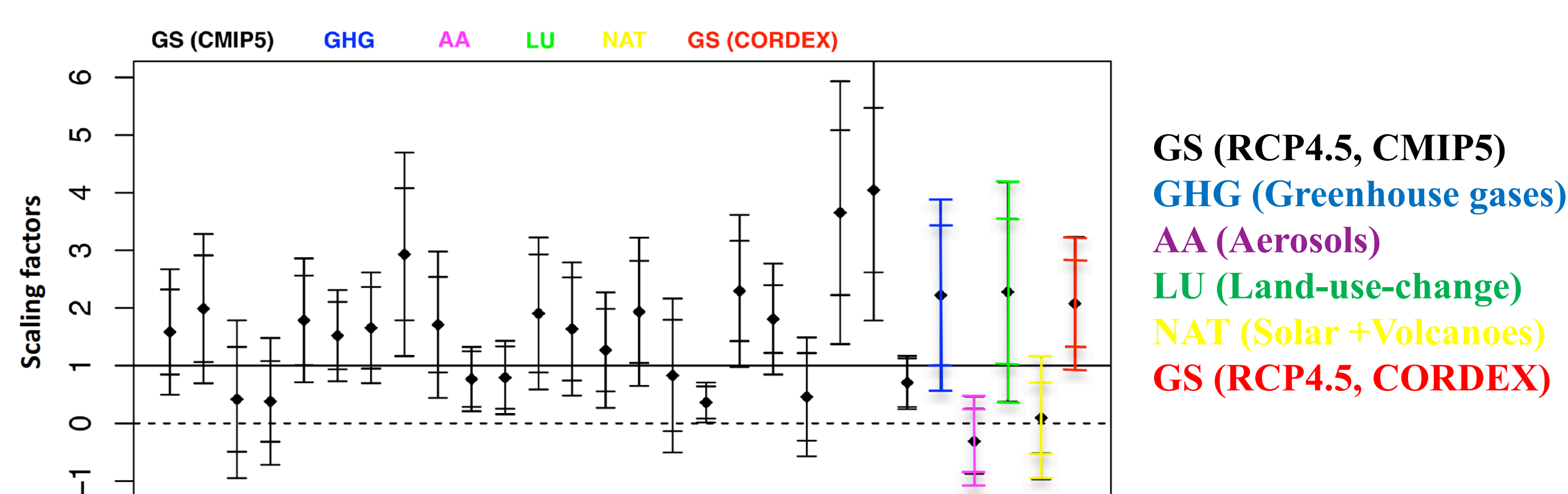


Figure 2: Scaling factors of observed precipitation changes against climate change signal patterns.

Detection of a signal can be claimed in those cases where the whiskers does not include the “0” line but includes “1”.

Detection of anthropogenic drivers

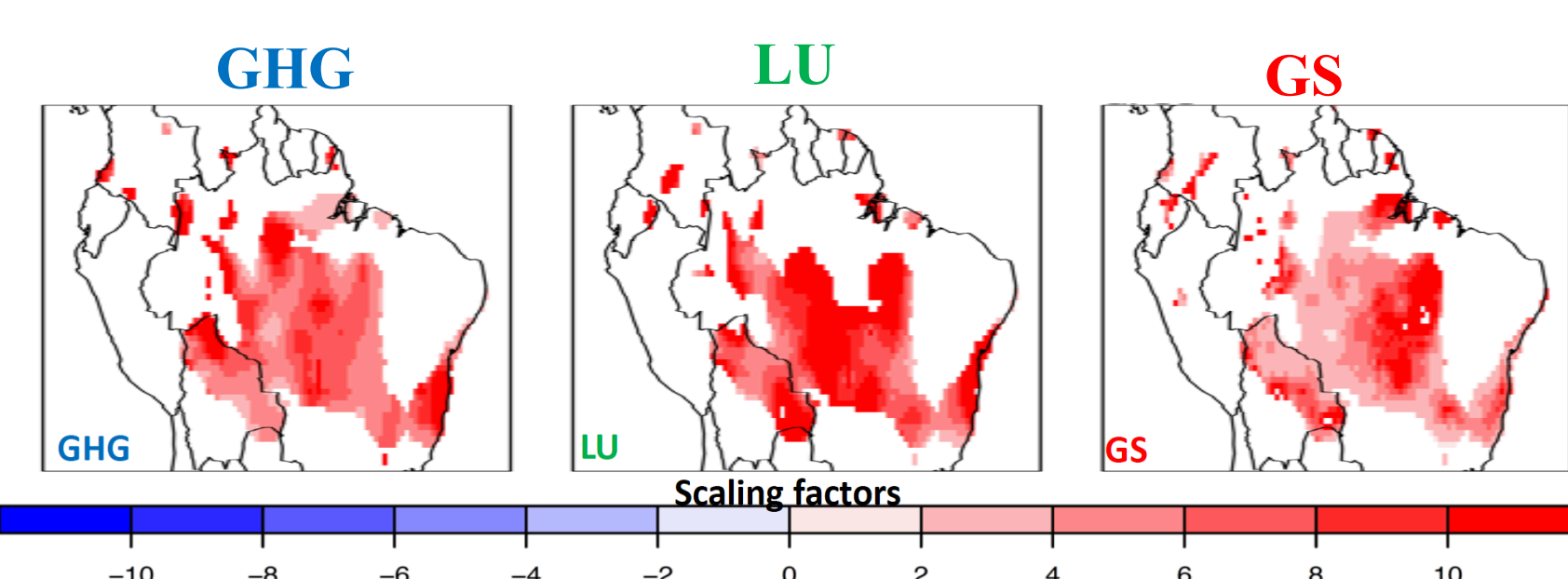


Figure 3: Regions where the effect of climate change signals are detectable in the observed precipitation record (at 5% level).

1-year moving scaling factors

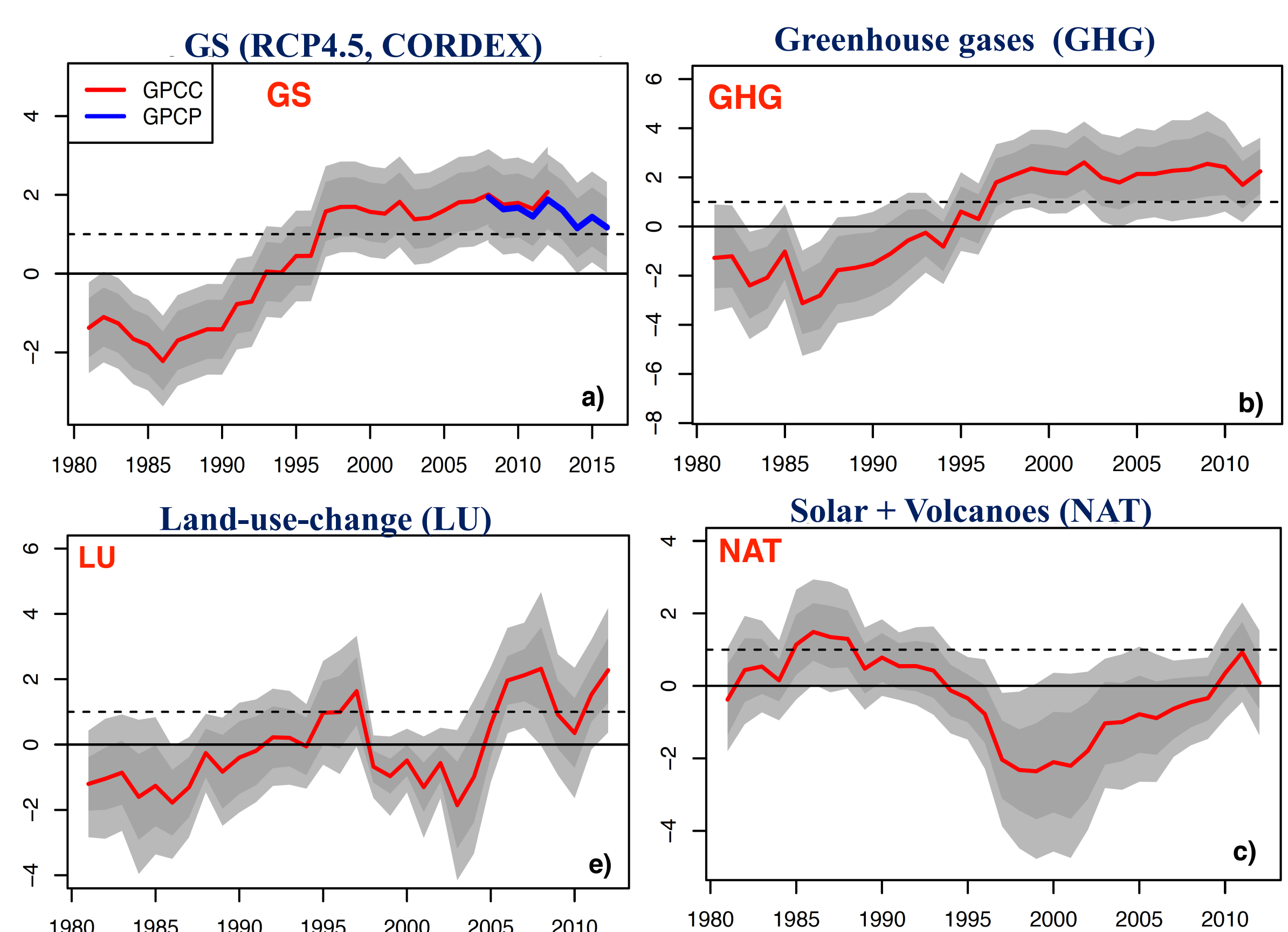


Figure 5: Scaling factors of observed 1-year moving 30-year trends of precipitation in ASO onto the GS, GHG and LU guess patterns. The horizontal axes show the end-year of moving 30-year trends. The grey shaded area indicates the 95th -tile range in a stationary climate based on 400 control run segments, for the raw and double the model variance. **Detection of a signal can be claimed in those cases where the gray shaded area excludes “0”.**

Conclusions

- The recently observed “drier dry seasons” over tropical South America is systematically and externally forced.
- The elevated GHG level and land-use-change are attributed as key causes for the observed drying over 1983-2012 period (<5% risk of error).
- The observed “drier dry season” is a feature which will continue and intensify in the course of unfolding anthropogenic climate change.

References:

Barkhordarian A, von Storch H, Zorita E, Loikith P.C. and Mechoso C.R. (2017) Observed warming over northern South America has an anthropogenic origin. *Climate Dynamics*. <https://doi.org/10.1007/s00382-017-3988-z>.

Barkhordarian et al., (2018) Simultaneous regional detection of land-use changes and elevated GHG levels: the case of spring precipitation in tropical South America. *Geophys. Res. Lett.* doi: 10.1029/2018GL078041

Measuring Earth's Energy Imbalance from Space

Authors: Maria Z. Hakuba (329J)

G.L. Stephens (3292), B. Christophe, A.E. Nash (3120), B. Foulon,
S.V. Bettadpur, B.D. Tapley, F.H. Webb (8300)

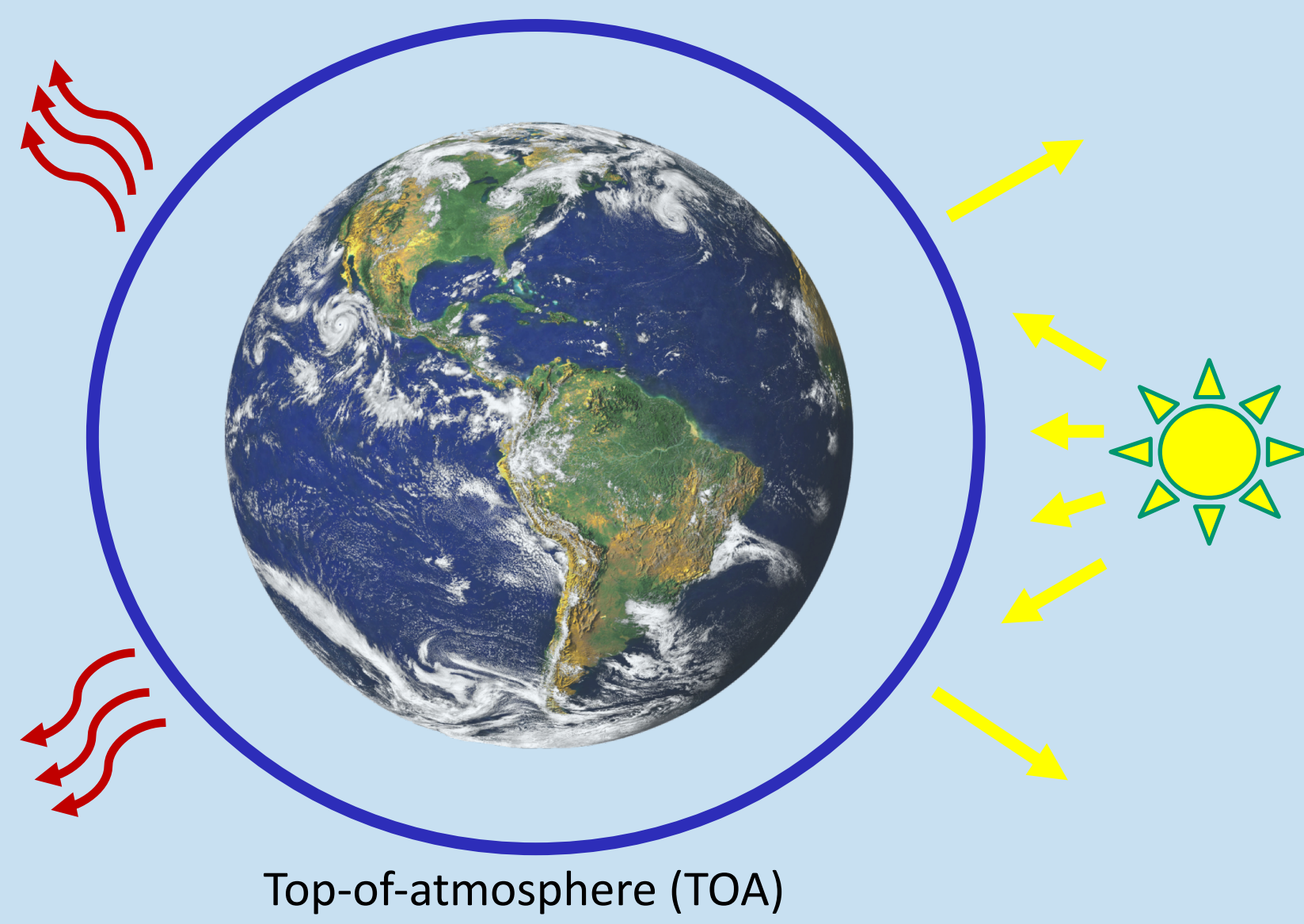
Global mean energy imbalance

Earth's energy imbalance (EEI) = Net radiative flux = Solar incoming – solar reflected – Earth emitted radiation =

$0.7 \pm 0.1 \text{ Wm}^{-2}$
(Johnson et al. 2016;
CERES EBAF)

→ direct estimate of global warming

93% of this excess heat is stored in global oceans



How EEI is measured today



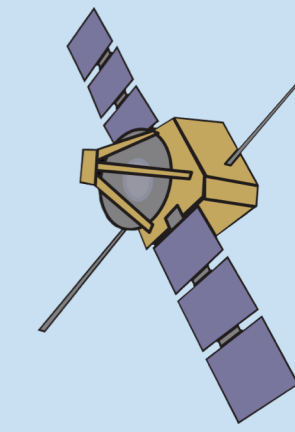
Ocean temperature: Argo in-situ measurement system profiles ocean column “globally”. Used to calculate change in ocean heat content (OHC).

Caveats: Misses heat in deep ocean, marginal seas, polar oceans



Steric sea level change: Provides OHC due to thermal expansion, From residual calculation of total sea level (altimetry) & ocean mass change (GRACE).

Caveats: Combines two data products with various sources of error

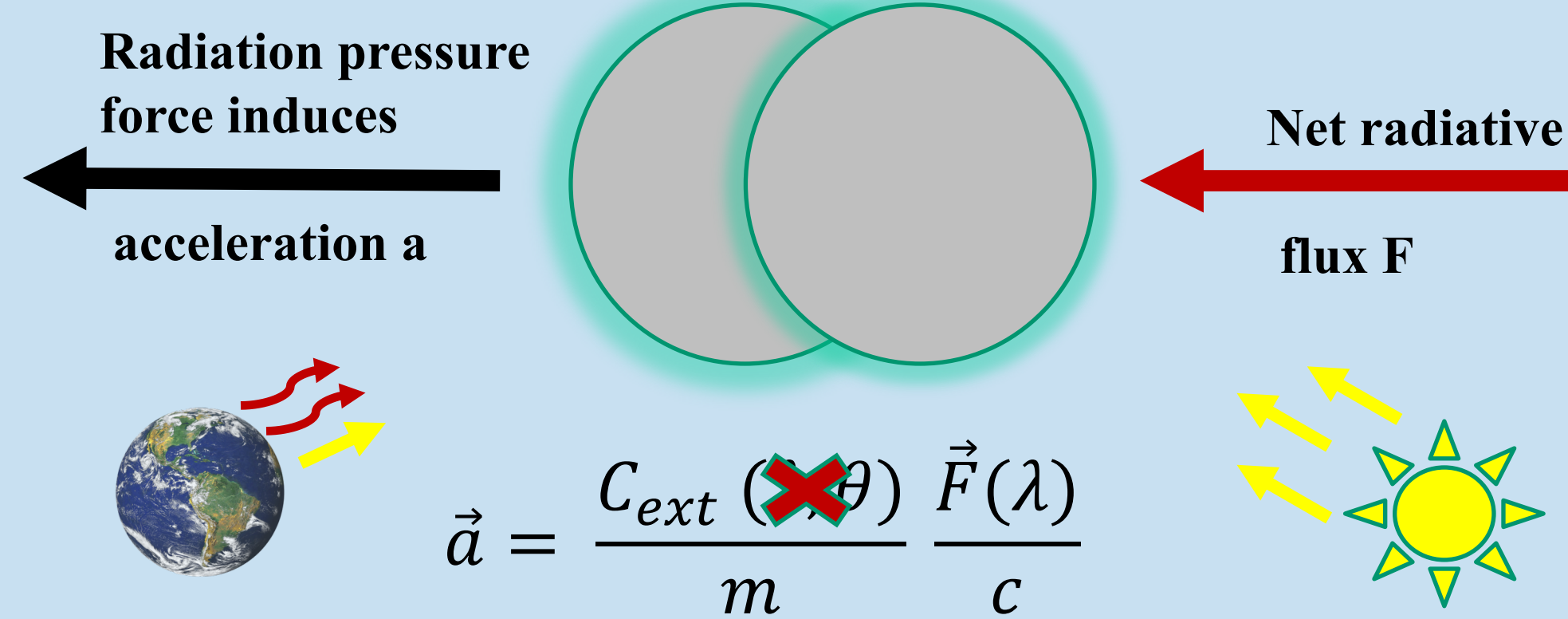


TOA radiometry: EEI=radiative component residual from CERES
Caveats: component residual has large calibration error: EEI= +4 Wm^{-2}

How can we measure EEI directly from space with an accuracy of at least $\pm 0.3 \text{ Wm}^{-2}$ to estimate global annual mean EEI and year-to-year changes?

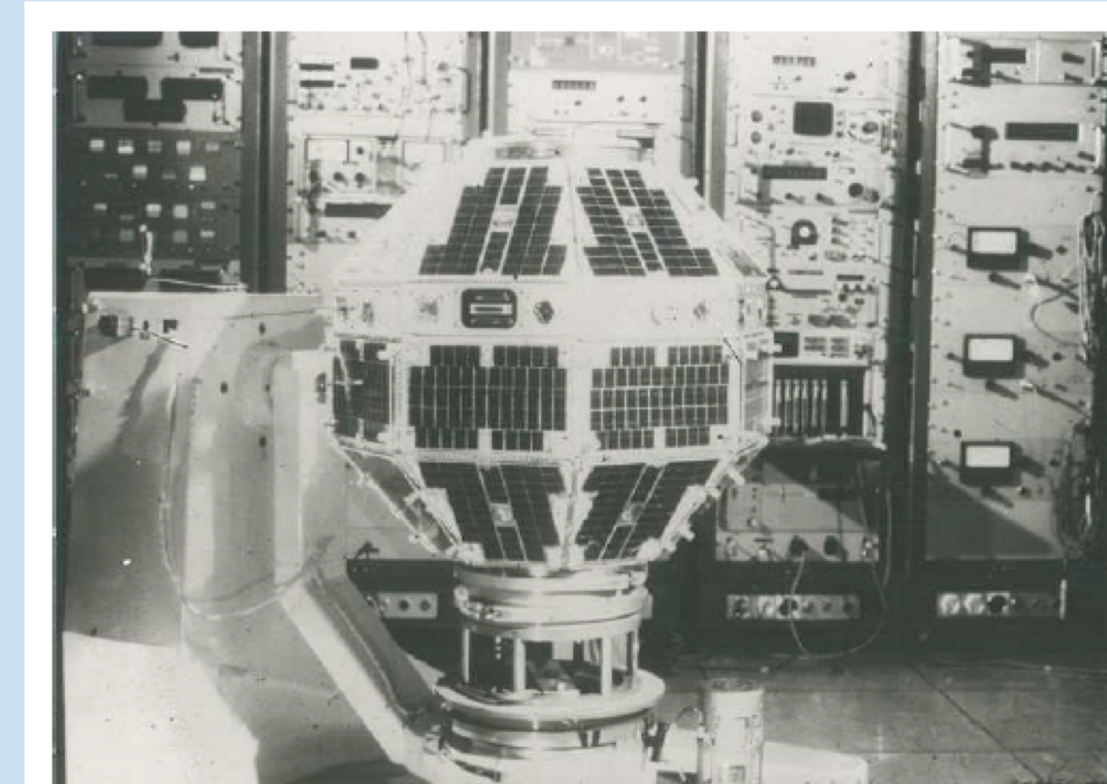
Derive EEI from radiation pressure force acting on spherical space craft

$$\vec{P} = m\vec{a} = \frac{1}{c} C_{ext} (\lambda \times \theta) \vec{F}(\lambda)$$



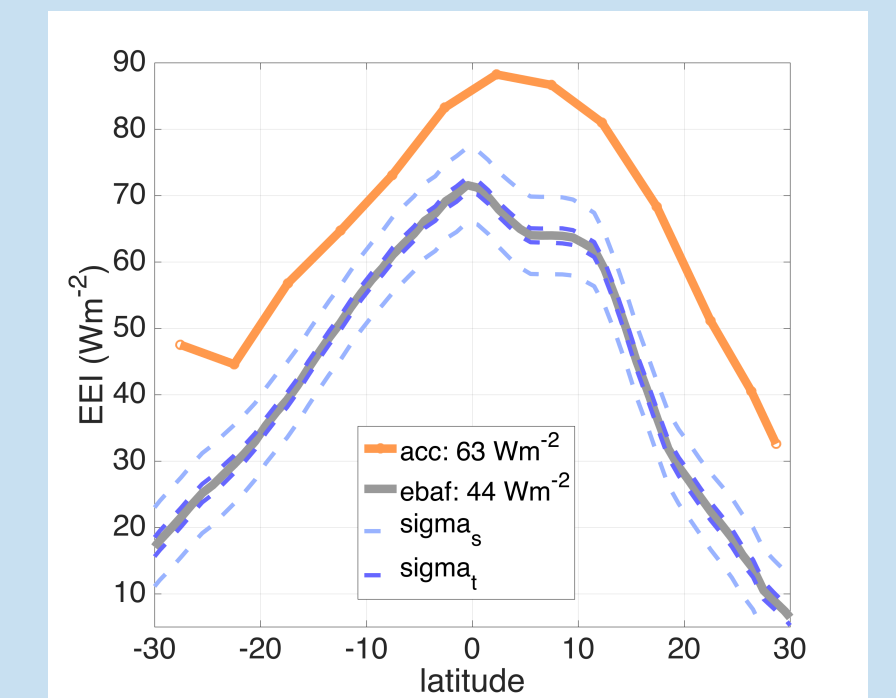
$$\vec{a} = \frac{C_{ext} (\lambda \times \theta) \vec{F}(\lambda)}{m c}$$

Accelerometer CACTUS demonstrates feasibility in 1975



CASTOR D5B Satellite CNES, 1975

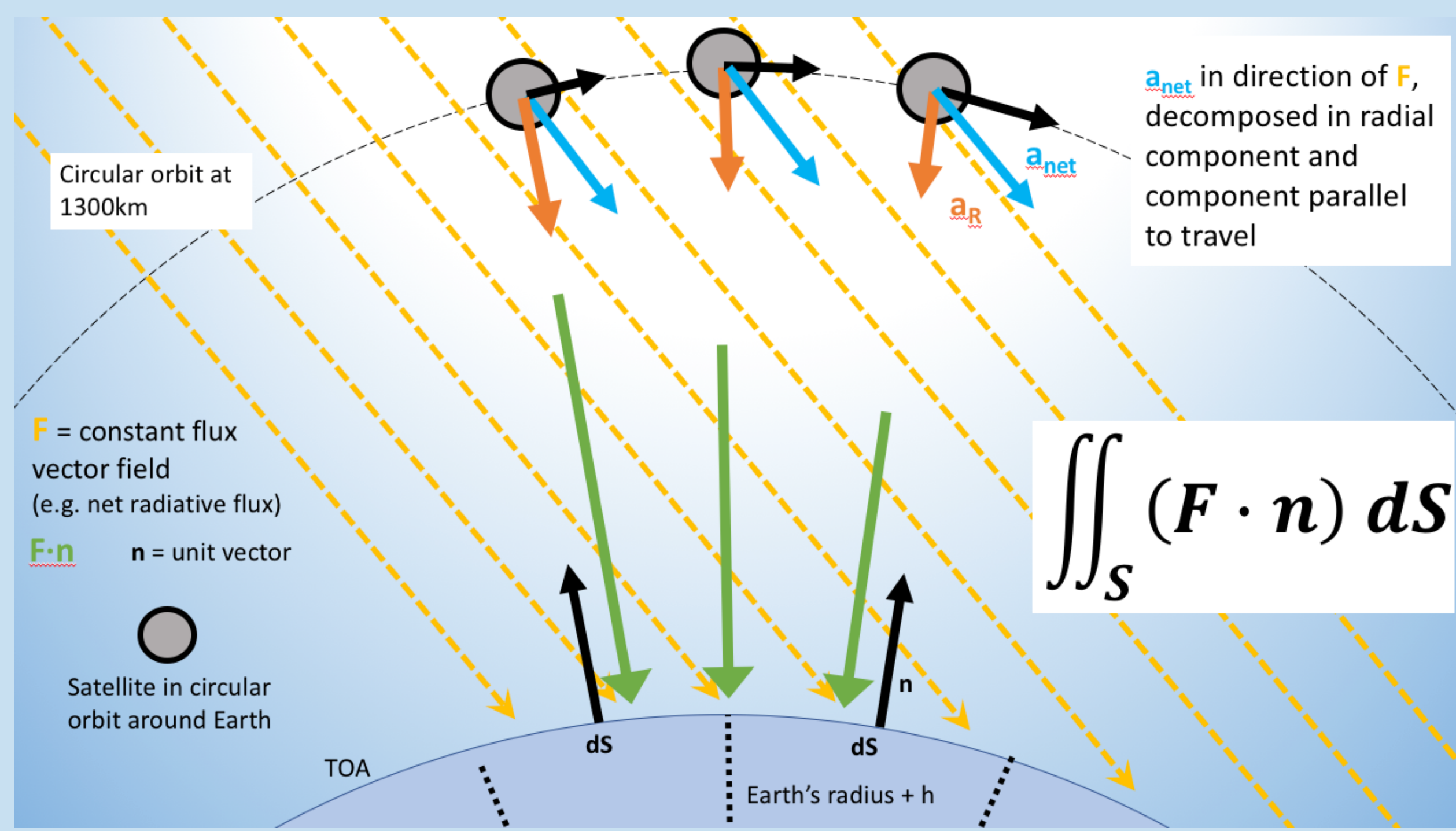
radius: 0.8 m, mass: 76 kg



Zonal averages of TOA net radiation flux (Wm^{-2}) derived from CACTUS accelerations (1975-1976, orange) and CERES EBAF (2000-2017, gray) between $30^{\circ}\text{S} - 30^{\circ}\text{N}$. Bright blue dashed lines represent the spatial $\pm 1\sigma_s$ of monthly $1^{\circ} \times 1^{\circ}$ anomalies per latitude, while the dark blue lines represent the temporal $\pm 1\sigma_t$ of zonally averaged monthly anomalies.

- Zonal and seasonal variability of EEI
- Longwave cloud effects and land-sea contrasts
- Incoming solar radiation

From acceleration to surface flux through TOA



Challenges

- Spherical satellite allows for EEI measurement via radial acceleration & eliminates aerodynamic drag effect: **custom design** required
- Optimization of thermal control & **thermo-optical properties**
- Model all **confounding effects** & accelerations with varying time & space resolutions, illumination angles, weather conditions, space craft characteristics
- Spatial and temporal **sampling** concerns: Aliasing and diurnal cycle coverage; multiple satellites in polar and non-polar orbits
- Instrument accuracy very high (0.01 Wm^{-2} at 10^{-3} Hz spin), but other uncertainties will add, goal is 0.3 Wm^{-2} or better .

Reference: Hakuba, M.Z., G.L. Stephens, B. Christophe, A.E. Nash, B. Foulon, S.V. Bettadpur, B.D. Tapley, F.H. Webb (2018), Earth's Energy Imbalance measured from space, accepted.

Essentials for realistic simulations of subtropical marine stratocumulus clouds

Author: Mark Smalley (329J)
Matthew Lebsock (329J), Kay Sušelj (398K), Joao Teixeira (3292)

I. Introduction

The Problem

➤ The representation of shallow maritime clouds in global circulation models constitutes a leading source of uncertainty in projections of Earth's future climate.

➤ What model physics are necessary to capture the relationship between low cloud cover and weather regime?

Our Solution for the JPL EDMF

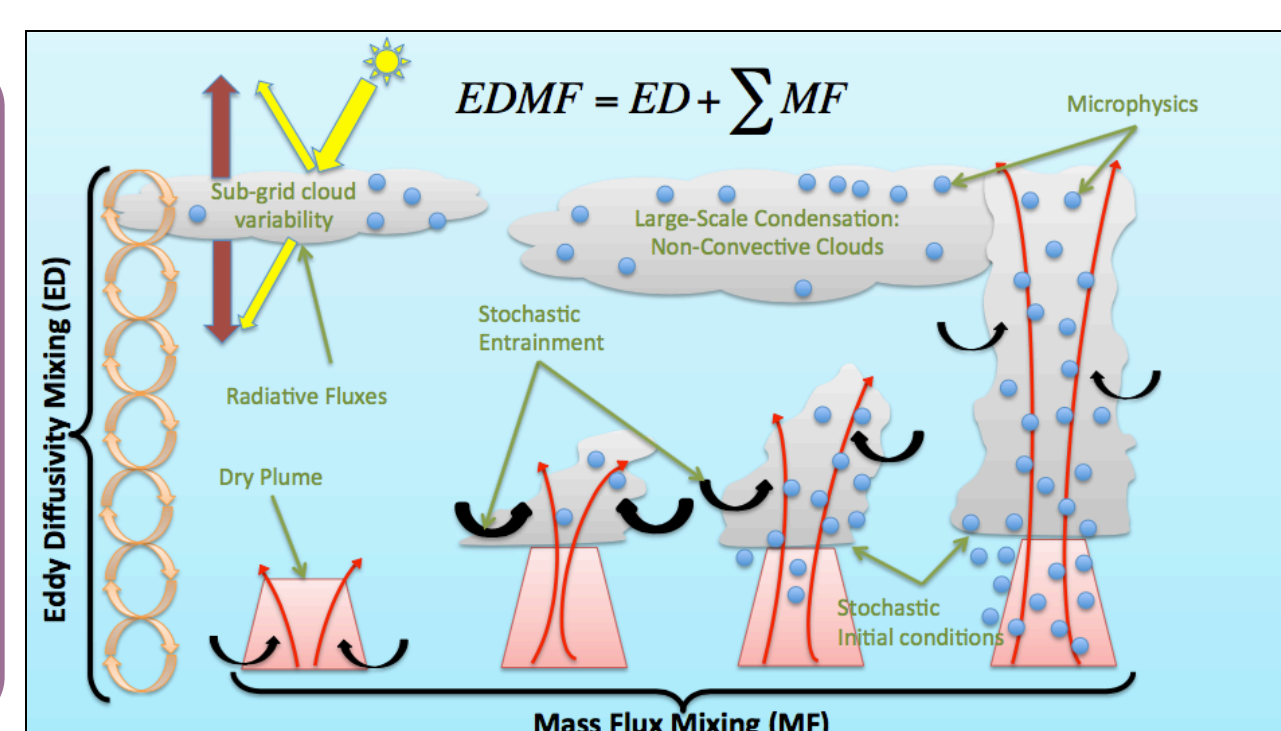
➤ We tune internal variables of the JPL Eddy-Diffusivity/Mass-Flux (EDMF), a unified turbulence and convection parameterization, in order to accurately simulate the relationship between low clouds and lower tropospheric stability.

➤ Global observations of cloud properties provided by NASA satellites and instruments (CloudSat/CALIPSO) are used as a benchmark for model simulations of low clouds.

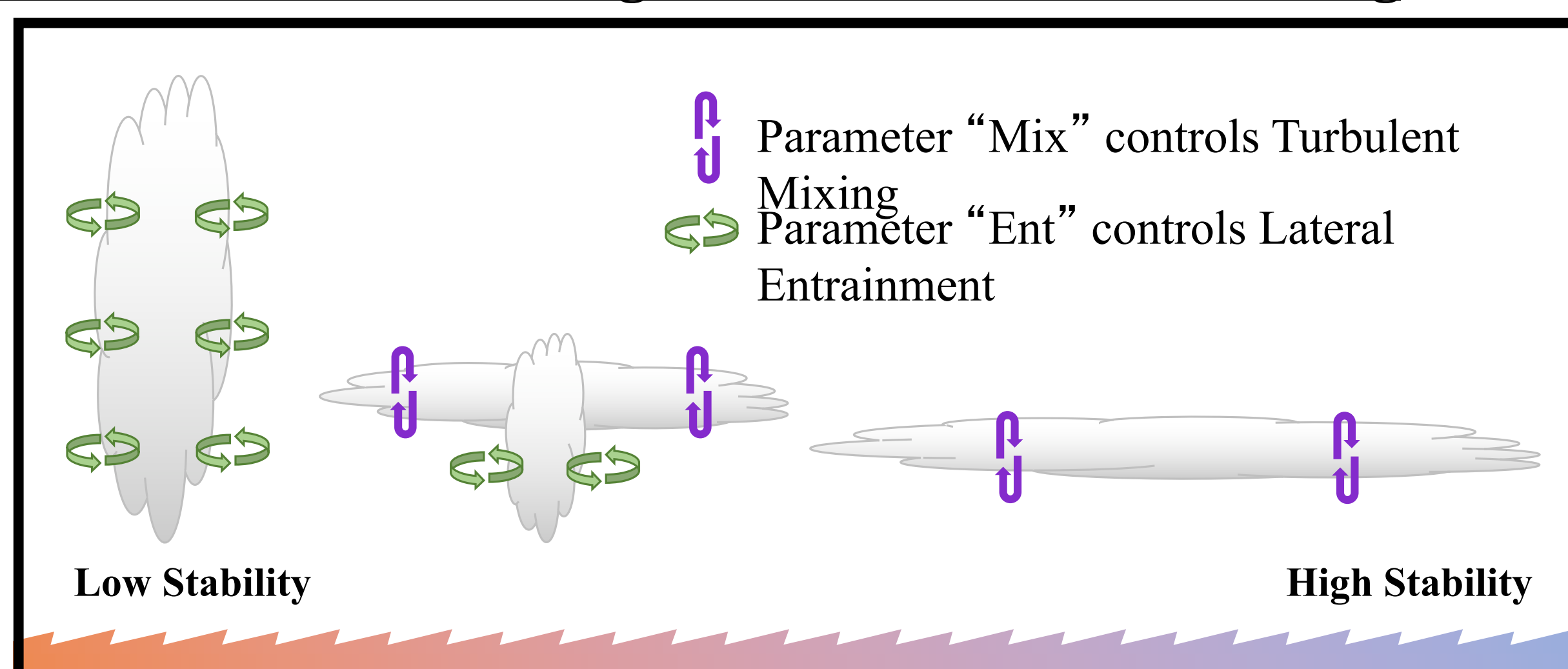
II. JPL Eddy-Diffusivity/Mass-Flux Parameterization

➤ JPL EDMF parameterizes sub-grid scale atmospheric physics (Sušelj and Teixeira 2018) within a large-scale model.

➤ A single-moment microphysics package is coupled to updraft dynamics, with prognostic total H_2O and θ_L .



III. Parameters Controlling Vertical and Lateral Mixing



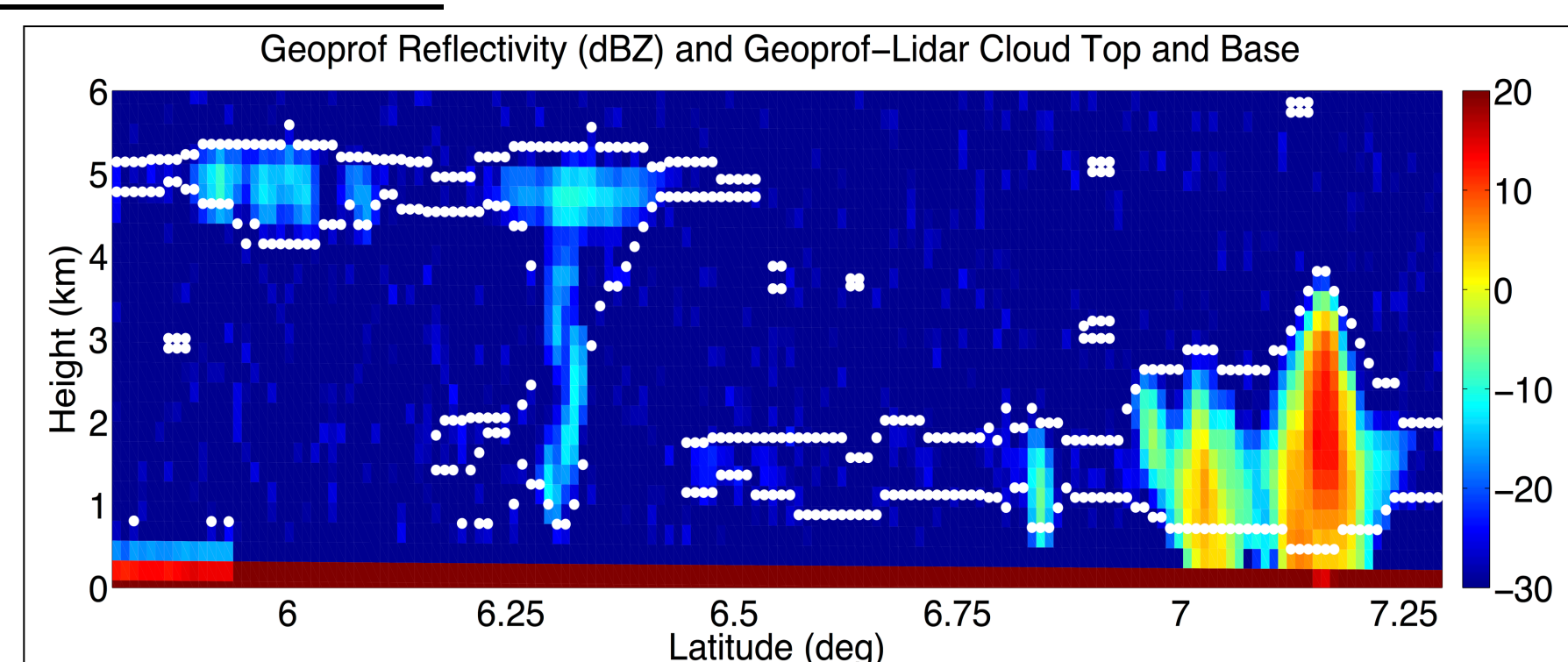
➤ EDMF parameter Ent controls lateral entrainment in buoyant updrafts and is most important in unstable conditions.

➤ EDMF parameter Mix controls small-scale turbulent mixing in the non-convective portion of the column and is most important in stable conditions.

We desire realistic simulations across all stability regimes, including when both lateral entrainment and turbulent mixing are at work!

IV. JPL Observations for Validation

➤ CALIPSO/CloudSat vertically-resolved cloud fraction



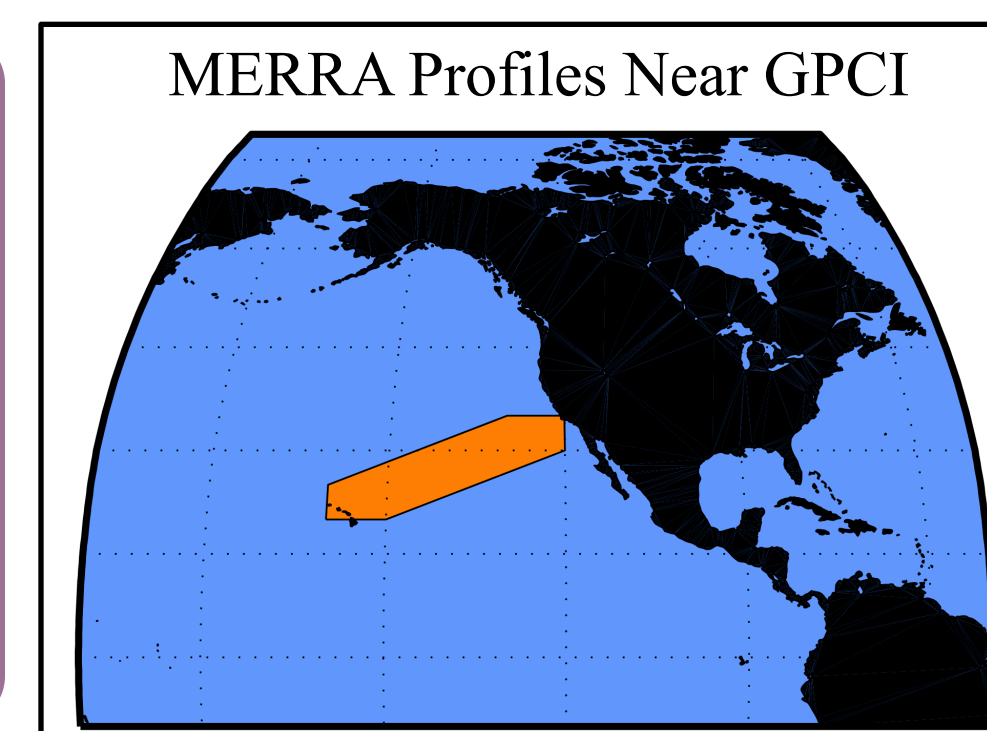
V. Experiment Design

➤ Initial conditions are provided by the NASA MERRA2 global reanalysis along the GPCI Polygon.

➤ All profiles have downward motion at 500 mbar.

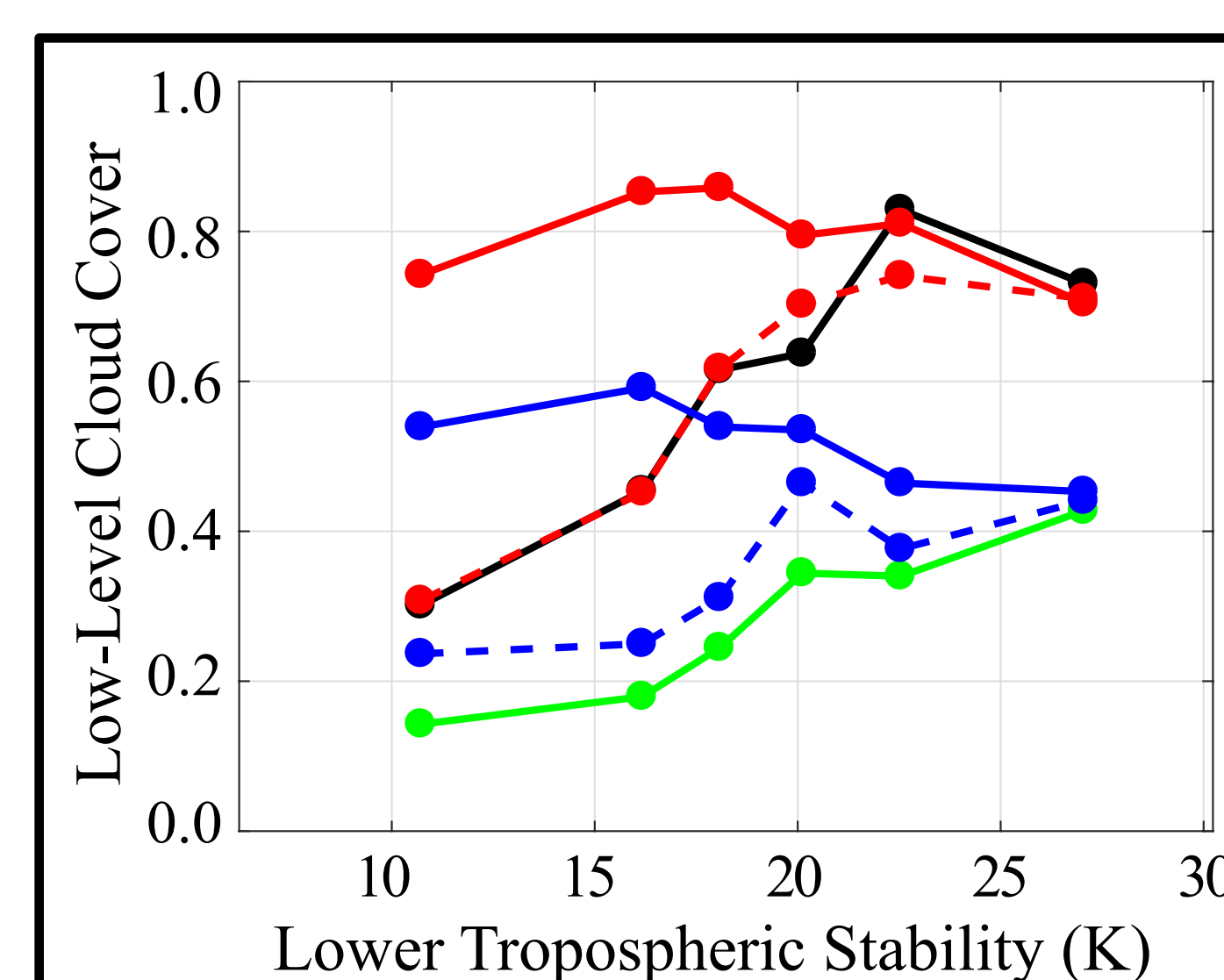
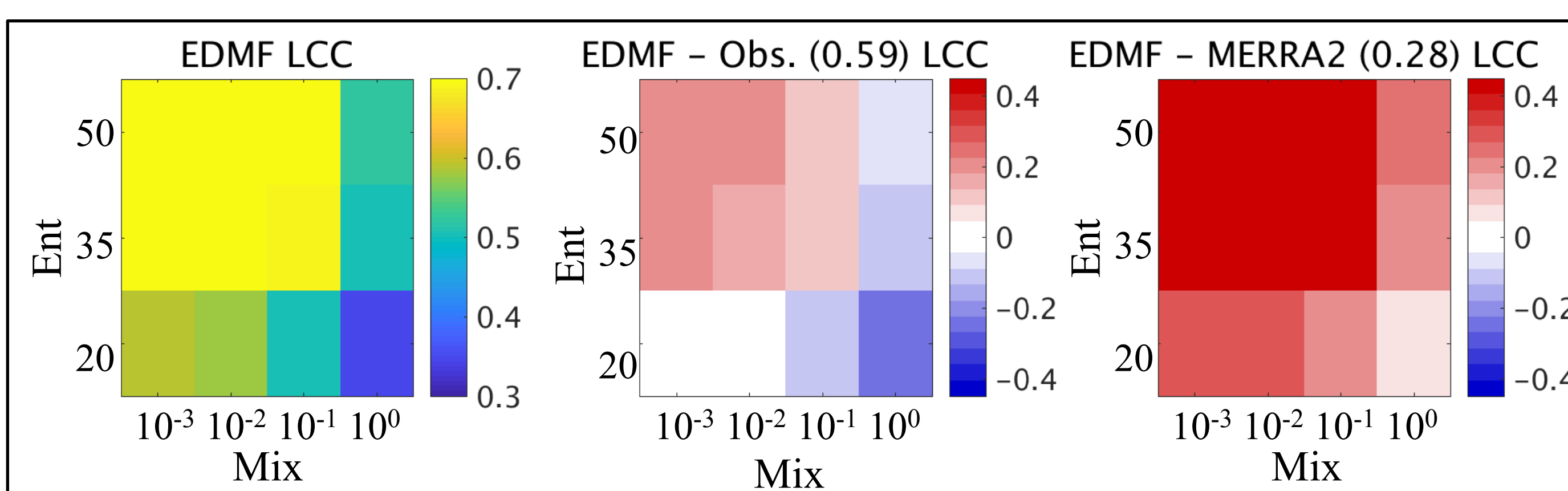
➤ 2000 individual EDMF profiles are run for 3 model hours within a single column model.

➤ Assessment is performed at the end of the simulation.

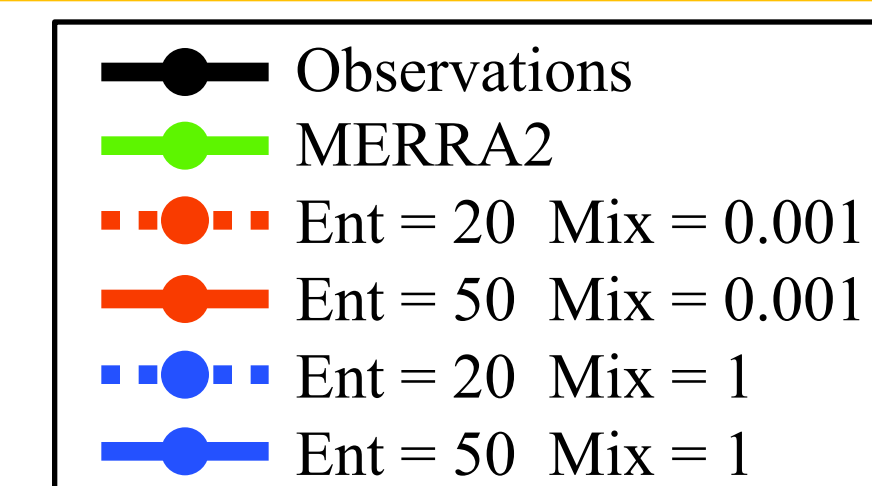


VI. Simulated Spectrum of Cloudiness

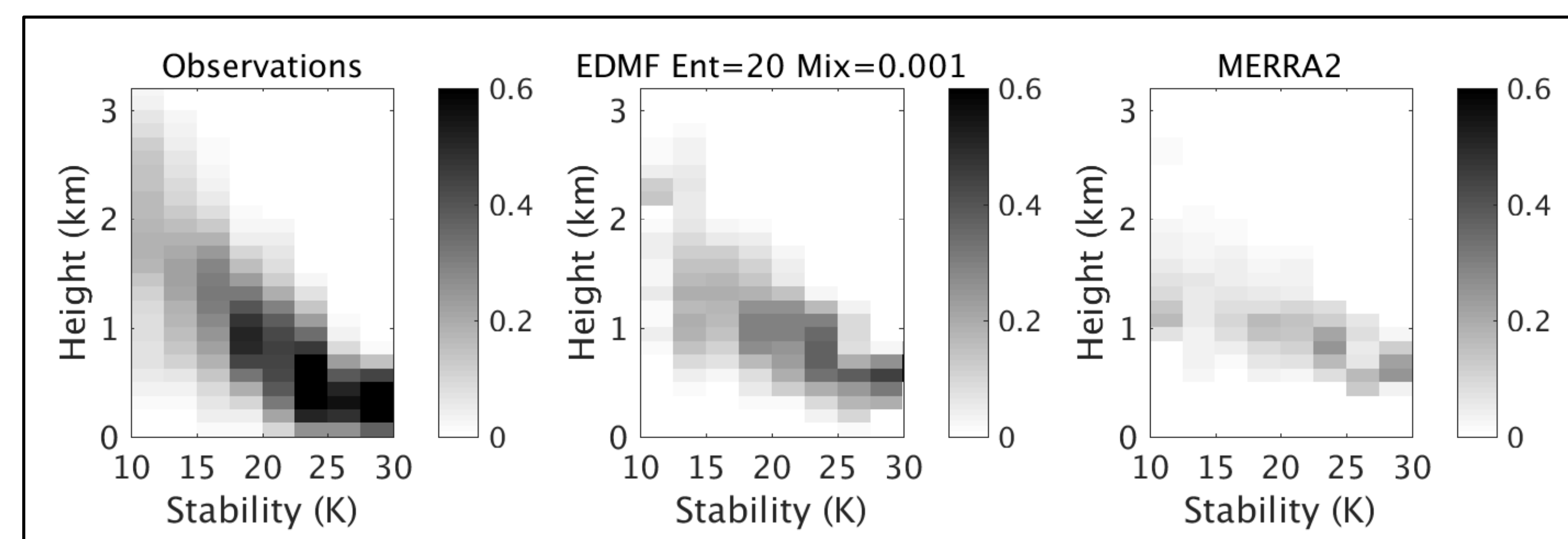
➤ When we run the same 2000 simulations for each candidate value of Ent and Mix, we find agreement in mean Low Cloud Cover (LCC) across a range of parameter space.



Inspection of low cloud cover as a function of stability regime reveals a clear winner with low entrainment and low turbulent mixing!



Simulated Cloud Fraction from JPL EDMF shows improvement over MERRA2.



VII. Conclusions

✓ Accurate parameterization of both entrainment and turbulent mixing are required for reliable simulations of low cloud cover, a key element in understanding climate change.

✓ Simple comparisons of average low cloud cover could lead investigators to implement the wrong combination of parameters!

✓ JPL EDMF shows improvement over MERRA2, which produces too few clouds.

References

Sušelj, K., J. Teixeira, 2018. A unified eddy-diffusivity/mass-flux approach for modeling atmospheric convection. In Review.

This research is funded by NASA CloudSat/CALIPSO science team funding to JPL under RTOP/WBS (105357/ 967701.02.01.02.08)

Warm Season Satellite Precipitation Biases for Different Cloud Types Over Western North Pacific

Nobuyuki Utsumi (334H)

H. Kim (329F), F. J. Turk (334H) and Z. S. Haddad (334H)

Background

- Satellite-based precipitation products are used in various fields.
- Biases for the products have been reported. (Associated with land surface type / water vapor / storm organization level)

Research Question:

Any systematic biases associated with cloud type?

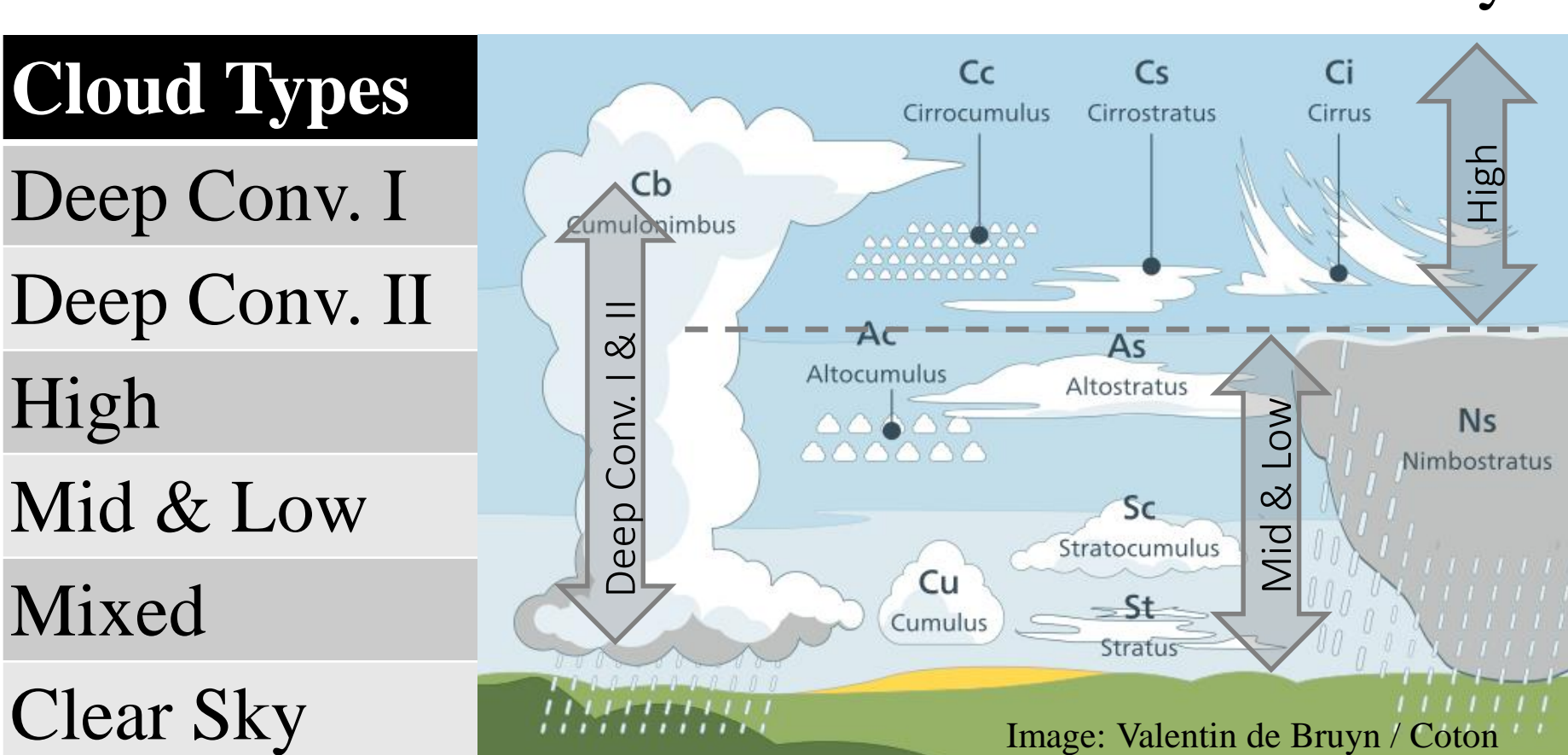
Precipitation Products

Product	Reference data in this study
DPR-Ku L2 (ver5) (radar)	GPM Core-observatory http://www.eorc.jaxa
GMI L2 (ver5) (PMW)	
IMERG (ver.5) (IR+PMW)	GSMaP_MWR V4.7.2] Rain_rate(0.25x0.25deg):01JUL200. Ushio et al. (2009)
“ (IR)	
“ (PMW)	
GSMaP MVK (ver.7) (IR+PMW)	
“ (IR)	
“ (PMW)	

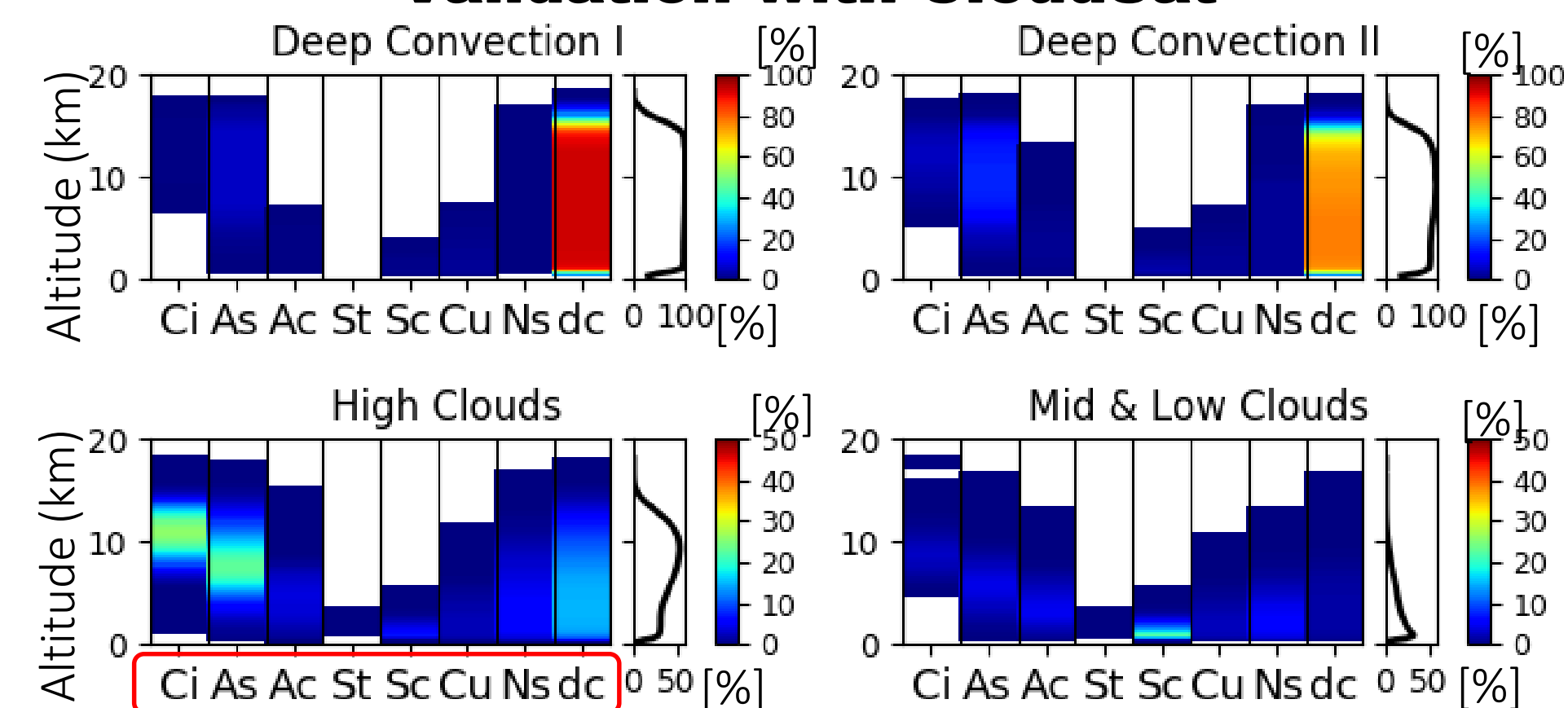
* PMW: Passive Microwave, IR: Infrared

Cloud Type Information

Source Data: Satellite Cloud Grid Information by JMA (Vis. and IR of Himarwari-6) @ 0.2° x 0.25° of WN Pacific / hourly



Validation with CloudSat



Cloud type by CloudSat (2B-CLDCLASS)

Our cloud type clarification works well !!

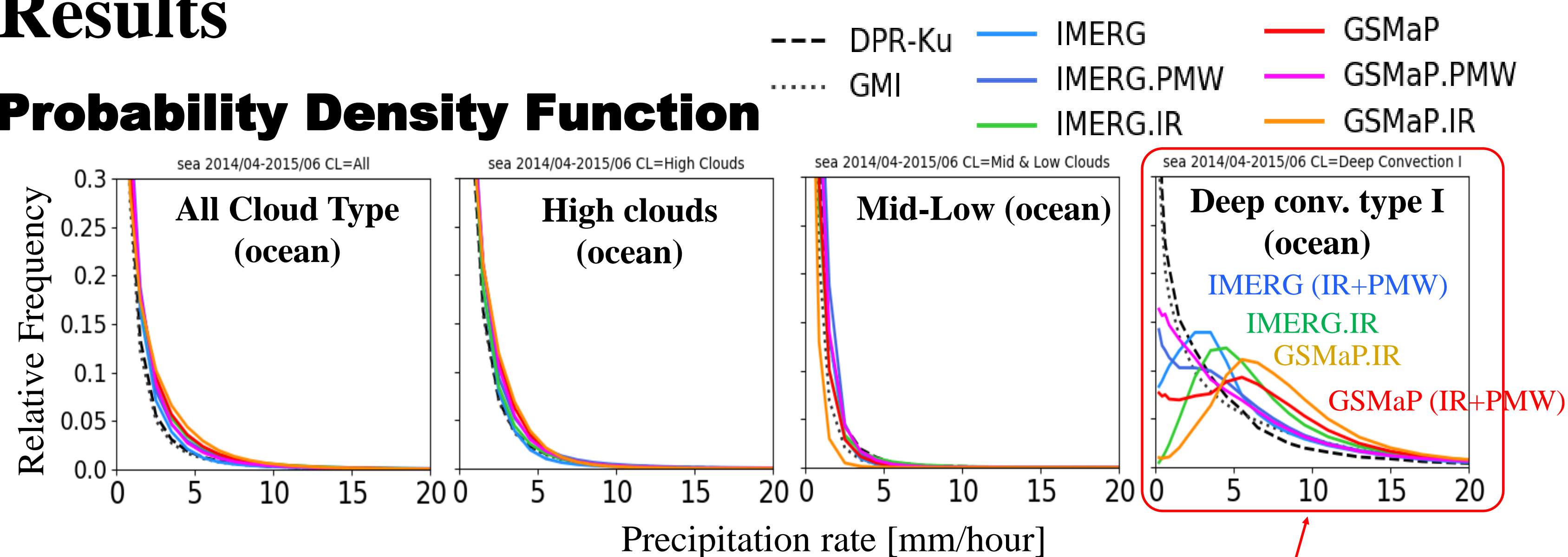
Method

Precipitation × Cloud type = Precipitation by each cloud type

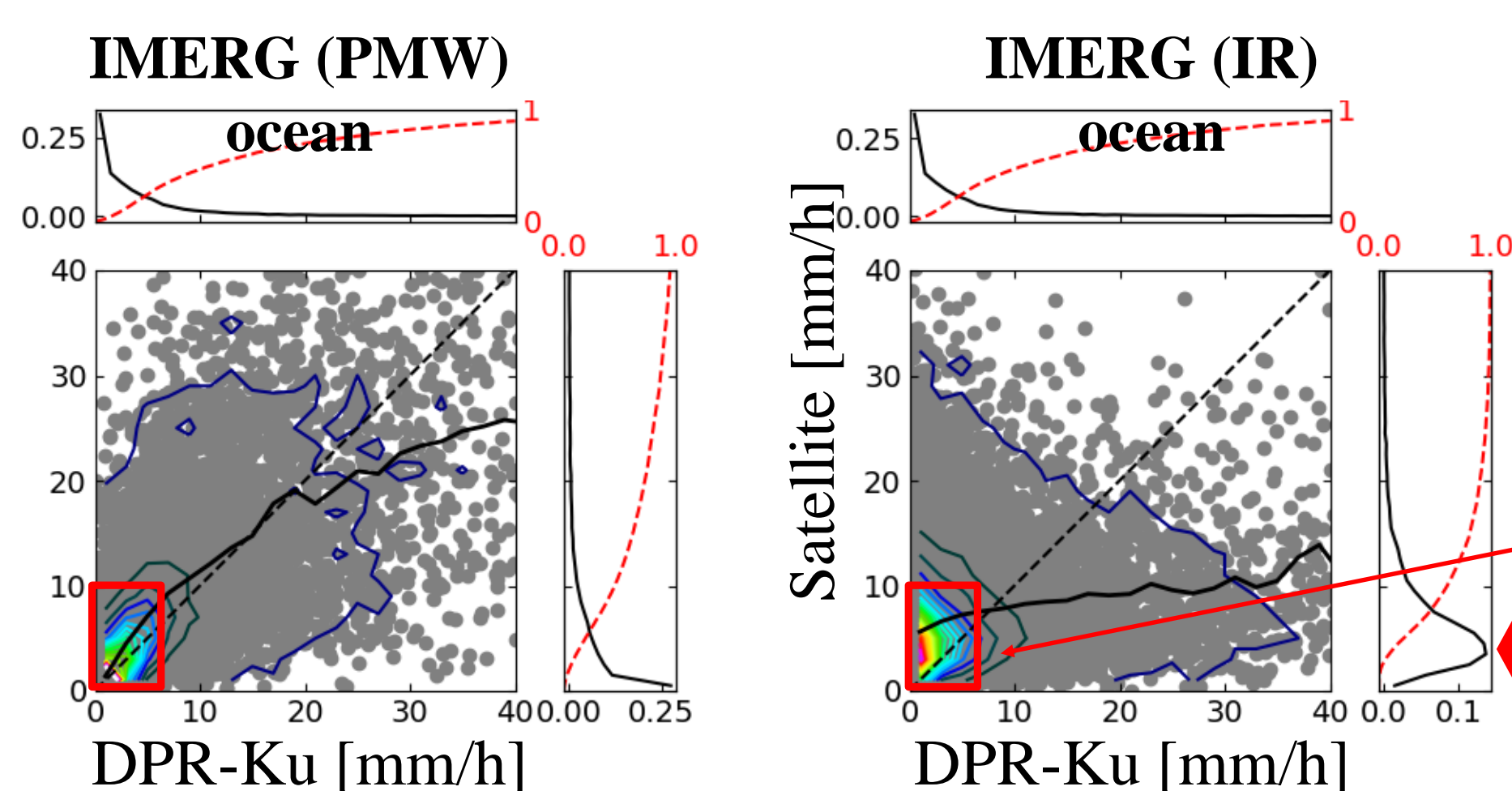
every 1-hour @0.20° x 0.25° pixel (Apr. 2014 – June 2015 (w/o Nov.-Mar.))

Results

Probability Density Function



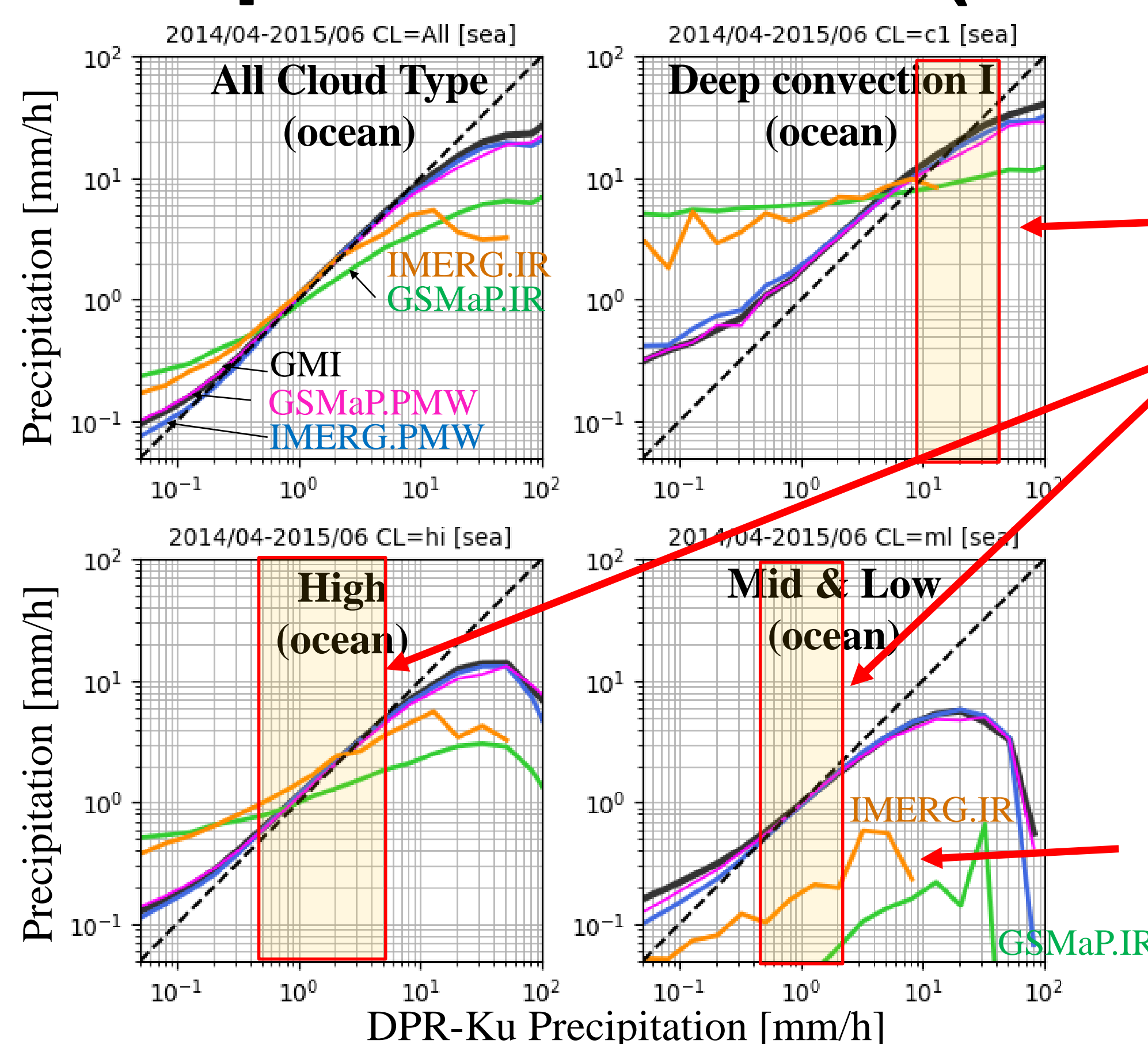
Comparison with DPR-Ku



IR-based (&IR+PMW) products have very different characteristics for Deep convection.

IR-based product significantly overestimate weak precipitation of Deep convection.

Comparison with DPR-Ku (multi products)



Good performance range differs by cloud type.

- Deep conv.: Heavier intensity (10 – 30 mm h⁻¹)
- High & Mid-Low : Weak intensity (0.5 – 6 mm h⁻¹)

Typical states of cloud types are captured, but the variability outside it is not captured well.

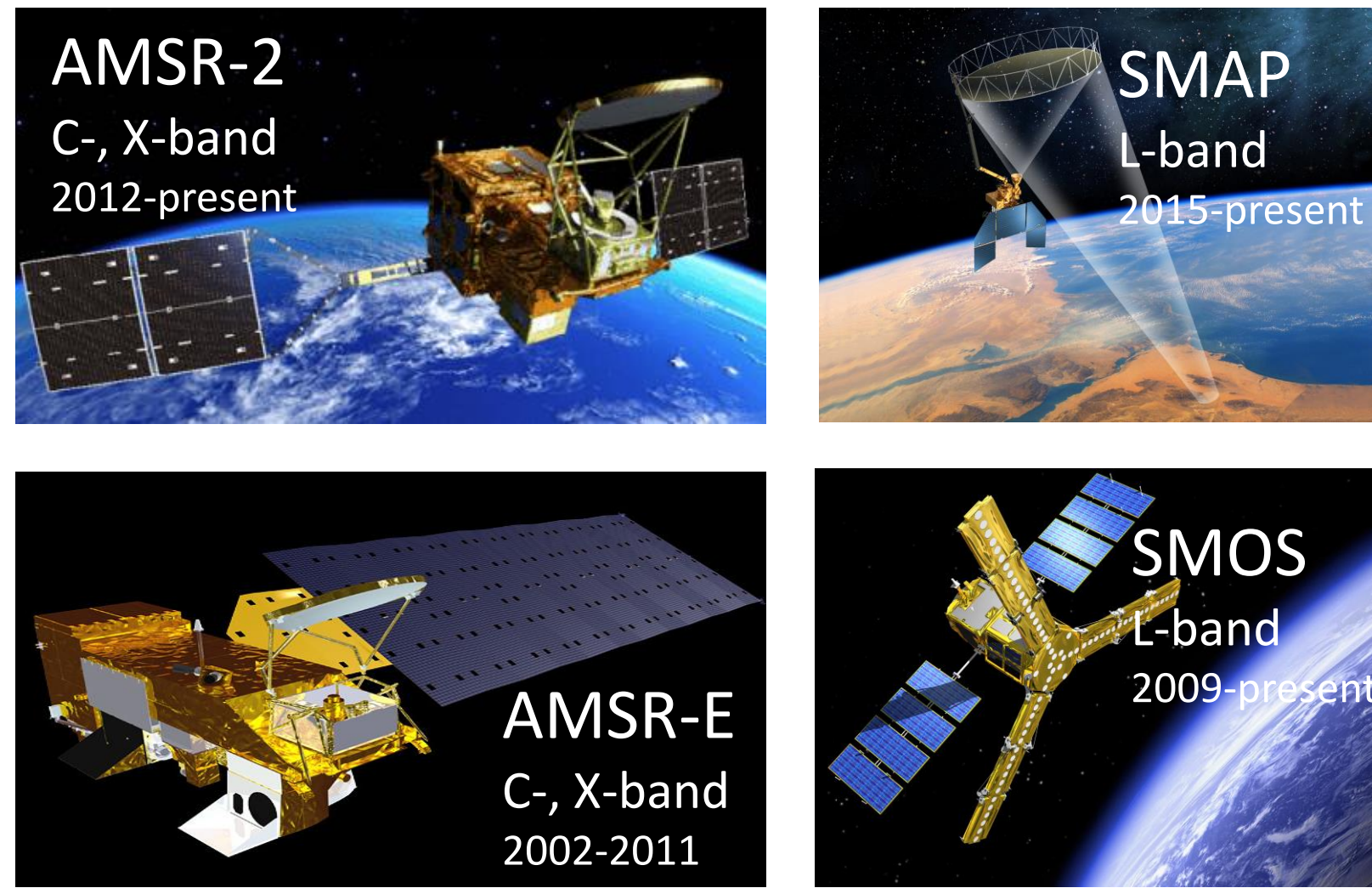
IRs underestimate entire range @ Mid & Low cloud (ocean)

Conclusions

- Systematic biases of precipitation products associated with cloud type are found.
- IR-based precipitation estimates for deep convection has large bias for deep convection (@weak precipitation)
- Typical states of precipitation by each cloud type are captured by products.
- However, variability outside of typical range is not captured well.
- Considering cloud type will help identifying causes of errors and also development of retrieval algorithm.

Reference: Utsumi, N. and Kim, H. (2018), Warm Season Satellite Precipitation Biases for Different Cloud Types Over Western North Pacific, IEEE Geosci. Remote Sens. Lett. (Acceted)

We have many satellites capable of mapping global soil moisture



BUT...

- The L-, C- and X-band brightness temperature observations are not consistent;
- The soil moisture retrieval algorithm and parameters are not consistent;
- Different frequencies have different sensing depths.

WE PROPOSE:

15+ years of consistent long-term uniform soil moisture data record

Inter-calibrate the L-, C- and X-band brightness temperatures

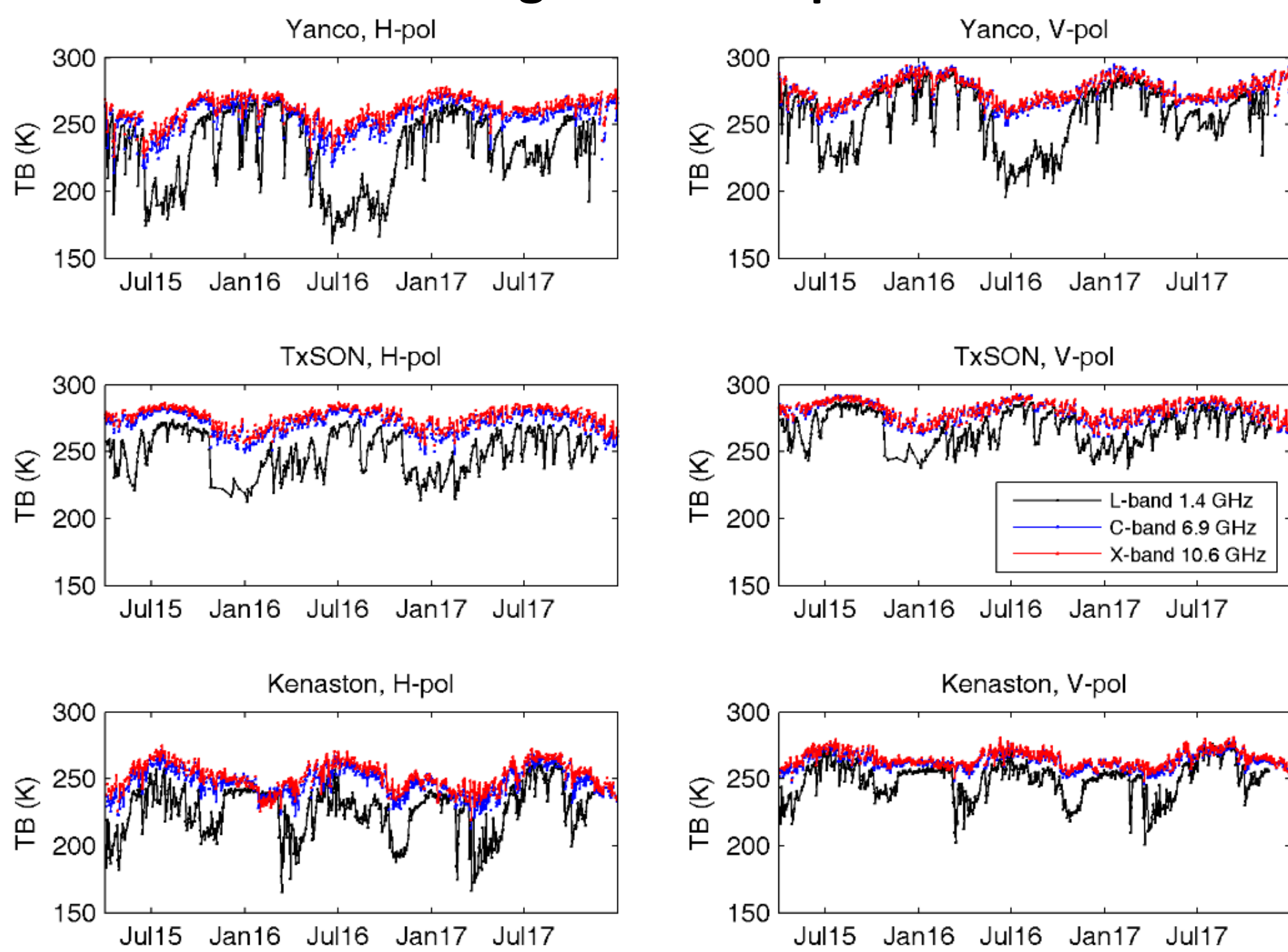
Retrieve consistent SM using the brightness temperature at different frequencies

Compensate for different sensing depths of L-, C- and X-band, present the SM at a uniform depth

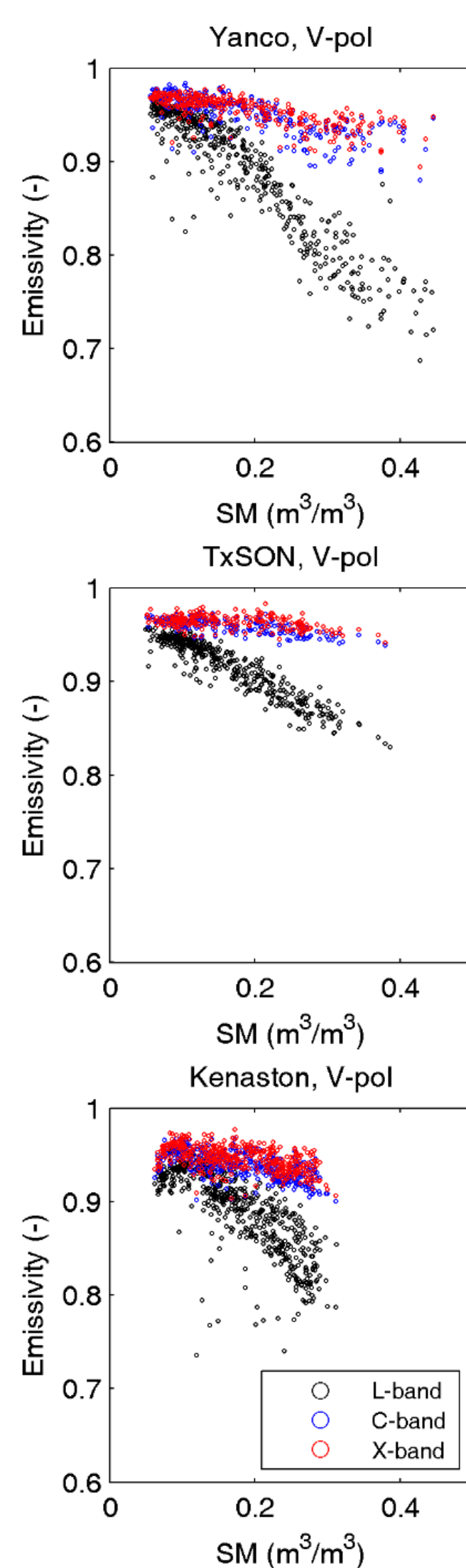
Analysis started from 2 satellites and 3 in-situ data sets

- Satellites: **SMAP** (L-band) and **AMSR2** (C-, X-band) to cover different frequencies
- In-situ Sites: 1) **Yanco**, NSW, Australia (mixed crop-grassland); 2) **TxSON**, TX, USA (grassland); 3) **Kenaston**, Sask. Canada (Cropland).

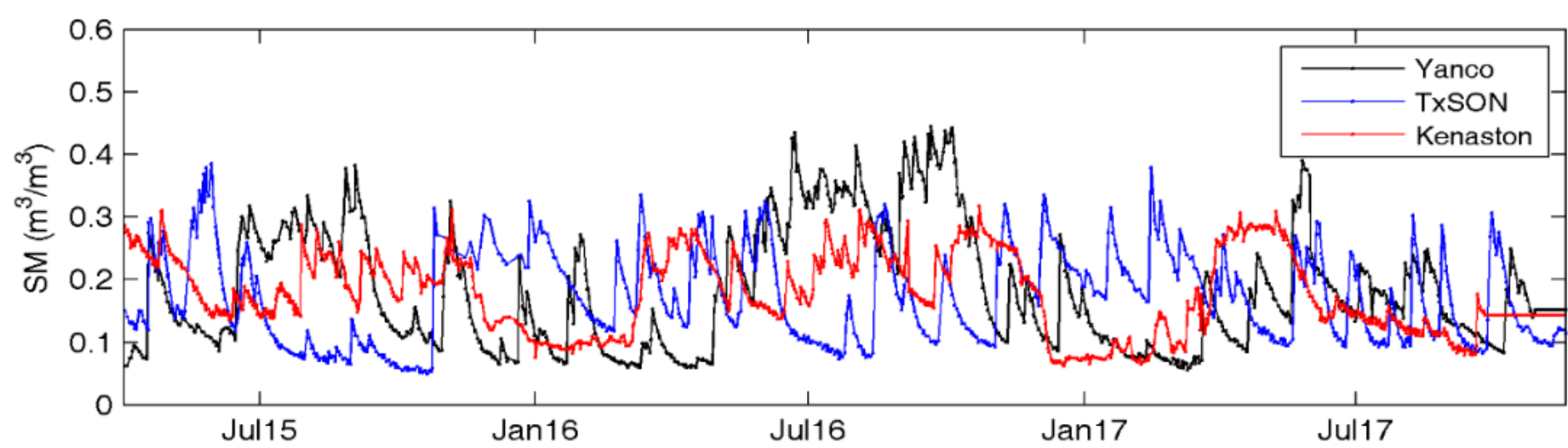
Brightness Temperature



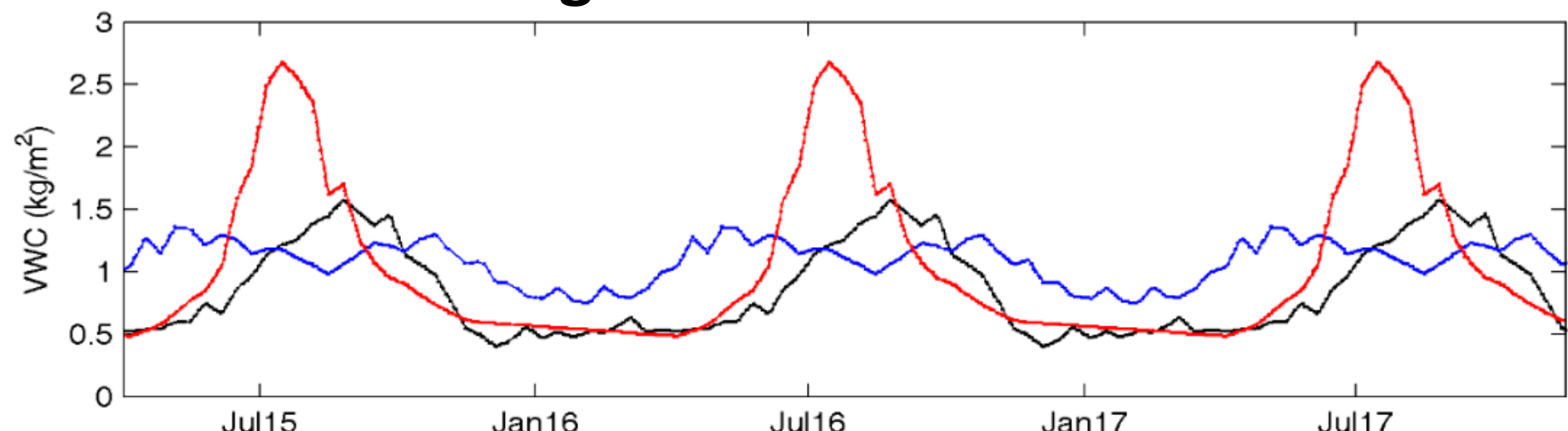
Emissivity VS Soil Moisture



In-Situ Soil Moisture

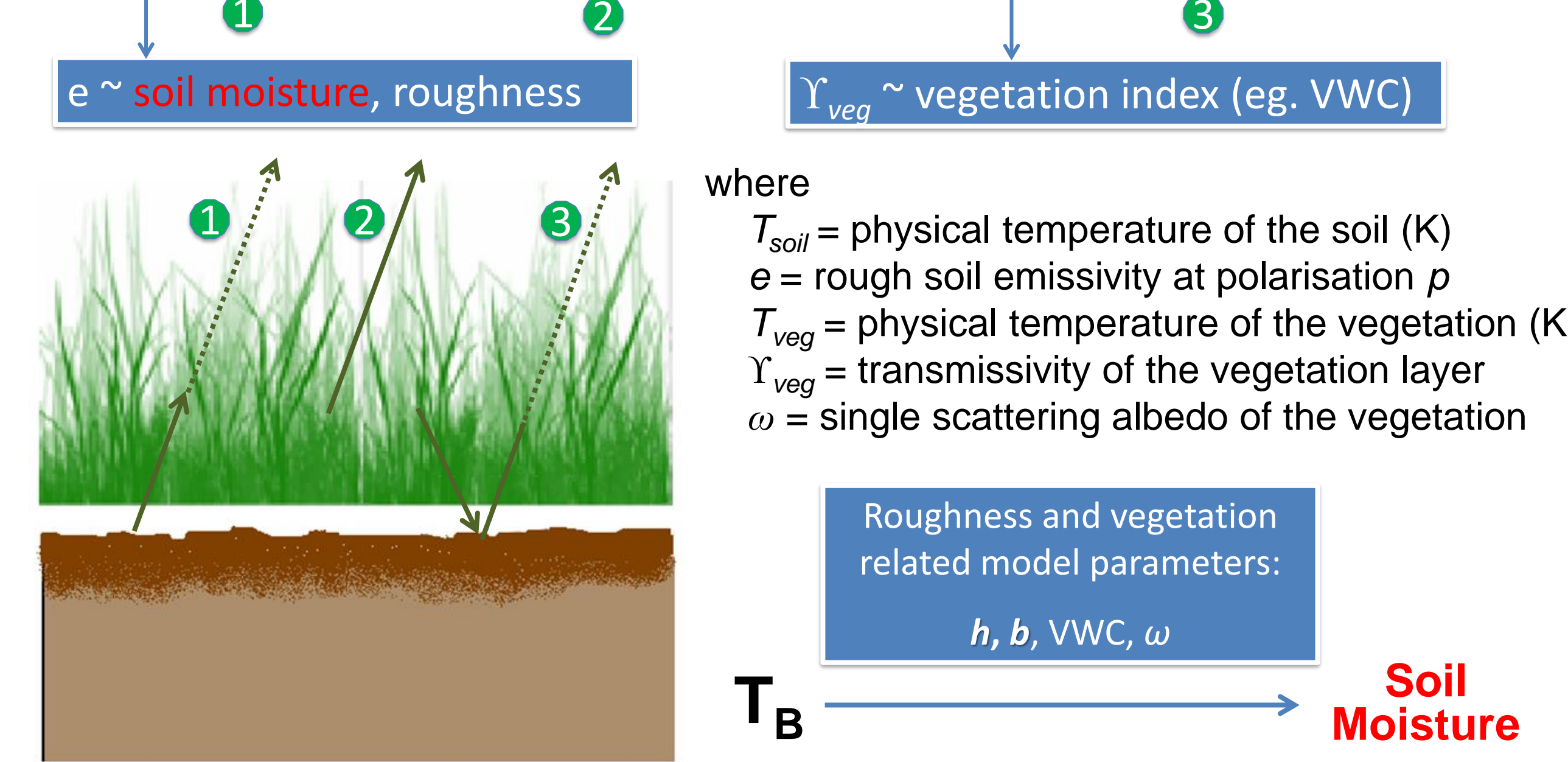


Vegetation Water Content



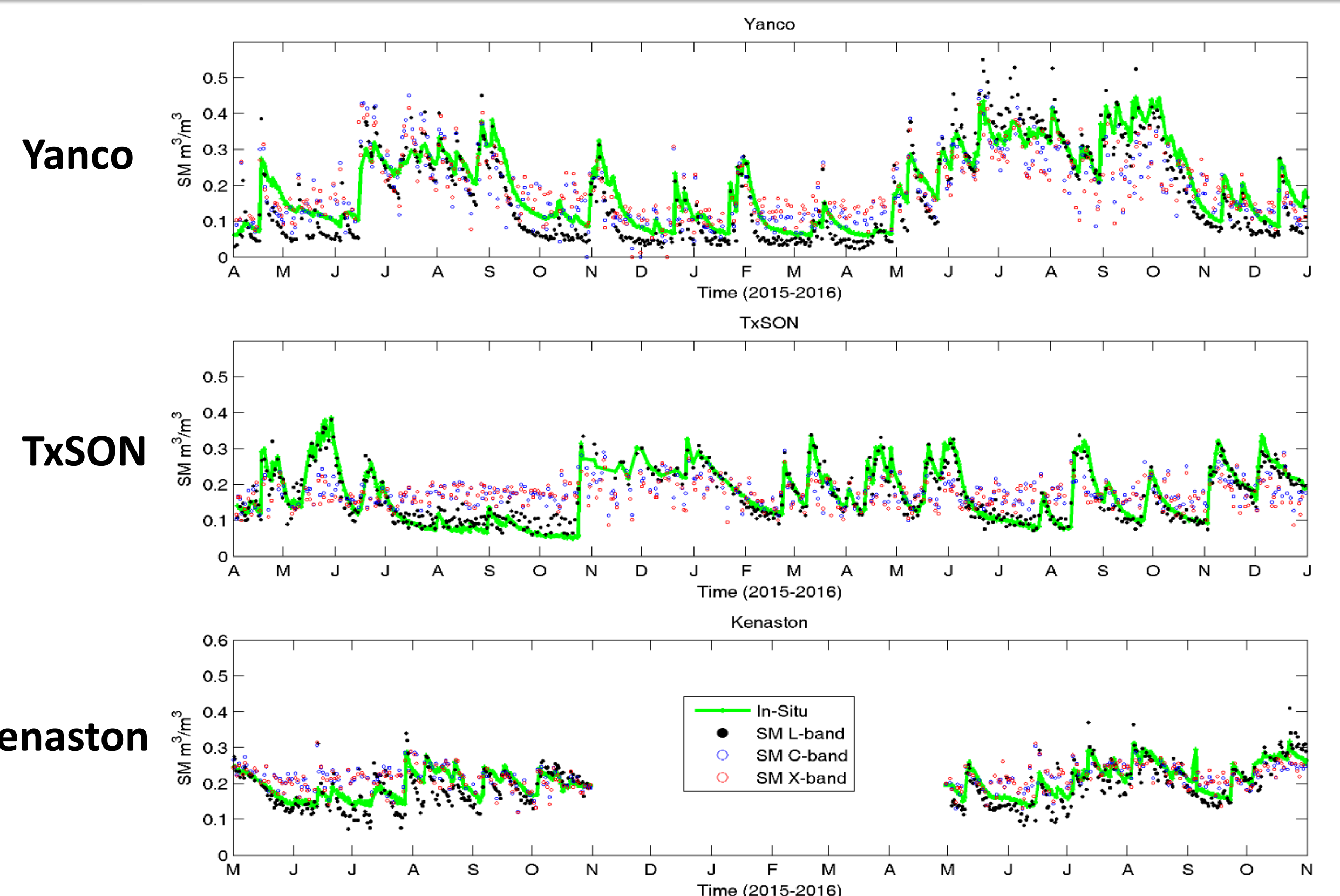
The tau-omega model & model calibration

$$T_B = e T_{soil} \gamma_{veg} + (1 - \gamma_{veg})(1 - \omega) T_{veg} + (1 - \gamma_{veg})(1 - \omega)(1 - e) \gamma_{veg} T_{veg}$$



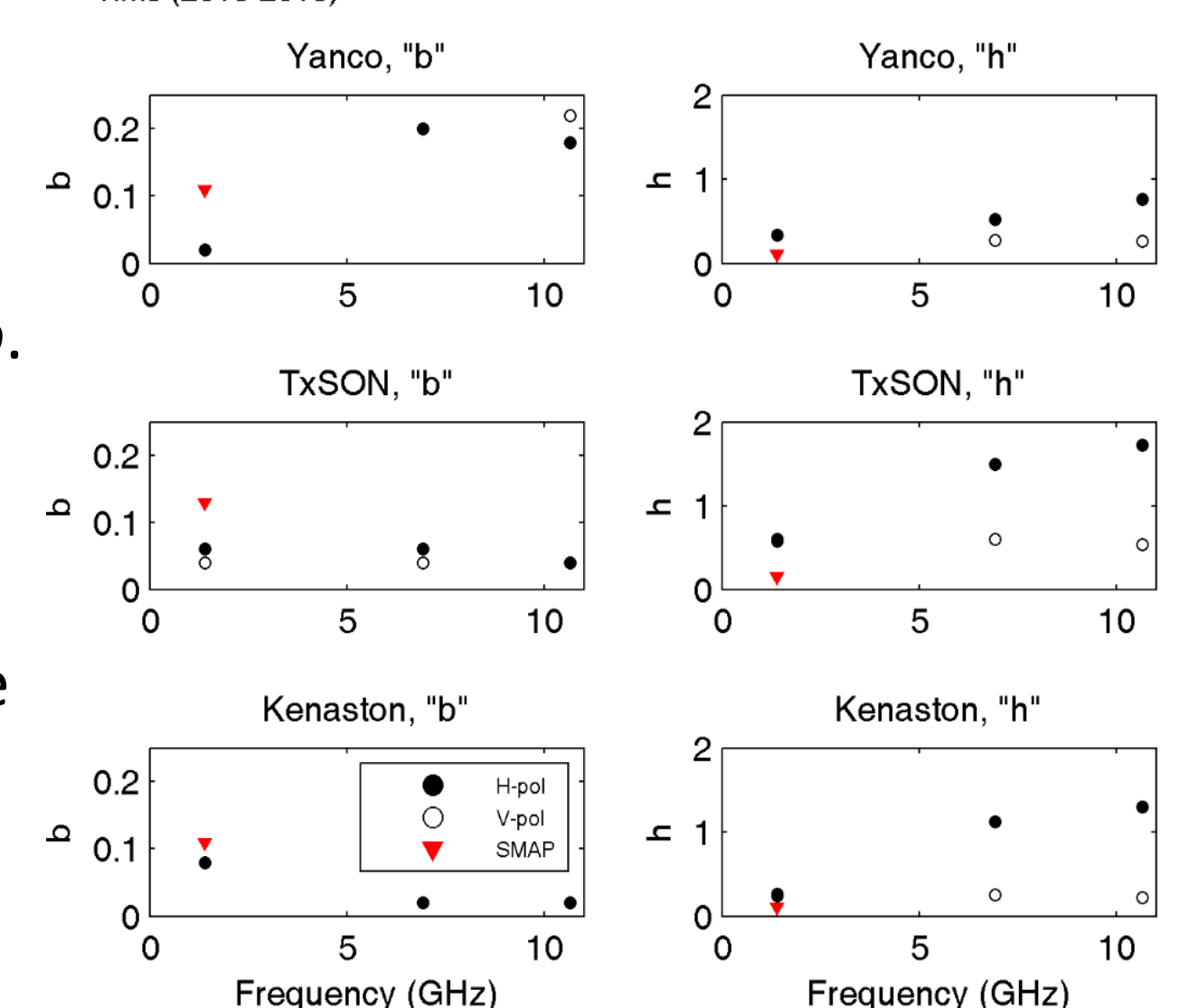
- Calibration focuses on: roughness parameter h & vegetation parameter b
- Pre-set ranges of 0-1.5 for b and 0-2 for h with 0.01 interval, retrieve SM using all combinations of b and h by minimizing SSE of observed and simulated TB
- Determine the optimum combination of b and h with the smallest RMSD between retrieved and in-situ soil moisture.

Soil Moisture Retrieval from different frequencies



Parameters VS Frequency

- At H-pol, h is more sensitive to frequency change compared with b . At V-pol, however, h is not very responsive to frequency change.
- Currently, AMSR2 does not have parameters readily available for the SCA algorithm. The result provide such parameters for crop and grassland.



Conclusions and future work

- L-band, V-pol** has the best accuracy: ub.RMSD = 0.025 ~ 0.047 m³/m³.
- C-, X-band, V-pol is satisfactory: ub.RMSD = 0.039 ~ 0.076 m³/m³.
- Calibrated parameters improve the L-band accuracy by 0.01-0.05 m³/m³.
- Include SMOS and AMSR-E radiometers to expand data set back to 2002.
- Include more sites across the world; calibrate landcover-dependent parameters.